THE RELATIONSHIP BETWEEN OCEANIC TRANSFORM FAULT SEGMENTATION, SEISMICITY, AND THERMAL STRUCTURE

BY

Monica Wolfson-Schwehr

B.S., Eckerd College, 2001

M.S., University of South Florida, 2005

DISSERTATION

Submitted to the University of New Hampshire
in Partial Fulfillment of
the Requirements for the degree of

Doctor of Philosophy

in

Oceanography

December 2015

ProQuest Number: 10000389

ProQuest 10000389

ProQuest LLC.
789 East Eisenhower Parkway
P.O. Box 1346
Ann Arbor, MI 48106 - 1346

This thesis/dissertation has been examined and approved in partial fulfillment of the requirements for the degree of Doctor of Philosophy in Oceanography by:

Dissertation Director, Margaret S. Boettcher, Associate Professor of Geophysics

Larry A. Mayer, Professor of Earth Sciences and Ocean Engineering

James V. Gardner, Affiliate Professor of Earth Sciences

Joel E. Johnson, Associate Professor of Geology

Brian R. Calder, Research Associate Professor in Ocean Engineering

Jeffrey J. McGuire, Associate Scientist, Geology and Geophysics,
Woods Hole Oceanographic Institute, Woods Hole, MA 02543

On October 15, 2015

Original approval signatures are on file with the University of New Hampshire Graduate School.

Acknowledgments

I am truly thankful to have been part of the Center for Coastal and Ocean Mapping/Joint Hydrographic Center family. Their support and encouragement kept me going over the years, and I have learned so much from my time there. I cannot imagine a better committee than Margaret Boettcher, Larry Mayer, Jim Gardner, Joel Johnson, Brian Calder, and Jeff McGuire. Their support has been unwavering over the course of my PhD, even when the road got a bit winding. I want to thank Margaret for her kindness and patience over the years, and for her steadfast smile that greeted me every time we had a meeting. While she has been an exceptional advisor and will be a great colleague, she has also become a good friend. I look forward to working with her in the future and continuing to learn from her. Jim was always there with a kind, encouraging word, just when I needed it the most. Jim and Joel would get visibly excited when we discussed my research during committee meetings, and their enthusiasm was always contagious. Larry was a huge support from the beginning, not just in providing funding for my research but in helping me develop my voice as a scientist. Brian not only helped redirect me when I would lose my way in some piece of code, or get confused on the best way to compute an uncertainty, but he is the absolute best New York Times Crossword buddy when standing watch at sea. Jeff provided an excellent excuse to travel down to the breathtaking Woods Hole Oceanographic Institute campus, and was always willing to take time out of his schedule to meet with me when he was in NH, when I was down in MA, or when we both happened to be in CA.

My family has been amazingly supportive over the course of my graduate career. I want to

thank my parents, Stewart and Leona Wolfson, who tirelessly listened to me babble on excitedly about my research even when they had no clue what I was talking about; my brother, Sean Wolfson, who challenged and encouraged me; my husband Kurt Schwehr, who has provided me with so much strength and love; and lastly but certainly not least, my son Lincoln, who continues to be the best stress reliever ever.

Table of Contents

List of Tables

ABSTRACT

THE RELATIONSHIP BETWEEN OCEANIC TRANSFORM FAULT SEGMENTATION, SEISMICITY, AND THERMAL STRUCTURE

by

Monica Wolfson-Schwehr
University of New Hampshire, December, 2015

Mid-ocean ridge transform faults (RTFs) are typically viewed as geometrically simple, with fault lengths readily constrained by the ridge-transform intersections. This relative simplicity, combined with well-constrained slip rates, make them an ideal environment for studying strike-slip earthquake behavior. As the resolution of available bathymetric data over oceanic transform faults continues to improve, however, it is being revealed that the geometry and structure of these faults can be complex, including such features as intra-transform pull-apart basins, intra-transform spreading centers, and cross-transform ridges. To better determine the resolution of structural complexity on RTFs, as well as the prevalence of RTF segmentation, fault structure is delineated on a global scale. Segmentation breaks the fault system up into a series of subparallel fault strands separated by an extensional basin, intra-transform spreading center, or fault step. RTF segmentation occurs across the full range of spreading rates, from faults on the ultraslow portion of the Southwest Indian Ridge to faults on the ultrafast portion of the East Pacific Rise (EPR). It is most prevalent along the EPR, which hosts the fastest spreading rates in the world and has undergone multiple changes in relative plate motion over the last couple of million years. Earthquakes on RTFs are known to be small, to scale with the area above the $600°C$ isotherm, and to exhibit some of the most predictable behaviors in seismology. In order to determine whether segmentation affects the global RTF scaling relations, the scalings are recomputed using an updated seismic catalog and fault database in which RTF systems are broken

up according to their degree of segmentation (as delineated from available bathymetric datasets). No statistically significant differences between the new computed scaling relations and the current scaling relations were found, though a few faults were identified as outliers. Finite element analysis is used to model 3-D RTF fault geometry assuming a viscoplastic rheology in order to determine how segmentation affects the underlying thermal structure of the fault. In the models, fault segment length, length and location along fault of the intra-transform spreading center, and slip rate are varied. A new scaling relation is developed for the critical fault offset length (O_C) that significantly reduces the thermal area of adjacent fault segments, such that adjacent segments are fully decoupled at $\sim 4O_C$. On moderate to fast slipping RTFs, offsets ≥ 5 km are sufficient to significantly reduce the thermal influence between two adjacent transform fault segments. The relationship between fault structure and seismic behavior was directly addressed on the Discovery transform fault, located at 4°S on the East Pacific Rise. One year of microseismicity recorded on an OBS array, and 24 years of Mw ≥ 5.4 earthquakes obtained from the Global Centroid Moment Tensor catalog, were correlated with surface fault structure delineated from high-resolution multibeam bathymetry. Each of the 15 Mw ≥ 5.4 earthquakes was relocated into one of five distinct repeating rupture patches, while microseismicity was found to be reduced within these patches. While the endpoints of these patches appeared to correlate with structural features on the western segment of Discovery, small step-overs in the primary fault trace were not observed at patch boundaries. This indicates that physical segmentation of the fault is not the primary control on the size and location of large earthquakes on Discovery, and that along-strike heterogeneity in fault zone properties must play an important role.

1 | INTRODUCTION

1.1 Introduction

Mid-ocean ridge transform faults (RTFs) are strike-slip faults that offset the mid-ocean ridge system and accommodate motion from seafloor spreading. Oceanic transform faults are typically viewed as geometrically simple, with fault lengths readily constrained by their ridge-transform intersections (Wilson, 1965a; Menard & Atwater, 1968; Searle, 1983; Fox & Gallo, 1989). Numerous studies of strike-slip fault earthquake behavior have focused on RTFs, due to their relative simplicity compared to their continental counterparts (Boettcher & Jordan, 2004; McGuire *et al.*, 2005; Willoughby & Hyndman, 2005; Boettcher & McGuire, 2009; Sykes & Ekström, 2012). Whereas continental strike-slip faults often have a complex crustal makeup that may include metamorphic, igneous, and sedimentary rock, oceanic lithosphere is more homogenous, composed predominantly of a mafic basalt-dominated crust that overlies an ultramafic upper mantle primarily composed peridotite (Jordan & Grotzinger, 2008). Tectonic parameters, such as fault length and slip rate, are often better constrained for oceanic faults, even though source and location parameters of the seismicity are not. Furthermore, the relatively fast slip rates of some mid-ocean ridge transform faults, combined with small to moderate maximum earthquake magnitudes result in seismic cycles that are often less than 10 years, making it feasible to observe an entire cycle within a relatively short seismic catalog (Boettcher & Jordan, 2004; McGuire, 2008; Boettcher & McGuire, 2009). Earthquakes on RTFs are known to be small, to scale with the area above the 600°C isotherm, and to exhibit some of the

1

most predictable behaviors in seismology. There is an apparent seismic deficit on RTFs and it is not understood why the largest events do not rupture the full fault area (Boettcher & Jordan, 2004).

Recent global bathymetric data compilations, along with several high-resolution multibeam and sidescan sonar surveys over oceanic transform faults, show that the geometry and structure of RTFs can be complex. The majority of RTFs are defined by their median valleys, however, some faults are expressed as median ridges. The traditional view of RTFs is that they offset the mid-ocean ridge system at right angles, yet many faults are oriented obliquely to the ridge. The presence of transverse ridges and troughs, anonymously rotated abyssal hill fabric, and the presence or lack of fracture zone traces also add to the complexity of the RTF system. Additionally, many RTFs are physically segmented, in which the fault system is broken up into a series of parallel to subparallel fault strands separated by extensional basins or intra-transform spreading centers (Fig. 1.2). Morphologic studies on RTFs with an emphasis on segmentation are limited in number and tend to focus on individual fault locations (Fornari *et al.*, 1989; Embley & Wilson, 1992; Pockalny *et al.*, 1997; Hékinian *et al.*, 2000; Sclater *et al.*, 2005). One of the primary goals of this study, therefore, is to quantify RTF segmentation on a global scale using existing high-resolution multibeam sonar bathymetry, in conjunction with global bathymetric compilations.

This dissertation investigates the relationship between fault structure and seismicity on RTFs, and seeks to determine whether fault segmentation can help explain the low seismic coupling and small earthquake size observed on oceanic transform faults. To this end, three primary questions are addressed:

1. How is segmentation related to the underlying thermal structure of the fault?

2. How prevalent is RTF segmentation and how does it affect global scaling relations?

3. What is the relationship between fault structure and seismicity on the Discovery Transform Fault?
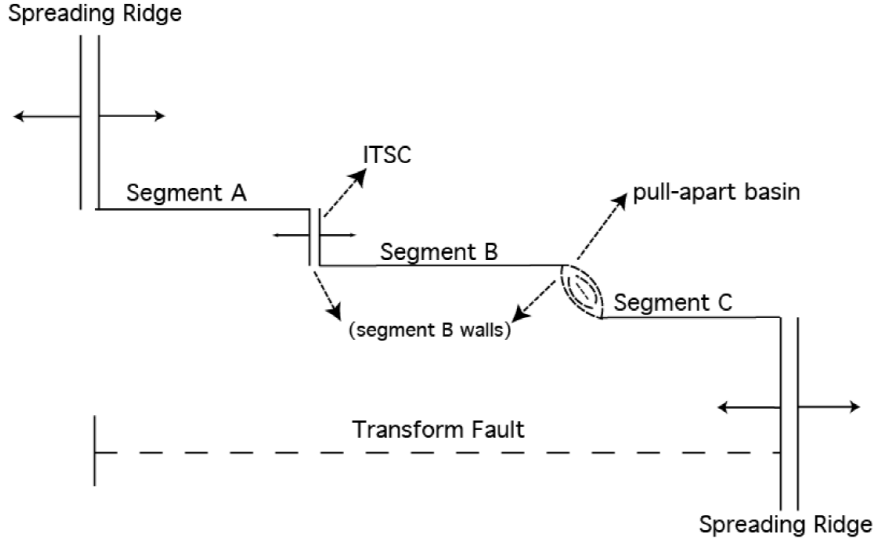
Figure 1.2: A schematic representation of physical segmentation along an oceanic transform fault and the possible types of offsets: ITSC or a pull-apart basin.

The question of how RTF segmentation reflects the underlying thermal structure of RTFs is addressed in chapter 2. Three-dimensional finite element modeling is used to explore the effect of intra-transform spreading centers (ITSCs) above 600°C. A simplified RTF geometry, in which the transform domain is always perpendicular to the ridge, is modeled using a viscoplastic rheology that accounts for brittle failure mechanisms in the upper lithosphere and nonlinear ductile flow in the lower lithosphere. The spreading rate, length of fault segments, and the location and length of the ITSC are varied between model runs. Using fault segment lengths, the length of the ITSC, and the spreading rate, a scaling relation is developed for a critical fault offset length (O_C) that significantly reduces ($\sim$63%) the combined thermal area of the two fault segments. O_C then represents the length of offset at which two adjacent fault segments begin to decouple from one another, with full decoupling at $\sim$4O_C. Offsets both larger and smaller than O_C correspond with the endpoint of repeating rupture patches, however, indicating that the secondary effects of these offsets, such as enhanced hydrothermal circulation, increased porosity, and alteration of the host rock into weaker materials may also affect the seismogenic properties of RTFs.

3

Chapter 3 addresses the question of how prevalent RTF segmentation is, and whether or not this segmentation affects global scaling relations. A global characterization of oceanic transform fault structure, involving the delineation of 202 individual fault segments, is presented. These segments are classified into 95 single segment faults, and 37 segmented RTF systems. Segmentation was found to occur on RTFs representing the full range of slip rates, from faults on the ultraslow portion of the Southwest Indian Ridge, to faults on the ultrafast portion of the East Pacific Rise. Segmentation was most prevalent on the East Pacific Rise, which boasts the fastest slip rates in the world and bounds the southeastern portion of the Pacific Plate. The Pacific Plate has undergone multiple, small counterclockwise changes in relative plate motion over the last couple of million years, putting all the faults along the EPR, with the exception of Clipperton Transform Fault, under extension. This extension, combined with the high slip rates, results in lithospheric thinning and tearing within the transform fault domain, which may eventually lead to the formation of intra-transform spreading centers. (Menard & Atwater, 1968; Fox & Gallo, 1989; Lonsdale, 1994; Pockalny *et al.*, 1997; Gregg *et al.*, 2006; Behn *et al.*, 2007). While both a sufficiently high slip rate and a recent change in plate motion direction are required to form a segmented transform fault, whether or not one process dominates over the other is not known. Global scaling relations on RTFs relate the fault tectonic parameters of length and slip rate to seismic parameters such as the size of the maximum expected earthquake and seismic coupling. Segmentation on RTFs was not accounted for when these relations were developed, and adjacent fault segments closer together than 35 km were combined in the database (Boettcher & Jordan, 2004; Boettcher & McGuire, 2009). To determine whether segmentation has a significant affect on the scaling relations, and in particular, if it can explain the low seismic coupling and small earthquakes, the relations are recomputed using an updated seismic catalog obtained from the Global Centroid Moment Tensor Project (CMT) and a new segmented fault database. For this new analysis, two adjacent fault segments are only combined if the adjacent offset is less than 5 km long, the length of offset found to decouple fault segments on moderate- to

4

fast-slipping faults. With the exception of a few outlier faults, the results of this analysis were not significantly different from the current set of global scaling relations, indicating that segmentation alone cannot account for the low seismic coupling and small maximum earthquake size observed on RTFs. Finally, the few outlier faults, faults that behave as exceptions to the rules set forth by the scaling relations, are examined in detail and the observed structure on the fault is used to explain their anomalous behavior.

Question 3 is addressed in chapter 4, exploring the influence of physical fault structure on the seismic behavior of the Discovery Transform Fault, located at $\sim 4°$S on the East Pacific Rise. Surface fault structure delineated from high-resolution multibeam bathymetry is correlated with one year of microseismicity recorded during a 2008 ocean bottom seismograph deployment and 24 years of $5.4 \leq$ Mw ≤ 6.0 earthquakes obtained from the Global Centroid Moment Tensor (CMT) catalog. The large earthquakes obtained from the CMT catalog were relocated using a teleseismic surface wave cross-correlation technique into one of five distinct rupture patches on the fault. Microseismicity was relocated using the HypoDD relocation algorithm, and was found, in general, to cluster between these large rupture patches. The western fault segment of the Discovery Transform Fault is composed of three zones of varying structural and seismic behavior: a zone with no large events and abundant microseismicity, a fully coupled zone with large earthquakes, and a complex zone with multiple fault strands and abundant seismicity. The three rupture patches on the western fault segment correlate with small structural features in the bathymetry, though none of these features appear to be actual offsets, or step-overs, in the active fault trace. This indicates that physical structure alone is not responsible for controlling the size and location of these repeating rupture patches, and that along-strike heterogeneity in fault zone processes must play an important role.

The final chapter of this dissertation brings everything together and addresses the overarching question of this research: Can fault segmentation can help explain the low seismic coupling and small earthquake size observed on oceanic transform faults? While the thermal modeling showed

that offsets greater than or equal to a critical offset length can decouple adjacent fault segments, the scaling relation analysis indicated that segmentation alone cannot account for the low seismic coupling and small maximum earthquake size observed on RTFs. It is likely an interplay between the structure of the fault and along-strike heterogeneity in fault zone processes that control the size of the largest earthquakes.

2 | THE RELATIONSHIP BETWEEN FAULT SEGMENTATION AND UNDERLYING THERMAL STRUCTURE ON OCEANIC TRANSFORM FAULTS

2.1 Introduction

The largest earthquakes on mid-ocean ridge transform faults rupture a small portion of the available fault area (e.g., Bird *et al.*, 2002), which is proportional to the total fault area to the one-half power (Boettcher & Jordan, 2004). A remarkable observation from a number of RTFs is that the largest earthquakes appear to repeatedly rupture the same patch of the fault and do not propagate through short (∼10 km long) rupture barriers that separate the rupture zones (McGuire, 2008; Boettcher & McGuire, 2009; McGuire *et al.*, 2012; Wolfson-Schwehr *et al.*, 2014). Large and small scale offsets in the fault trace, associated with intra-transform spreading centers (ITSCs), extensional basins, and/or jogs in the fault trace, have been identified on many RTFs, including Blanco (Embley & Wilson, 1992), Siqueiros (Fornari *et al.*, 1989), Gofar (McGuire *et al.*, 2012), Discovery (Wolfson-Schwehr *et al.*, 2014), and Eltanin (Sykes & Ekström, 2012) RTFs. These offsets break the fault up into a series of two-or-more parallel to subparallel faults strands. It has been suggested that the low maximum magnitudes observed on RTFs may be due, in part, to not considering segmentation of the active fault trace. Transform offsets along the fault trace may also explain the occurrence of rupture patches versus rupture barriers if they occur at the boundary between these zones.

In this study, I investigated the effect of fault segmentation using three-dimensional models of

RTF thermal structure. Specifically, I used COMSOL Multiphysics (v. 4.2a) to run a series of simulations of segmented RTFs that tested a range of fault segment lengths, orthogonal offset lengths, and full spreading rates and modeled the lithosphere and asthenosphere as a steady-state, incompressible flow. Coulomb failure incorporates brittle processes in the lithosphere and upper mantle, and a temperature-dependent olivine flow law activates ductile deformation in the asthenosphere (e.g., Hirth & Kohlstedt, 2003). The results from the modeling work led to the development of a scaling relation for the critical offset length, the length of offset necessary to significantly reduce the thermal area underlying a segmented transform fault system, such that the two adjacent fault segments begin to behave independently (i.e., their thermal structures begin to decouple from one another). Predictions of the critical offset length are then used to determine whether offsets observed along three well-studied faults on the East Pacific Rise and the Gorda Ridge may be controlling the location of rupture patches versus rupture barriers on these faults.

2.2 Model Setup

To explore the interplay between fault segmentation and the underlying thermal structure on RTFs, I modeled various RTF geometries composed of two fault segments separated by an lateral offset. Seven pairs of fault segment lengths were modeled ranging in length from 10 to 150 km. The length of the offset was varied from 0 km, where the transform fault system is simply composed of a single, unbroken fault segment, to 30 km (Table 2-1, Fig. 2.1). The lateral extent of the model domain was determined in the across-fault direction by the length of the ridge segments (50 km each) plus the length of the orthogonal offset, and in the along-fault direction by the length of the fault segment plus an additional 50 km on either side of the fault. All models were 100 km deep (Fig. 2.1).

The model set up following the methodology laid out in Roland *et al.* (2010). Mantle flow in the model was driven by imposing a horizontal surface velocity of $V/2$ on either side of the fault for $V = 2$ - 14 cm/yr, representing slow to fast spreading mid-ocean ridges. Boundary conditions

Table 2-1: Geometries of the modeled faults

Geometry	L_1 (km)	L_2 (km)	$L_T (km)$
1	50	50	100
2	10	90	100
3	25	75	100
4	40	60	100
5	100	100	200
6	80	120	200
7	50	100	150
Length of Offsets	0, 1, 2, 5, 10, 15, 20, 25, 30 km		
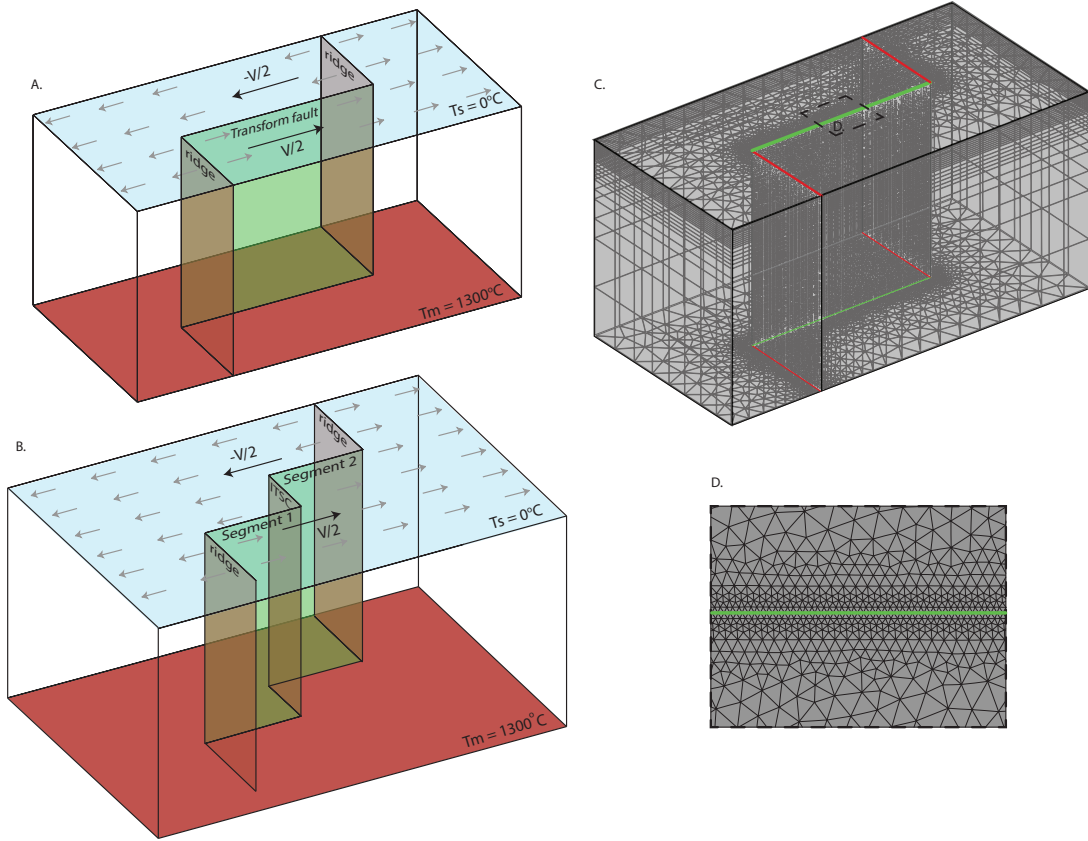
Figure 2.1: A) Schematic of the model setup showing a single, unbroken transform fault segment. B) Schematic of the model setup for a segmented RTF with two fault segments separated by an ITSC. In both A and B, V is the spreading rate of the ridge, T_s is the surface temperature at the seafloor/water interface, and T_m is the mantle potential temperature. C) The mesh is composed of irregular triangular elements. Node-spacing is finer towards the top surface of the model domain and along the transform and ridge boundaries. D) Zooming in on the mesh shows how the the elements become finer as the mesh approaches the transform plane. Elements along the transform and ridge segments are spaced at 1-km intervals.

on the sides of the model parallel to the transform fault are symmetric, while those perpendicular to the transform fault are open to convective flux. The base of the model is stress-free, allowing convective flux into and out of the model domain without drag from the underlying mantle. The imposed temperature at the surface of the model, which represents the seafloor/seawater interface, is $0°$, and the base of the model is fixed with the mantle potential temperature of $1300°C$. The surface of the model is meshed using a free-triangular grid, with finer grid spacing along the fault plane. The surface mesh is then extruded from the surface to the bottom, with increasing grid spacing, creating a mesh of prismatic elements with finer-spacing at shallow depths (Fig. 2.1). The mesh-spacing is 1-km along the RTF, including ridge segments and orthogonal offsets ≥ 5 km in length, and between 0 - 10 km depth. The element spacing varies such that there are 4 evenly spaced nodes along the offset for offsets of <5 km.

In addition to conductive heat loss, the COMSOL models incorporate advective heat loss due to the convective flux of the mantle. Brittle weakening in the shallow lithosphere reduces the effective viscosity and enhances passive mantle upwelling, which in turn, warms the center of the fault and cools the ridge-transform intersections. To derive the temperature structure underlying RTFs, I solved for the conservation of mass, momentum, and energy assuming steady-state, incompressible flow. Dislocation creep in the upper mantle was modeled using a temperature-dependent non-Newtonian power law (Hirth & Kohlstedt, 1995):

$$\dot{\varepsilon} = A(\sigma_1 - \sigma_3)^n \exp\left(-\frac{E}{RT}\right) \tag{2.1}$$

where $\dot{\varepsilon}$ is the uniaxial strain rate, $(\sigma_1 - \sigma_3)$ is the differential stress, T is the temperature, and R is the gas constant. The values of A, the pre-exponential factor, n, the stress exponent, and E, the activation energy used in the model were obtained from experiments on dry olivine (Hirth & Kohlstedt, 1995, for values see Table 2-S1 in the Supplement). These values were also used to calculate the viscosity due to creep, η_{creep}, as a function of temperature and strain rate:

$$\eta_{creep} = \frac{1}{4} \left(\frac{4}{3A} \right)^{1/n} \dot{\varepsilon}_{II}^{\frac{1-n}{n}} \exp \left(\frac{E}{nRT} \right) \tag{2.2}$$

Brittle deformation is approximated by computing the maximum shear stress, τ_{max}, as a function of the coefficient of friction, μ, the density of the lithosphere, ρ, the density of seawater, ρ_w, gravitational acceleration, g, depth, z, and cohesion, C:

$$\tau_{max} = \mu(\rho - \rho_w)gz + C \tag{2.3}$$

Equation 2.3 is based on the assumption that the maximum compressive principle stress, σ_1, is vertical, which is expected for mid-ocean ridge environments that are undergoing extension. For simplicity, this assumption is applied throughout the model domain, although it is acknowledged that along the transform fault plane the vertical stress is expected to be the intermediate principle stress, σ_2. Assuming σ_1 is vertical near the transform allows the fault to fail at slightly lower differential stresses than theoretically predicted. However, Roland *et al.* (2010) showed that this discrepancy has a negligible effect on the resulting flow field and temperature structure.

Following Chen & Morgan (1990), I then calculated an effective viscosity of the upper lithosphere, η_{fric}, that is limited by τ_{max} and the second invariant of the strain-rate tensor, $\dot{\varepsilon}_{II}$:

$$\eta_{fric} = \frac{\tau_{max}}{\sqrt{2\dot{\varepsilon}_{II}}} \tag{2.4}$$

Deformation occurs by the mechanism with the lowest viscosity at each point in the model space and an effective viscosity, η_{eff}, was used in the conservation of momentum to determine the flow field:

$$\eta_{eff} = \left(\frac{1}{\eta_{fric}} + \frac{1}{\eta_{creep}} + \frac{1}{\eta_{max}} \right)^{-1} \tag{2.5}$$

where η_{max} is a viscosity cap utilized to aid in model convergence. Following Roland *et al.* (2010), I computed an initial solution for mantle flow and temperature assuming a constant viscosity of $10^{19} Pa{\cdot}s$. The solution is subsequently iterated, systematically increasing η_{max} from an initial value, $\eta_0 = 10^{19} Pa{\cdot}s$, to $10^{24} Pa{\cdot}s$.

2.3 Results

The modeled RTF thermal structures depend primarily on the kinematic fault parameters, including fault segment length, transform offset length, and spreading rate. The area above the $600°C$ isotherm, A_T, for any given RTF fault segment is proportional to the segment length, and inversely proportional to the offset length and the spreading rate (Fig. 2.2). The increase in A_T with fault segment length can be attributed to an increase in conductive cooling and a decrease in passive upwelling under the transform with increasing distance from the ridge. Faster spreading rates at the ridges results in lithosphere that is thinner, warmer, and weaker and thus, A_T increases as spreading rate decreases.

Similarly, the effect of segmentation is to decrease A_T of the entire RTF system (the combined thermal area of all fault segments), with a more significant decrease for longer offsets (Fig. 2.2). The thermal structure of a segmented RTF system composed of a 25-km long fault segment separated from a 75-km long fault segment by an offset is shown in Fig. 2.2 (modeled thermal structures of the 6 other RTF geometries are presented in the Supplementary Information). The thermal structure of the RTF with a 2-km offset (Fig. 2.2B) is similar to that for the unbroken fault (Fig. 2.2A), with a reduction in A_T of only 8%, indicating that the proximity of the adjacent fault segments contributes to the seismogenic area of each segment. By contrast, the reduction in A_T when the offset is increased from 2 to 15 km is $\sim$22% (Figure 2.2C) and the depth to the $600°C$ isotherm for the segmented fault system (white line) is nearly indistinguishable from that of thermal models calculated for the two fault segments independently (black lines). This indicates that an offset

length of 15 km is long enough to thermally decouple the two adjacent fault segments. At greater offsets beyond this critical decoupling length, A_T will remain constant regardless of an increase in offset length, and converge to the solution for two independent fault segments.

As shown by Behn *et al.* (2007), calculations with a visco-plastic rheology results in a different geometry of the seismogenic area, but a similar prediction of A_T relative to a half-space cooling model. As such the area above the $600°C$ isotherm derived from the finite-element models on a single isolated fault, A_T, can be approximated by the scaling relation:

$$A_T = C_{600}L^{1.5}V^{-0.47} \tag{2.6}$$

where the constant, $C_{600} = 7.1 \times 10^{-3}$ km/yr^{-1} and the exponents on L and V are nearly the same as found by Boettcher & Jordan (2004), who fit the relation to the half-space cooling model. For single, unbroken faults of length L, $A_{unbroken} = A_T$ from equation 2.6. For segmented faults with very large offset lengths, A_T obtained from the three-dimensional models approaches that of two thermally independent, or decoupled, fault segments of length L_1 and L_2 (e.g., the 15-km offset in Figure 2.2). Thus I defined $A_{decoupled}$ as the sum of A_T for each fault segment length, given as

$$A_{decoupled} = C_{600}(L_1^{1.5} + L_2^{1.5})V^{-0.47} \tag{2.7}$$

To describe A_T for intermediate offset lengths, I first defined an area loss ratio:

$$R = \frac{A_{unbroken} - A_{combined}}{A_{unbroken} - A_{decoupled}} \tag{2.8}$$

where $A_{combined}$ is the sum of the thermal areas for the fault segments in a two-segment RTF system. When R equals 1, $A_{combined}$ equals $A_{decoupled}$. As the length of the offset approaches 0 km, $A_{combined}$ approaches $A_{unbroken}$, and R approaches 0. $A_{combined}$ is well-fit by the equation:
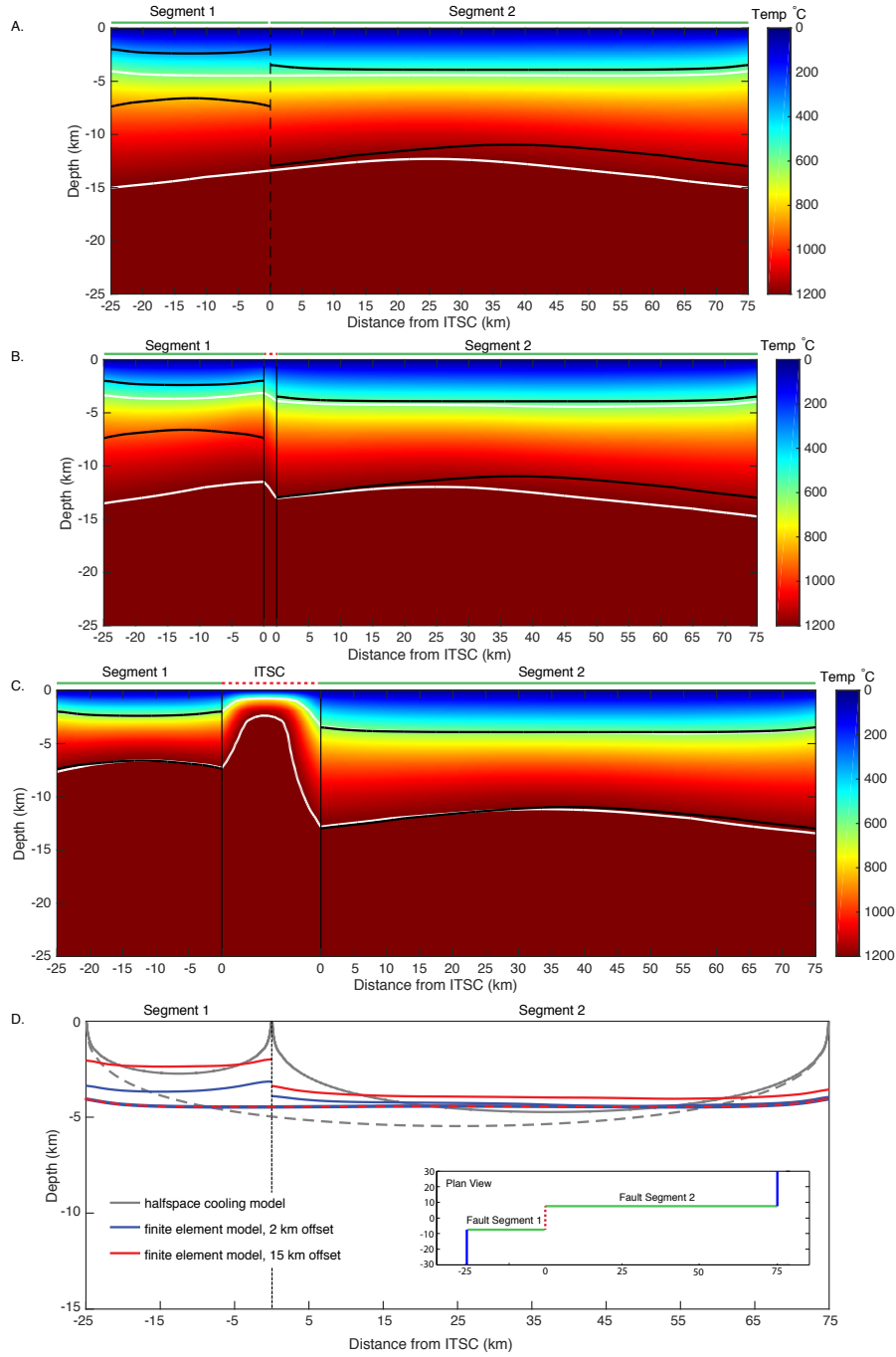
Figure 2.2: A - C: Temperature cross-section of an RTF. The top and bottom white lines denote 600°C and 1200°C isotherms from the modeled geometry. The top and bottom black lines denote the 600°C and 1200°C isotherms for a single 25-km long and 75-km long fault segment, respectively. A: An unbroken 100-km long RTF. B: A segmented RTF system comprised of a 25-km long fault segment separated from a 75-km long fault segment by a 2-km long offset. C: Same as in B except the offset length is now 15 km. Note that for the 15-km offset, the 600° isotherm for the segmented fault system (top white line) is nearly indistinguishable from that of the individual fault segments (top black lines), indicating that the two segments are nearly 100% decoupled. D: Temperature profiles for the segmented fault system comparing the results of the half space model, and the finite element model for both a 2-km and 15-km offset. Solid lines delineate the 600°C isotherm for the individual fault segments. Dashed lines denote the 600°C isotherm for the whole 100-km long fault. Slip rate in all panels is 8 cm/yr.

14

$$A_{combined} = A_{unbroken} \exp\left(\frac{-O}{O_C}\right) + A_{decoupled}\left[1 - \exp\left(\frac{-O}{O_C}\right)\right] \tag{2.9}$$

where O_C is the critical offset length that results in a reduction in seismogenic area corresponding to $R = 0.63$, which corresponds to $O_C = O_L$ (Fig. 2.3).
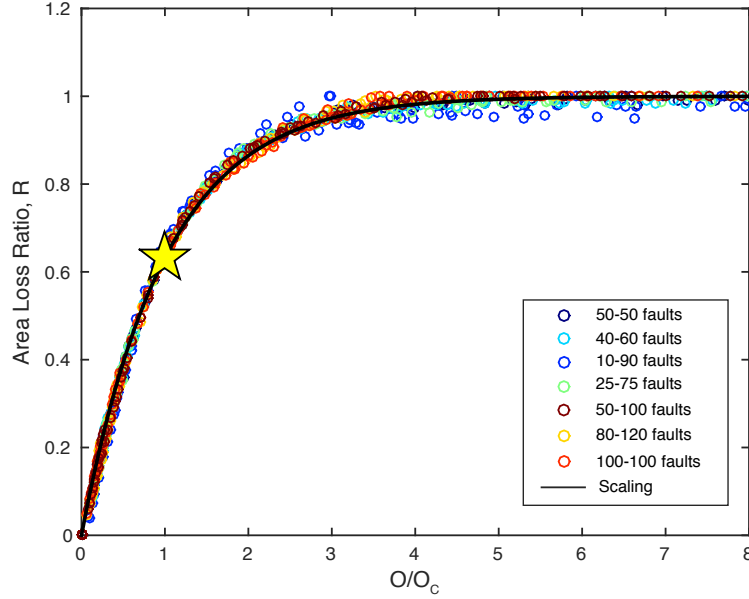

Figure 2.3: A plot of R versus the offset ratio, O_L/O_C. The colored circles represent data derived from the model. The black line results from using the scaled version of R and the scaling relation for O_C. The star indicates where the line has an offset ratio equal to 1.

A scaling relation for O_C (black line in Fig. 2.4) was developed, based on the fault segment lengths (L_1 and L_2) and slip rate (V):

$$O_C = C_O \frac{L_1^{1.5} + L_2^{1.5} - 0.1|L_1 - L_2|^{1.5}}{L_1 + L_2} L_0^{0.5} \frac{V}{V_0}^{-0.6} \tag{2.10}$$

where C_O is a constant $= 0.6144$, and the normalizing constants, L_0 and V_0, equal 1 km and 8 cm/yr, respectively. Figure 2.4 shows a plot of O_C derived from Equation 2.10 versus O_C derived from the models. Circle colors represent the 7 different model geometries. C_O is the average of the slope terms obtained from linear least squares regressions for each geometry. The critical offset length is shown for a series of segmented RTF geometries, wherein the two adjacent fault segments are the

15

same length (Fig 2.7). Each curve is generated using Equation 2.10 and a spreading rate of 8 cm/yr. The most significant changes in O_C, regardless of fault segment length, occur as the spreading rate increases from slow to intermediate rates (2 to 6 cm/yr). At moderate- to fast-spreading rates, the critical fault offset is typically ≤ 5 km, for fault segment lengths of 100 km or less.
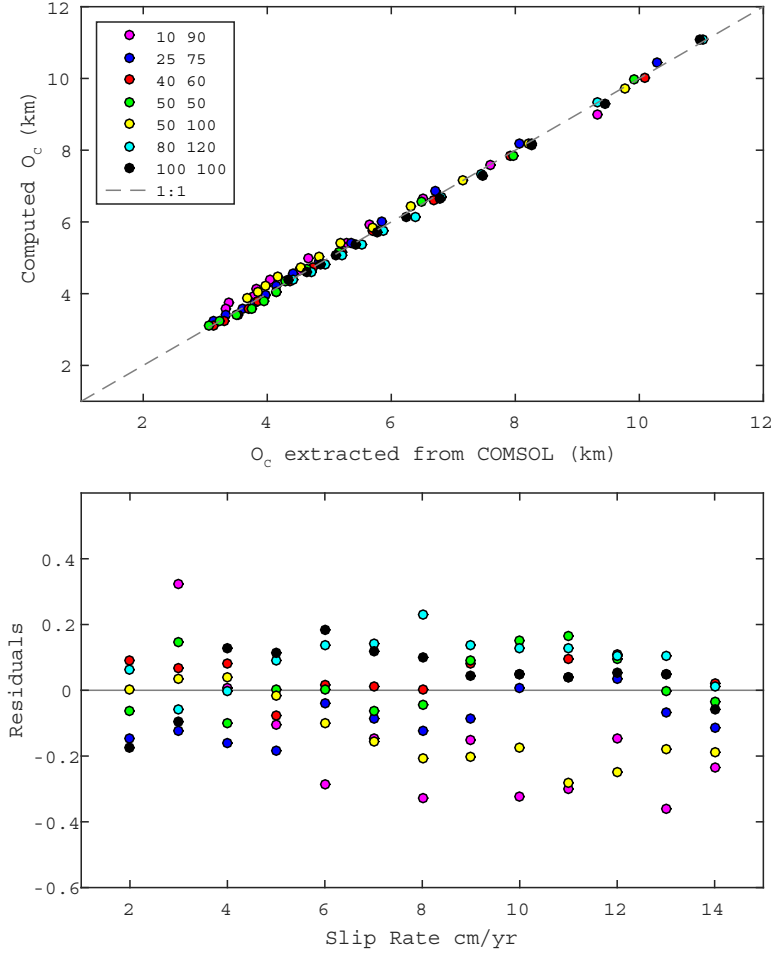
Figure 2.4: A) Plot of O_C derived from Equation 2.10 versus O_C derived from the models. Circle colors represent the 7 different model geometries. B) Plot of the residuals between the scaled O_C and O_C derived from the models, by slip rate.

2.4 Discussion

On continental strike-slip faults, earthquake ruptures have been observed to jump across discontinuities along the fault trace, and propagate onto adjacent faults or fault segments (Wesnousky, 1988,

2008; Oglesby, 2008). These studies suggest that there is a correlation between step discontinuities (lateral fault offsets) and the endpoints of historical ruptures on these faults. Wesnousky (2006) observed that there is an upper limit of offset length, ~3 to 4 km, above which earthquakes are unlikely to propagate. This dimension of fault step agrees with the findings from dynamic rupture modeling (Harris & Day, 1993), which suggest that rupture is unlikely to propagate across an offset >5 km. These observations are congruent with the results of this study, which indicate that for moderate- to fast-slipping faults, two adjacent fault segments will decouple starting at offsets $\geq$5 km. Dynamic rupture models also indicate that along with offset length, the orthogonality of the offset with respect to the fault trace is important (Wesnousky & Biasi, 2011), as is rupture velocity and the rate of change in the initial shear stress (Oglesby, 2008). These studies suggest that for slow-slipping RTFs, where O_C can be much larger than 5 km, the dynamics of rupture propagation are likely to limit the size of the largest earthquakes.

In the models, the thermal structure underlying offsets $\geq 2O_C$, and with spreading rates ≥ 4 cm/yr, was found to be the same as the thermal structure underlying a mature mid-ocean ridge segment. For offsets shorter than $2O_C$, or for slower spreading rates, a shallowing of the isotherms was still observed, but they had not converged to the solution for an infinitely long ridge. A similar correlation was observed between RTF offset length and the morphology of these offsets, with offsets shorter than $2O_C$ being defined by extensional basins and offsets equal to or longer than $2O_C$ being defined by ITSCs. For example, the western end of Blanco Ridge is terminated by the ~16-km long Cascadia Depression, which is $\sim 2O_C$, and is interpreted to be an ITSC based on the presence of a narrow ridge, flanked by symmetrically-spaced inwardly-facing fault blocks (Embley & Wilson, 1992). To the east, Blanco Ridge ends in the ~8-km long Gorda Depression, which is $\sim 1O_C$, and interpreted to be an extensional basin based on morphological similarities to mature pull-apart basins found on continental divergent wrench faults (Embley & Wilson, 1992). For offsets contained within basins, such as those on the Blanco Transform Fault, offset length was measured as the

straight line distance between adjacent fault strands, but may not represent full basin width. On the Quebrada, Discovery, and Gofar Transform Faults, where dredged basalts from within the ITSCs confirms the presence of young magmas (Pickle *et al.*, 2009), the offsets are all $>2O_C$. Although comparisons between the type of offset observed on an RTF and the predicted critical offset length are limited to where there are high enough resolution multibeam bathymetry data to discern offset morphology, these observations, in combination with the modeled thermal structures, suggest that full mantle upwelling and seafloor spreading may not occur at offsets less than $2O_C$.

In Chapter 3 I present a global compilation of RTF structure. Using this global dataset, I looked at the ratio of measured offset length, O_L, over O_C for 67 adjacent fault segments. The histogram plot presented in Figure 2.5 shows that the majority of offsets measured on RTFs are on the order of $4O_C$ or greater. This indicates that most adjacent fault segments in a segmented RTF system are thermally decoupled. Figure 2.6 shows a scatter plot of the O_L:O_C ratio versus slip rate of the RTF system. For moderate- to fast-slipping faults, the offset lengths are all $\sim 4O_C$ or greater, which agrees with the results from the finite element analysis that on faults with slip rates >8 cm/yr, two adjacent fault segments will be thermally decoupled.

A remarkable observation from a number of RTFs is that the largest earthquakes appear to repeatedly rupture the same fault patches and do not propagate through short (~ 10 km long) rupture barriers that separate the rupture zones (McGuire, 2008; Boettcher & McGuire, 2009; McGuire *et al.*, 2012; Wolfson-Schwehr *et al.*, 2014). In some cases, offsets larger than O_C coincide with the rupture barriers, such as occurs on the G2 segment of Gofar Transform Fault on the East Pacific Rise (e.g., McGuire, 2008), whereas other repeating ruptures are only bounded by small (<1 km) step-overs, or jogs, in the fault trace, such as found on the westernmost segments of Gofar (G3) and Discovery (D2) Transform Faults on the East Pacific Rise (Froment *et al.*, 2014; Wolfson-Schwehr *et al.*, 2014). Similarly, on Blanco Ridge, the most seismically active segment of the Blanco Transform Fault, two large repeating rupture patches have been identified (Boettcher &
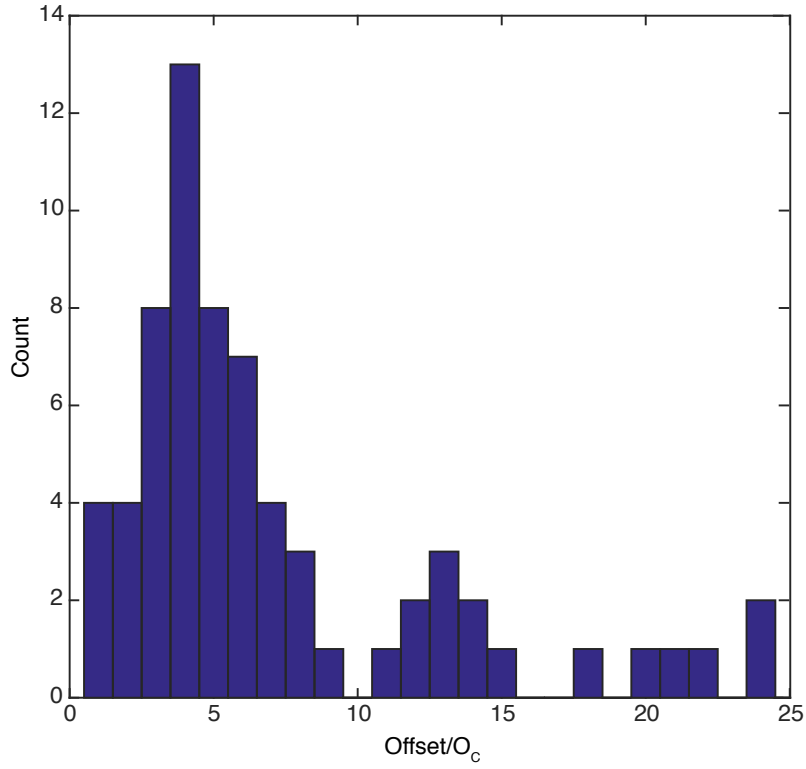
Figure 2.5: Histogram plot of O_L/O_C for 67 adjacent fault segments. Two fault segments are considered an adjacent pair if the offset between them is shorter than either of the two fault segment lengths and shorter than a maximum length of 50 km.
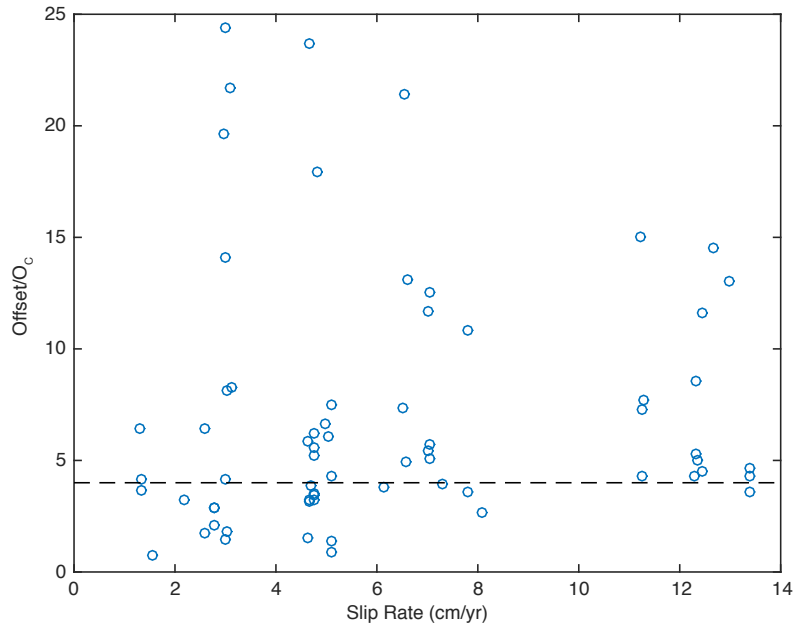

Figure 2.6: Scatter plot of O_L/O_C versus slip rate for 67 adjacent fault segments. The horizontal line denotes where the offset length equals $4O_C$.

McGuire, 2009), suggesting that a rupture barrier exists between them where no offset is resolved in the bathymetry data. The predicted values of O_C from equation 2.10 for segments of Gofar, Discovery, and Blanco are shown in Figure 2.7. The lengths of the discernible offsets on Blanco and Discovery are all greater than O_C, consistent with the lack of rupture propagation during the largest events on these faults. However, the repeating rupture patches do not extend from one ITSC to the next. Instead, some of their endpoints correlate with offsets and/or other structural features that are smaller than O_C (Froment *et al.*, 2014; Wolfson-Schwehr *et al.*, 2014). Thus, segmentation alone cannot explain why RTF earthquakes are small.
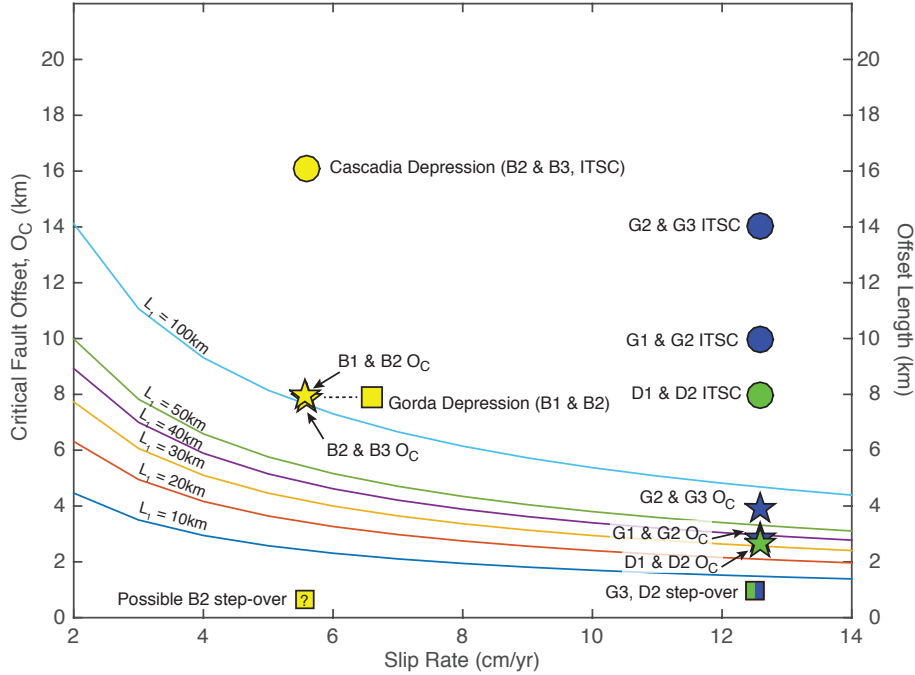

Figure 2.7: Critical fault offset length (left axis) and offset length (right axis) versus spreading rate. All spreading rates are obtained from version 2 of Global Strain Rate Model (Kreemer *et al.*, 2000). Lines represent O_C for segmented RTF systems composed of two fault segments of the same length ($L_1 = L_2$). The stars, circles, and squares denote O_C, ITSC length, and non-ITSC offsets (extensional basins, fault jogs), respectively for RTF segments discussed in the text. B = Blanco, G = Gofar, D = Discovery. The symbol for the Gorda Depression is offset laterally (in slip rate) for clarity. Numbering scheme for the segments follows that of Searle (1983).

Although a small number of faults with high-resolution bathymetric data have been discussed here, the vast majority of seafloor bathymetry is predicted using an inversion of global satellite

altimetry data, with which it is difficult to resolve features smaller, or closer together, than 12.5 km (Smith & Sandwell, 1997). It is possible, therefore, that segmentation is prevalent along RTFs on a scale that cannot be readily resolved in current datasets. These offsets, their effect on the underlying thermal structure of the fault, as well as secondary effects, such as enhanced damage in the fault zone and alteration (e.g., Roland *et al.*, 2012), may more fully explain why RTF earthquakes do not rupture the full fault area.

2.5   Conclusion

In this study, 3D finite-element analysis was used to determine the effect of lateral offsets on the underlying thermal structure of mid-ocean ridge transform faults, and a scaling relation was developed for the length of offset that significantly decouples adjacent fault segments (O_C). Using this scaling relation, predictions can be made about the thermal effect of any orthogonal offset on any RTF system. For moderate- to fast-slipping RTFs, the critical fault offset is typically ≤ 5 km, for fault segment lengths of 100 km or less. Most offsets resolved in bathymetric data on these faults are $> O_C$, consistent with the lack of observed rupture propagation across them. For all segmented RTF systems, regardless of spreading rate, full decoupling is achieved at $\sim 4O_C$. The endpoints of repeating rupture patches on RTFs appear to correspond to both offsets larger and smaller than O_C, which suggests that secondary effects of segmentation, such as variations in porosity, alteration of the fault rock, and enhanced hydrothermal circulation must limit the size of the largest earthquakes on RTFs. The ability to delineate offsets along RTFs is currently limited by the resolution of available bathymetric datasets, ~ 12.5 km for much of the world's oceans. The models presented in this study show that offsets on the order of 5 km or less are sufficient to significantly affect the underlying thermal structure. It is possible that segmentation of mid-ocean ridge transform faults is quite prevalent on a scale that we cannot currently resolve, and that this scale of offset plays a crucial role in the size and propagation of the largest expected earthquake on these faults.

2.6 Supplementary Information

Table 2-S1: Material Properties and Boundary Conditions for RTF Model Simulations

| Material Properties		
ρ_{lith}	Average lithospheric density	3300 kg/m3
ρ_w	Water density	1000 km/m3
η_0	Reference viscosity	1e19 $Pa{\cdot}s$
η_{max}	Maximum viscosity	1e24 $Pa{\cdot}s$
κ	Thermal conductivity	3 W/(mK)
C_P	Specific heat	1000 J/(KgK)
R	Gas constant	8.2134509999999992
A	Pre-exponential factor	110000
n	Stress exponent	3.5
E	Activation energy	520 KJ/mol
μ	Coefficient of friction	0.85
C	cohesion	20 MPa
g	Gravitation acceleration	-9.8 m/s2
Boundary Conditions		
$L_{(X)}$	Length of fault segment (e.g., L1)	See table 2-1 in main text
L_T	Length of unbroken transform	See table 2-1 in main text
O_L	Length of offset (ITSC)	See table 2-1 in main text
R_L	Length of ridge segment	50 km
V	Full spreading rate	2 - 14 cm/yr
Ts	Surface temperature	$0^{\circ}C$
Tm	Mantle potential temperature	$1300^{\circ}C$
Additional Variables		
A_T	Total area above $600^{\circ}C$ in a RTF system	
$A_{unbroken}$	Area above $600^{\circ}C$ in a RTF system with a single, unbroken fault	
$A_{decoupled}$	Area above $600^{\circ}C$ in a RTF system with two fault segments separated by a long ITSC such that they are thermally decoupled	
$A_{combined}$	Area above $600^{\circ}C$ in a RTF system with two fault segments separated by an ITSC	
O_C	Critical ITSC offset length (km)	
R	Area loss ratio (equation 2.8)	
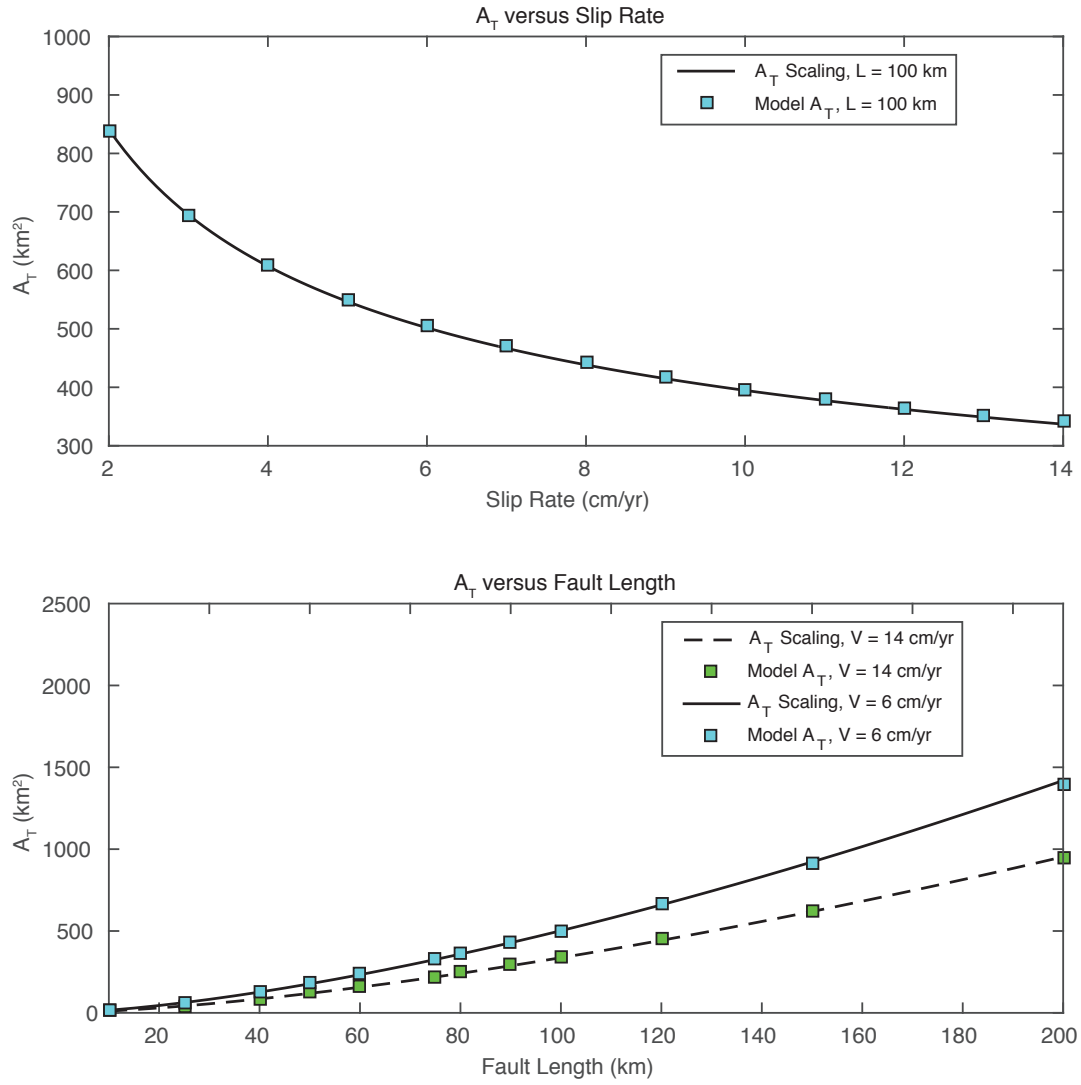
Figure 2.S1: A_T versus slip rate and fault length for our scaling relations (equation 8, black lines) and the finite element model (blue squares).
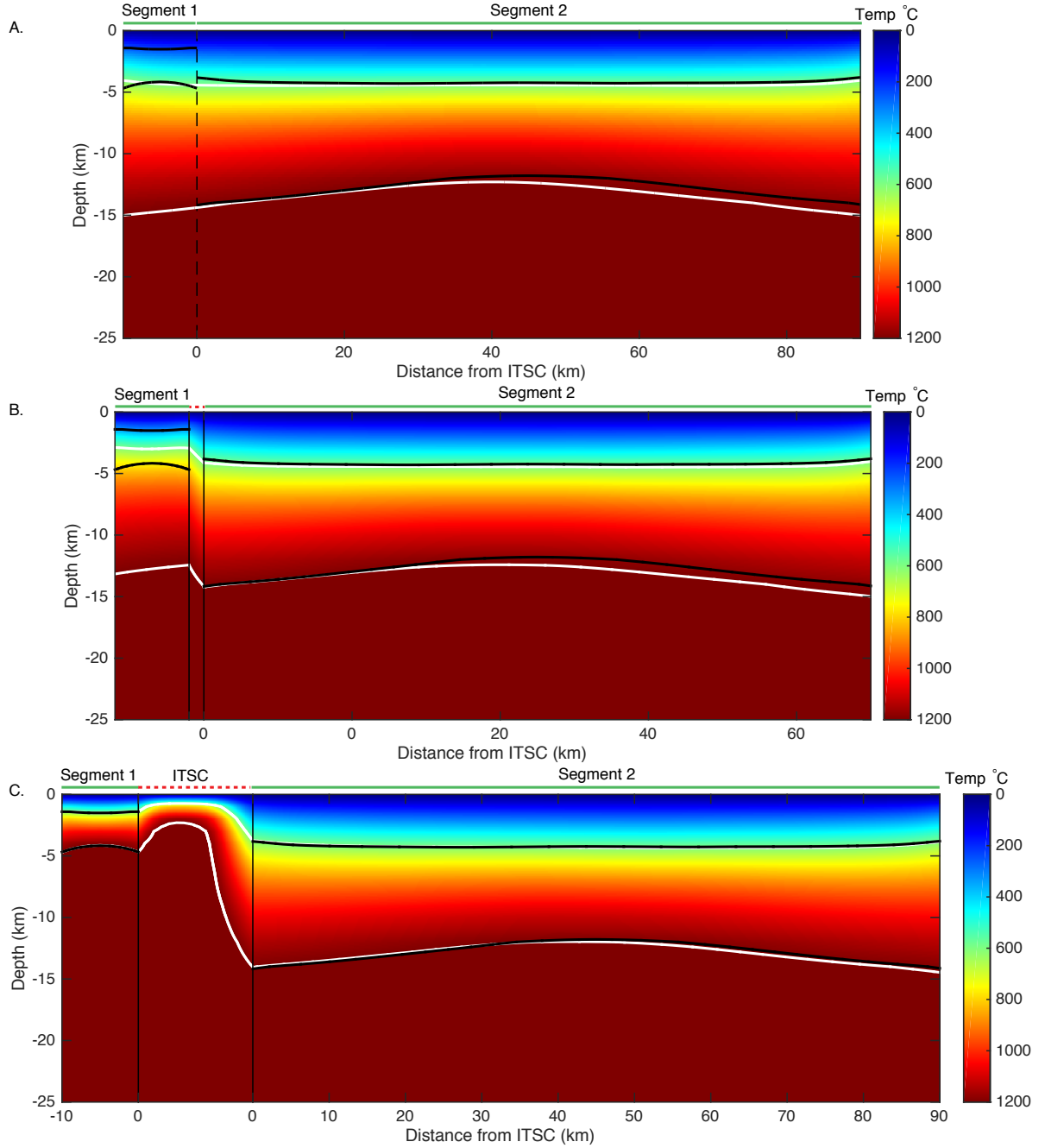
Figure 2.S2: A - C: Temperature cross-section of an RTF. Bottom white line denotes the 1200-degree C isotherm. Top white line denotes the 600-degree C isotherm. A: An unbroken 100-km long RTF. B: A segmented RTF system comprised of a 10-km long fault segment separated from a 90-km long fault segment by a 2-km long offset. C: Same as in B except the offset length is now 15 km. In both B & C, the top and bottom black line denote the 600° and 1200° isotherms for a single 10-km long and 90-km long fault segment, respectively. Note that for the 15-km offset, the 600° isotherm for the segmented fault system (top white line) is nearly indistinguishable from that of the individual fault segments, indicating that the two segments are nearly 100% decoupled. Slip rate in all panels is 8 cm/yr.
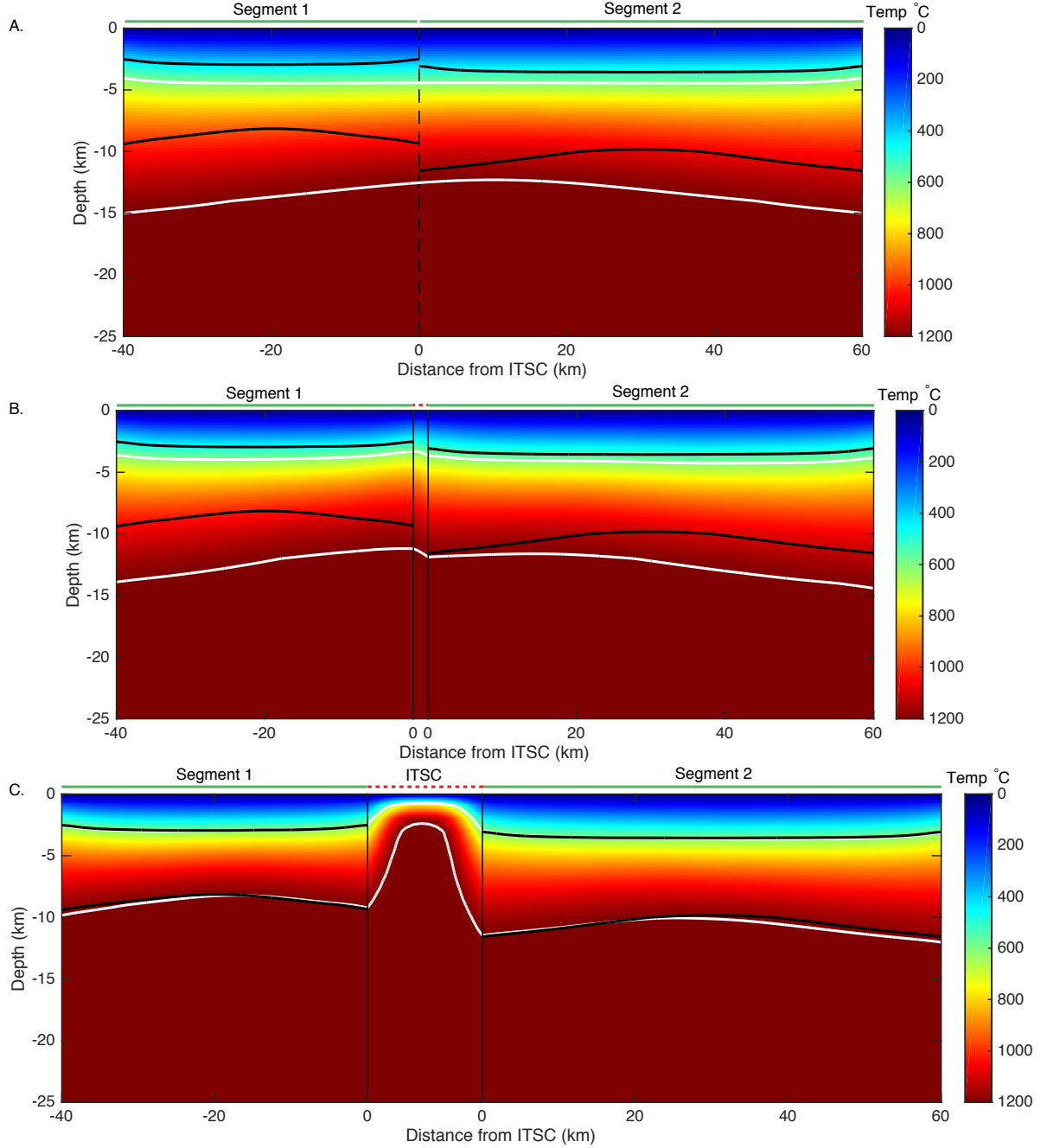
Figure 2.S3: A - C: Temperature cross-section of an RTF. Bottom white line denotes the 1200-degree C isotherm. Top white line denotes the 600-degree C isotherm. A: An unbroken 100-km long RTF. B: A segmented RTF system comprised of a 40-km long fault segment separated from a 60-km long fault segment by a 2-km long offset. C: Same as in B except the offset length is now 15 km. In both B & C, the top and bottom black line denote the 600° and 1200° isotherms for a single 40-km long and 60-km long fault segment, respectively. Note that for the 15-km offset, the 600° isotherm for the segmented fault system (top white line) is nearly indistinguishable from that of the individual fault segments, indicating that the two segments are nearly 100% decoupled. Slip rate in all panels is 8 cm/yr.
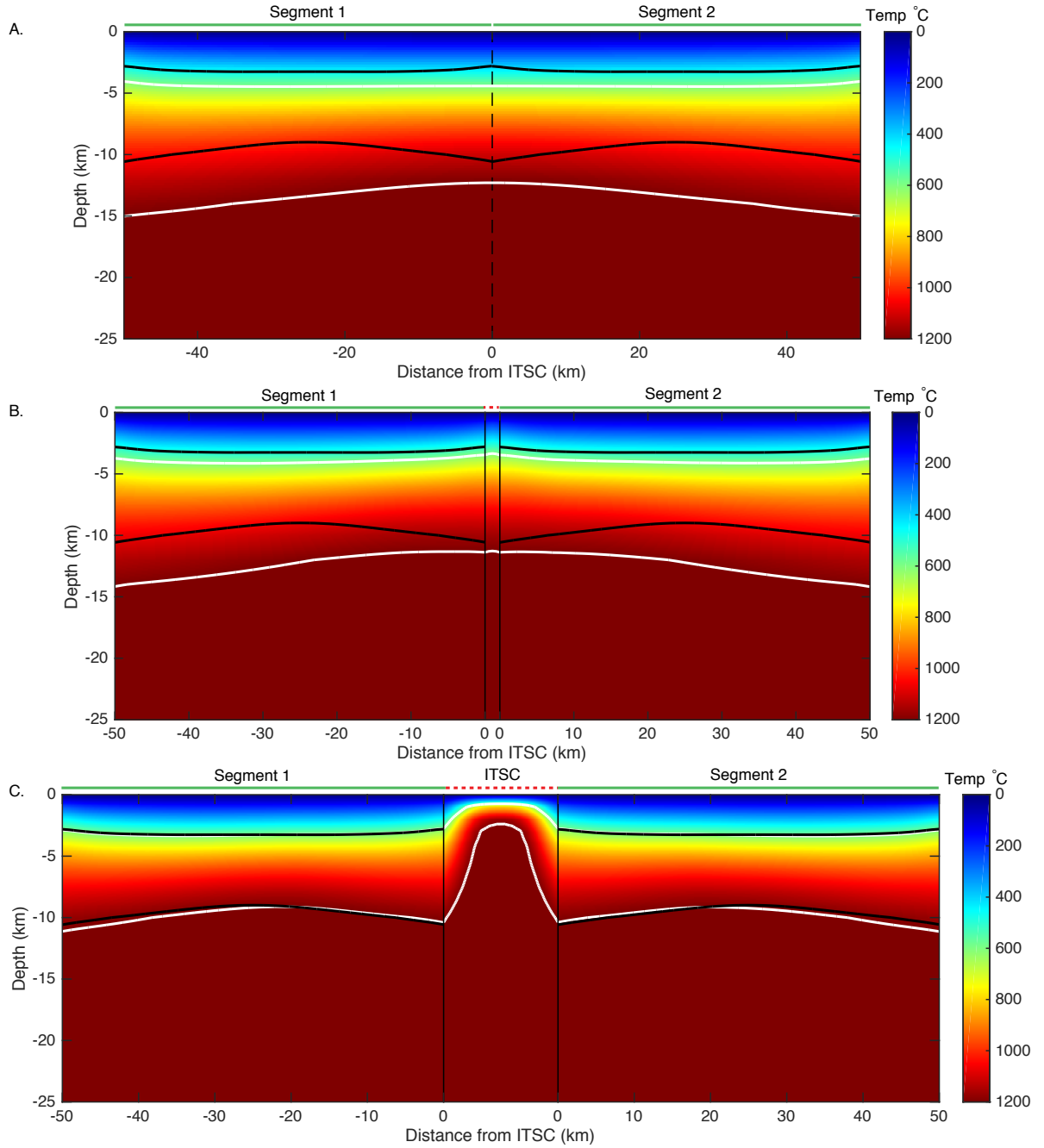
25

Figure 2.S4: A - C: Temperature cross-section of an RTF. Bottom white line denotes the 1200-degree C isotherm. Top white line denotes the 600-degree C isotherm. A: An unbroken 100-km long RTF. B: A segmented RTF system comprised of two 50-km long fault segments separated by a 2-km long offset. C: Same as in B except the offset length is now 15 km. In both B & C, the top and bottom black line denote the 600° and 1200° isotherms for a single 50-km long fault segment respectively. Note that for the 15-km offset, the 600° isotherm for the segmented fault system (top white line) is nearly indistinguishable from that of the individual fault segments, indicating that the two segments are nearly 100% decoupled. Dashed lines denote the 600° isotherm for the whole 100-km long fault. Slip rate in all panels is 8 cm/yr.
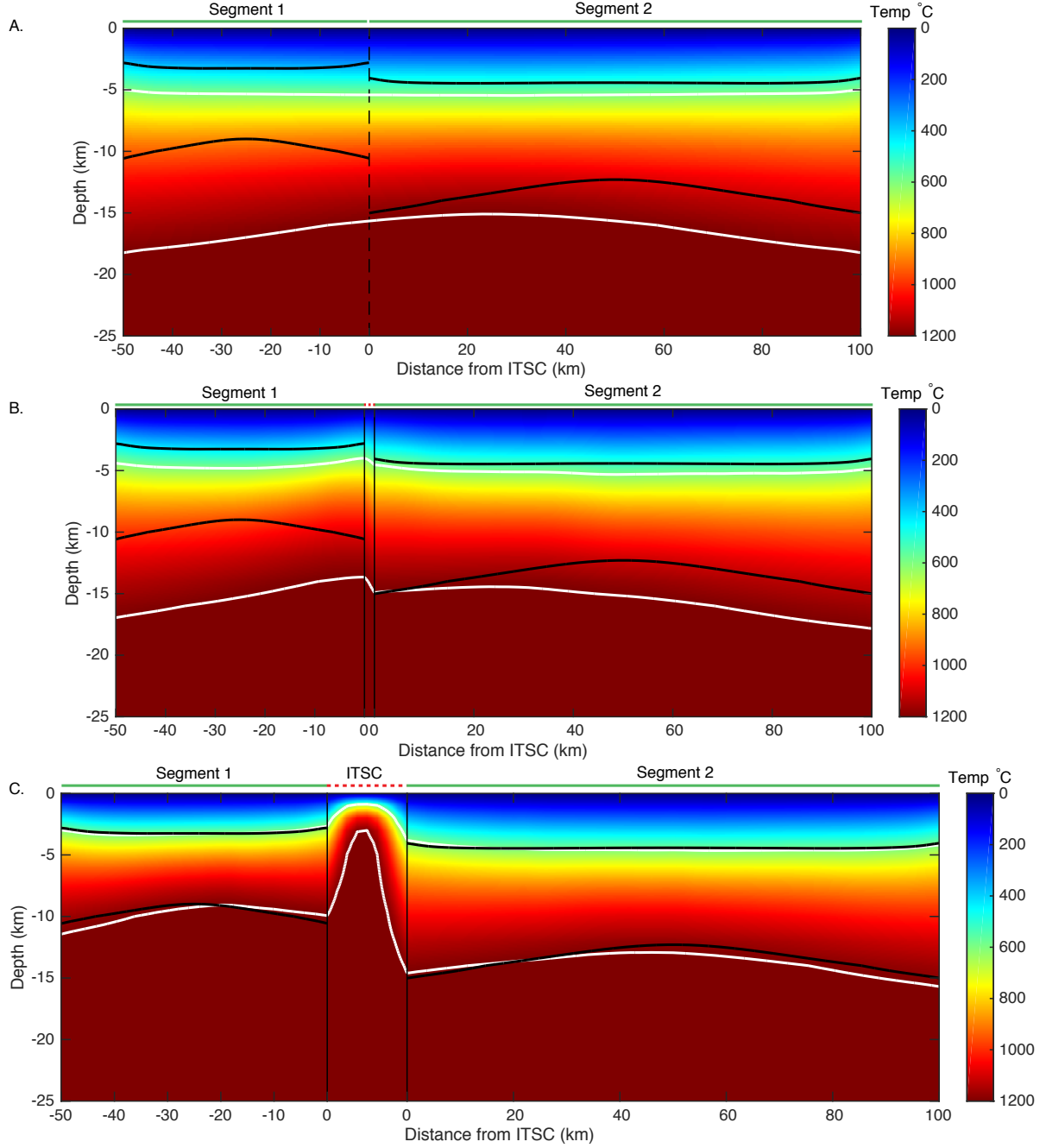
Figure 2.S5: A - C: Temperature cross-section of an RTF. Bottom white line denotes the 1200-degree C isotherm. Top white line denotes the 600-degree C isotherm. A: An unbroken 100-km long RTF. B: A segmented RTF system comprised of a 50-km long fault segment and a 100-km long fault segment separated by a 2-km long offset. C: Same as in B except the offset length is now 15 km. In both B & C, the top and bottom black line denote the 600° and 1200° isotherms for a single 50-km long fault segment and a 100-km long fault segment respectively. Note that for the 15-km offset, the 600° isotherm for the segmented fault system (top white line) is nearly indistinguishable from that of the individual fault segments, indicating that the two segments are nearly 100% decoupled. Slip rate in all panels is 8 cm/yr.
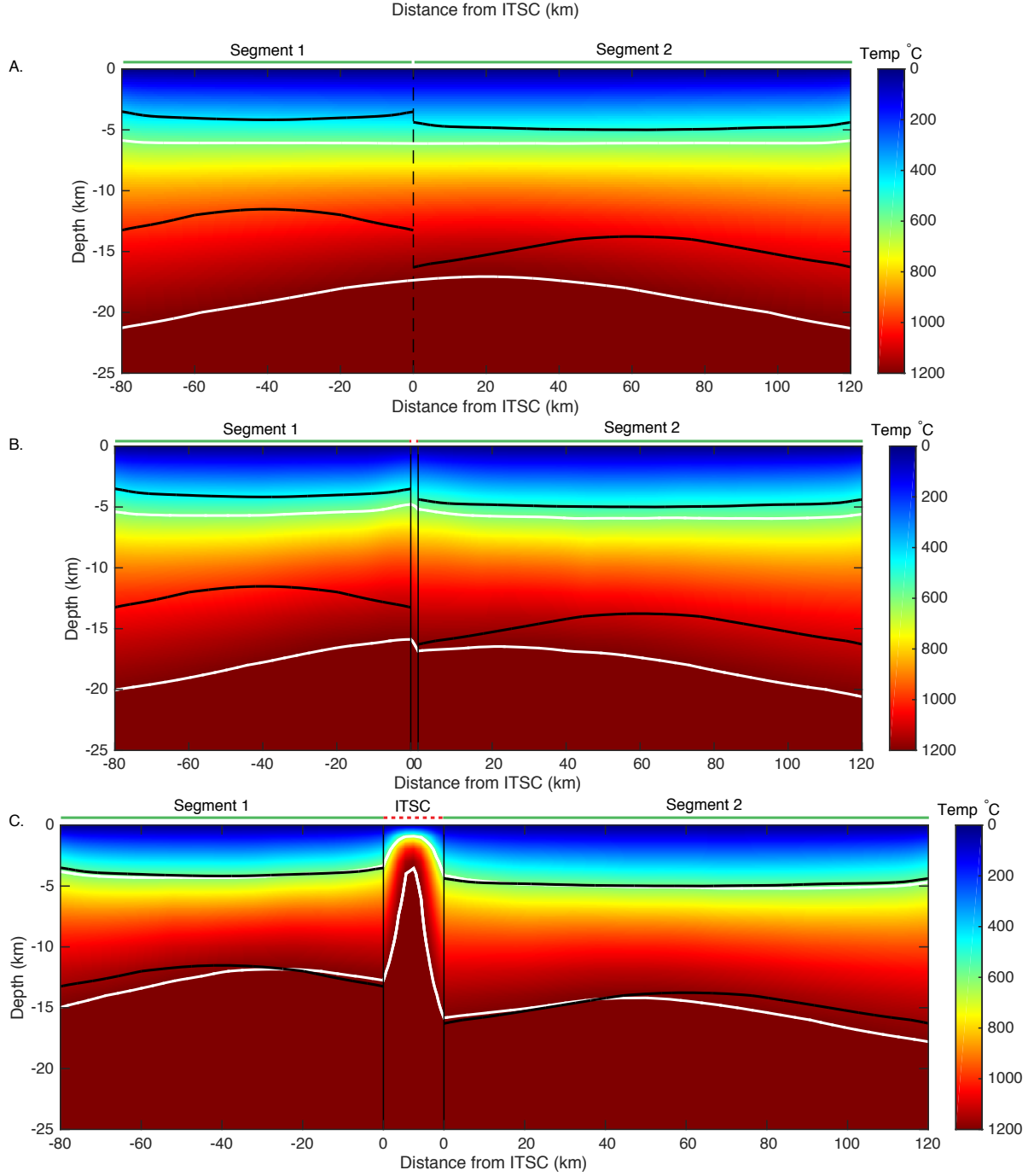
27

Figure 2.S6: A - C: Temperature cross-section of an RTF. Bottom white line denotes the 1200-degree C isotherm. Top white line denotes the 600-degree C isotherm. A: An unbroken 100-km long RTF. B: A segmented RTF system comprised of a 80-km long fault segment and a 120-km long fault segment separated by a 2-km long offset. C: Same as in B except the offset length is now 15 km. In both B & C, the top and bottom black line denote the 600° and 1200° isotherms for a single 80-km long fault segment and a 120-km long fault segment respectively. Note that for the 15-km offset, the 600° isotherm for the segmented fault system (top white line) is nearly indistinguishable from that of the individual fault segments, indicating that the two segments are nearly 100% decoupled. Slip rate in all panels is 8 cm/yr.
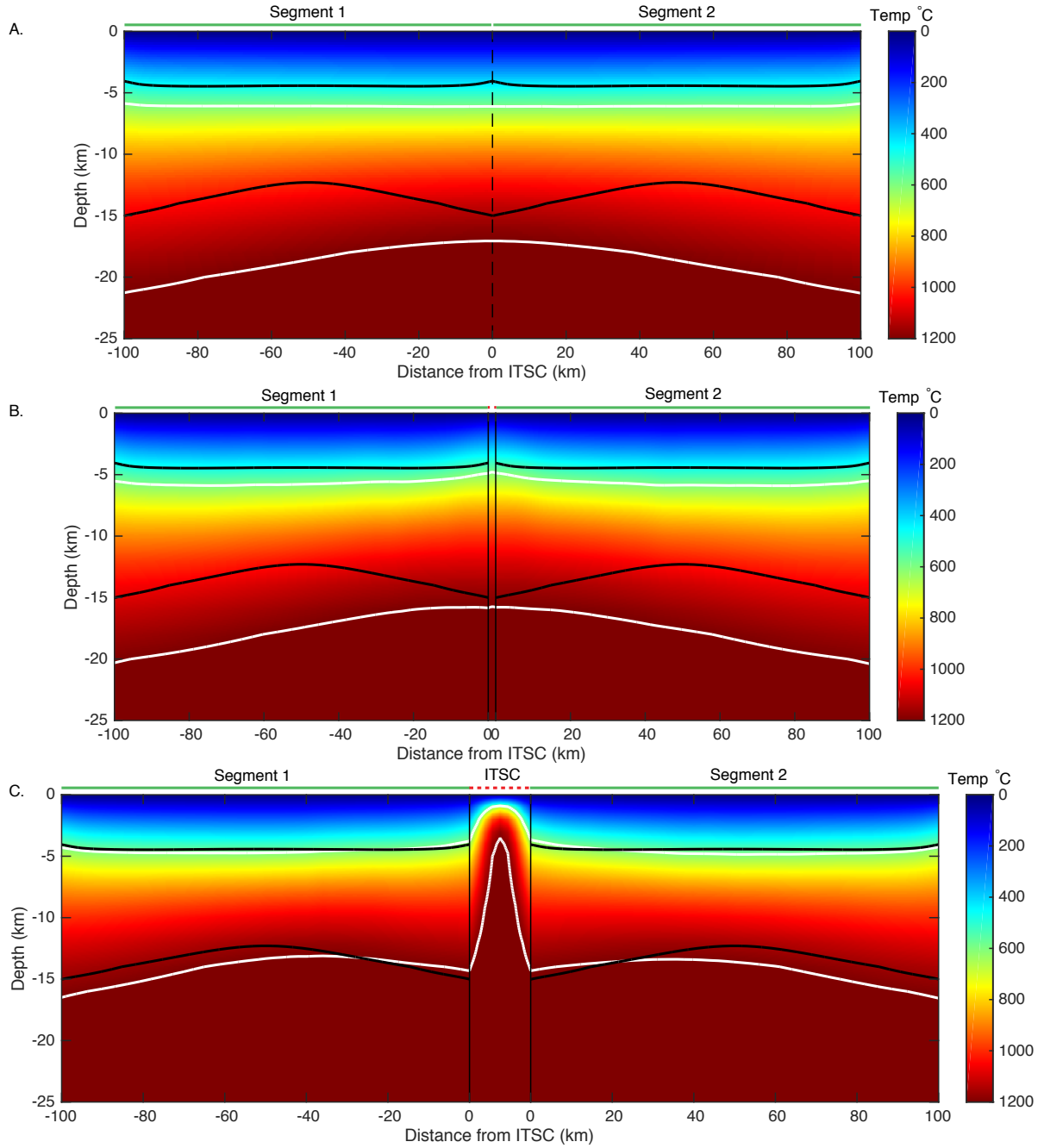
28

Figure 2.S7: A - C: Temperature cross-section of an RTF. Bottom white line denotes the 1200-degree C isotherm. Top white line denotes the 600-degree C isotherm. A: An unbroken 100-km long RTF. B: A segmented RTF system comprised of two 100-km long fault segments separated by a 2-km long offset. C: Same as in B except the offset length is now 15 km. In both B & C, the top and bottom black line denote the 600° and 1200° isotherms for a single 100-km long fault segment respectively. Note that for the 15-km offset, the 600° isotherm for the segmented fault system (top white line) is nearly indistinguishable from that of the individual fault segments, indicating that the two segments are nearly 100% decoupled. Slip rate in all panels is 8 cm/yr.

3 | A GLOBAL CHARACTERIZATION OF OCEANIC TRANFORM FAULT STRUCTURE AND THE EFFECTS OF SEGMENTATION ON GLOBAL SCALING RELATIONS

3.1 Introduction

Mid-ocean ridge transform faults (RTFs) are strike-slip faults that offset the mid-ocean ridge system and accommodate motion from seafloor spreading. Oceanic transforms are typically viewed as geometrically simple, with fault lengths readily constrained by the ridge-transform intersections (Wilson, 1965b; Menard & Atwater, 1968; Searle, 1983; Fox & Gallo, 1984; Sandwell, 1986; Fox & Gallo, 1989). The relative simplicity of their geometry, combined with well-constrained slip rates, makes them an ideal environment for studying strike-slip earthquake behavior (e.g., Parson & Searle, 1986; Boettcher & Jordan, 2004; Willoughby & Hyndman, 2005; Gregg *et al.*, 2006; Roland & McGuire, 2009; McGuire *et al.*, 2012; Sykes & Ekström, 2012). Early studies looking at the structure of RTFs relied on towed seismic surveys, gravity and magnetics data (Wilson, 1965a,b; Hey, 1977; Bird *et al.*, 1998), sidescan sonar (Searle, 1983, 1986; Taylor *et al.*, 1994), and singlebeam echosounders (Macdonald *et al.*, 1979, 1986). Although these data provide profound insight into the structure of the seafloor, the coverage and resolution of the data are quite variable, and analysis can be subjective. Recent global bathymetric data compilations (e.g., GEBCO World Map 2014, the Smith and Sandwell Global Topography dataset (Smith & Sandwell, 1997; Smith, 1998; Sandwell *et al.*, 2014), and The Global Multi-Resolution Topography (GMRT) synthesis (Ryan

et al., 2009)), along with several high-resolution multibeam and sidescan sonar surveys over oceanic transform faults (e.g., Lonsdale, 1978; Fornari *et al.*, 1989; Embley & Wilson, 1992; Goff *et al.*, 1993; Lonsdale, 1994; Dziak *et al.*, 2000; Wolfson-Schwehr *et al.*, 2014), that have shown that the geometry and structure of these faults can actually be quite complex.

Smith & Sandwell (1997) and Sandwell *et al.* (2014), provide global bathymetric maps of the seafloor compiled by inverting satellite altimetry data of the sea surface to obtain seafloor depth, and constraining these depths with the inclusion of multibeam and singlebeam sonar data where available. The latest version of this map (v.18.1, 2014) has a maximum global resolution of ∼5 km. Although this represents essentially a twofold increase in data resolution from the previous version, and has already led to the discovery of around 20,000 new seamounts, it is still not sufficient to capture the finer bathymetric details. Figure 3.1 shows a progression of resolution from estimated bathymetry (inverted from satellite altimetry data, resolution ∼12.5 km (Smith & Sandwell, 1997)) down to multibeam sonar bathymetry with a resolution of 200 m. In the top panel, which shows the estimated bathymetry only, the mid-ocean ridge system is discernible, but the number and structure of RTFs is not resolved. The middle panel shows the same dataset as the top, however it has been blended with soundings from a multibeam sonar survey. Inclusion of multibeam data in global grids not only provides a clearer image of the seafloor in that area, but also helps constrain the depth estimates from the altimetry data. The view of the MOR system cutting through this image is now clearer and individual RTFs can be seen in the data. However, it is not until the complete multibeam bathymetry coverage (bottom panel), that the true complexity of the seafloor starts to become evident. Where the presence of the East Pacific Rise (EPR) and perhaps 2 or 3 transforms could just be made out in the previous image, it is now seen that there are three distinct segmented RTF systems, each one composed of two-or-more individual fault strands. Sitting just north of the middle fault system is a possible nanoplate (Forsyth *et al.*, 2007; Wolfson-Schwehr *et al.*, 2014), which is, for the most part, indiscernible in the predicted bathymetry.

Predicted bathymetry
Data resolution: ~12.5 km

Predicted bathymetry blended with
shipborne sonar soundings
Data resolution: ~1.8 - 12.5 km
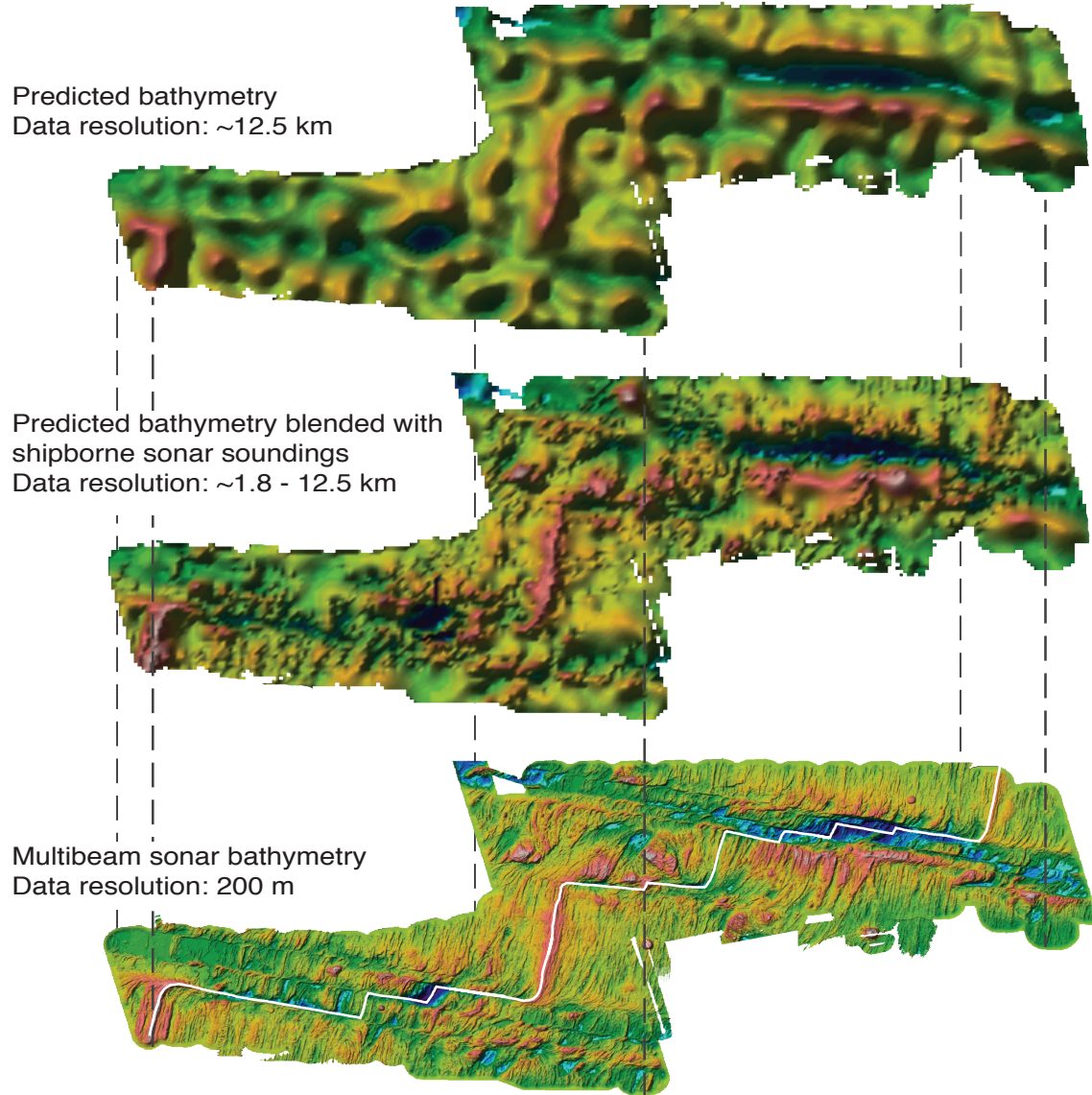
Multibeam sonar bathymetry
Data resolution: 200 m

Figure 3.1: Increasing progression of data resolution, from predicted bathymetry on the top to multibeam sonar bathymetry on the bottom. As the data resolution increases, the true complexity of the QDG fault systems becomes clear. Data credits: Top 2 images: Smith & Sandwell global topography dataset (v. 12.1; Smith & Sandwell, 1997). Bottom image: EM300 survey conducted in 2006. Plate boundary from (Pickle et al., 2009).

Segmentation of an RTF divides the fault up into a series of two-or-more parallel or subparallel fault segments that are laterally offset from one another by either a fault step, extensional basin, or intra-transform spreading center (ITSC) (Searle, 1983; Gregg *et al.*, 2006, 2009; Wolfson-Schwehr *et al.*, 2014), thereby decreasing the overall effective length of the fault system. The physical breakup of the fault into multiple strands is thought to occur primarily as a response to changes in plate-motion direction that caused the fault to undergo a period of extension (Menard & Atwater, 1968; Fox & Gallo, 1989; Lonsdale, 1994; Pockalny *et al.*, 1997; Gregg *et al.*, 2006; Behn *et al.*, 2007). On intermediate- and fast-slipping faults, where the lithosphere is hot and thin, extension can lead to the formation of fissures near the fault trace that allow melt to extrude, resulting in what is known as a "leaky" transform fault (Kastens *et al.*, 1979; Murton, 1986; Searle, 1986). Under continued extension, the fissures may coalesce, forming pull-apart basins and eventually an ITSC (e.g., the Siqueiros Transform Fault, Fig. 3.2, Pockalny *et al.*, 1997). On slower slipping transform faults, where the lithosphere is thicker and colder, extension may lead the formation of basins in which the extension is primarily accommodated through normal faulting (e.g., the Blanco Transform Fault, Embley & Wilson, 1992). Recent (over the last ~2 to 3 myr) 1 to 5° counterclockwise changes in spreading direction between the Pacific and Cocos plates (Carbotte & Macdonald, 1994) put the right-stepping Clipperton Transform Fault (10°N, ~10.6 cm/yr) under compression, while the left-stepping Siqueiros Transform Fault, ~200 km to the south (8°N, ~12.4 cm/yr) was put under extension (Macdonald *et al.*, 1992; Pockalny, 1997; Pockalny *et al.*, 1997). The compression across the Clipperton transform prevented the fault and ridges from being able to quickly adjust to the new direction in plate motion, resulting in a period of spreading in a direction that was intermediate between the new direction and the old. The compressional stresses caused the formation of median ridges. The younger side of the inactive fracture zone realigned to the new spreading direction relatively quickly, while the older side remained longer in the intermediate phase. This led to a zone of extension at the ridge-transform intersection, resulting in fissures and melt extrusion that formed

the ridge-intersection highs that are visible today. The Siqueiros Transform Fault was able to adjust

to the changes in plate motion direction relatively quickly compared to Clipperton. Extension along

the fault led to fissures and melt extrusion as described above. Each counterclockwise change in

spreading direction resulted in the formation of transverse flexural ridges and the development of
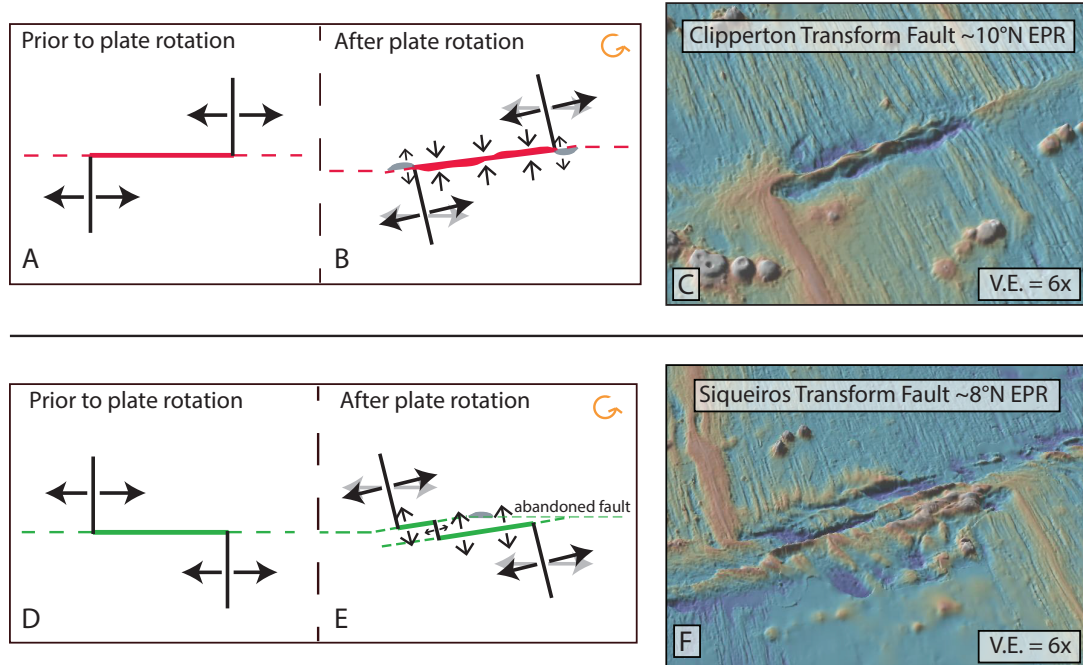
an ITSC (Fig. 3.2; Pockalny *et al.*, 1997).

Figure 3.2: A) A right-stepping transform fault. B) The same fault during a counterclockwise change in plate motion direction. The arrows represent the compressional and extensional stresses experienced by fault during the adjustment. The red thickened zones on either side of the transform represent median compressional ridges. The gray patches represent extensional ridge-transform intersection highs. C) An example of this geomorphic effect of a change in plate motion can be seen in the Clipperton Transform Fault. D) A left-stepping transform fault. E) The same fault as in D during a counterclockwise change in plate motion direction. The arrows represent the extensional stresses experienced by fault during the adjustment. There may also be extension along the fracture zones and abandoned fault traces, leading to normal faulting and the formation of extensional ridges on the older side of the fault (gray patches). F) An example of this geomorphic effect of a change in plate motion can be seen in the Siqueiros Transform Fault. Figure is based on (Pockalny *et al.*, 1997)

Slip along RTFs is partitioned into seismic and aseismic components, with the majority of slip

occuring aseismically (Brune, 1968; Bird *et al.*, 2002; Boettcher & Jordan, 2004; Frohlich & Wetzel,

2007). Seismicity on RTFs appears to be strongly controlled by the underlying thermal structure

of the fault. RTF earthquake focal depths (Abercrombie & Ekström, 2001; Braunmiller & Nábělek,

2008; Roland *et al.*, 2010), combined with results from laboratory friction experiments (Boettcher *et al.*, 2007), indicate that the seismogenic zone is limited by the 600°C isotherm. Boettcher & Jordan (2004) computed a set of global scaling relations for RTFs that relate the physical fault parameters, length (L) and slip rate (V), to the largest expected earthquake (Mc) and the total seismic moment. Combining the length and slip rate, the seismogenic area (A_T) can be calculated using the half-space cooling model:

$$A_T = C_T L^{3/2} V^{-1/2}, \tag{3.1}$$

where the constant C_T depends on the reference isotherm chosen as the base of the seismogenic zone ($4.1x10^{-3} km/yr^{1/2}$, for 600°C), and V is the slip rate of the fault. Boettcher & McGuire (2009) revisited the scaling relations, using an additional 10 years of data to verify the success of the relations, and determined a new scaling relation for the expected duration of seismic cycles on RTFs. The results from these studies indicate that there is a global seismic moment deficit on mid-ocean ridge transform faults, and the largest earthquakes on these faults do not rupture the full fault area (Boettcher & Jordan, 2004; Boettcher *et al.*, 2009). Additionally, there are some faults that behave as exceptions to the rules. On the Clipperton Transform Fault at 10°N on the EPR, the largest observed earthquakes are much bigger and occur less frequently than expected (Boettcher & Jordan, 2004; Boettcher & McGuire, 2009). Conversely, on the Quebrada Transform Fault at 4°S on the EPR, large repeating earthquakes do not occur at all. The exceptions suggest that RTF structure and along-strike mechanical properties are likely oversimplified in the global scaling relations.

To better determine the resolution of structural complexity on RTFs, as well as the effect this complexity may have on the global scaling relations, fault structure is delineated on a global scale. Individual multibeam sonar surveys are used in conjunction with the Smith and Sandwell Global Topography dataset (v. 18.1) and the Global Multi-Resolution Topography synthesis. This study

primarily focuses on the determination of the prevalence of RTF segmentation, but other structural complexities, such as median ridges versus valleys, anomalously rotated abyssal fabric, and transverse ridges are also noted. The presence of intra-transform ridges and anomalously rotated seafloor fabric suggests that the fault may have recently undergone, or may be still under, compression. During compression, increased normal stress across the fault may lead to larger earthquakes and higher seismic coupling. The Clipperton Transform Fault has both a median ridge (Pockalny, 1997) and anomalously rotated abyssal hill fabric (Sonder & Pockalny, 1999; Croon *et al.*, 2010), and is oriented such that every time the Pacific Plate undergoes a small counterclockwise change in plate motion direction, the Clipperton Transform Fault undergoes compression. Fault segmentation, such as shown along the Siqueiros Transform Fault (Fig. 3.2F), breaks the fault into a series of smaller fault segments. It is possible that combining all fault segments with offsets ≤35km in the original scaling analysis of Boettcher & Jordan (2004) resulted in a computed seismic coupling coefficient that fell below the true value. The purpose of this study is to investigate whether incorporating more realistic RTF segmentation significantly changes the global RTF scaling relations. Specifically, the expectation is that with segmentation, the seismic coupling should increase and the largest events should rupture more of the total seismogenic area.

3.2 Global Characterization

The primary datasets used for the characterization study were the Smith and Sandwell global topography dataset (v. 18.1), gridded at a resolution of 1 arc-minute (∼1.8 km at the equator; Smith & Sandwell, 1997), and the Global Multi-Resolution Topography (GMRT) synthesis (Ryan *et al.*, 2009), which includes multibeam sonar swath bathymetry gridded at a 100-m resolution, gridded multibeam bathymetry survey data at a variety of resolutions, gridded bathymetry data from the General Bathymetric Chart of the Oceans (GEBCO, 2014) at a resolution of 30 arc-seconds (∼1 km at the equator), and gridded bathymetry data from the International Bathymetric Chart of

the Arctic Ocean (IBCAO, v. 2.23) at a 2-km resolution. In addition, two multibeam sonar surveys, a Seabeam 2112 survey (200-m resolution) in 2006, and a Kongsberg Maritime EM302 survey (75-m resolution) in 2008, were used to delineate fault structure on the Quebrada, Discovery, and Gofar (QDG) Transform Faults located at ∼4°S on the EPR. These two surveys were cleaned and processed in CARIS HIPS (v. 6.4) and visualized in Fledermaus (v. 7). In some cases, available multibeam bathymetry grids were downloaded via GeoMapApp using the Marine Geoscience Data System, and imported into ArcGIS to aide in interpretation. Literature searches were also done to find any previous structural interpretations of each transform fault. All data were unprojected and displayed using the World Geodetic System (WGS) 84 ellipsoid. Therefore, all length measurements were made taking into account the curvature of the Earth.

Oceanic transform faults were included in the compilation if they were easily discernible in the data and had clear endpoints. To aide in the delineation of these features, the Present-day Plate Boundaries model from the University of Texas Institute of Geophysics Plates Project (Coffin et al., 1998) was also loaded in to ArcGIS. For each transform fault, length was measured from one endpoint to the other following a great circle. In the case of ridge-transform faults, the distance from each ridge-transform intersection to the nearest discernible ridge discontinuity was also measured. The proportion of median ridge to median valley for each fault was estimated by visual inspection. The presence of defined fracture zones, abyssal hill fabric, and transverse ridges were also noted. For segmented fault systems, the number and length of individual fault segments and their corresponding offsets were measured. Two adjacent faults were considered strands of the same segmented fault system if the adjoining offset is shorter than the length of either fault and less than a maximum length of 50 km. This upper bound is the result of three-dimensional finite element modeling on the effect of segmentation on the underlying thermal structure (see Ch. 3) which shows that even for slow-spreading RTF systems, two adjacent fault segments are fully thermally decoupled at distances of 50 km. Fifty kilometers is also approximately the scale of uncertainty in earthquake locations from

37

the Global Centroid Moment Tensor Project (Global CMT) catalog for mid-ocean ridge transform faults (Ekström *et al.*, 2012; Wolfson-Schwehr *et al.*, 2014), which becomes important during the scaling relation analysis.

In total, 202 individual fault segments were digitized, comprising 95 single-segment faults and 37 segmented fault systems (Fig. 3.3, Table 3-S1). Segmentation was found on ridges that represent the full range of spreading rates, from faults on the ultra-slow portions of the Southwest Indian Ridge and the Australian-Antarctic Ridge (< 2 mm/yr), to faults on the ultra-fast segment of the East Pacific Rise (>13 mm/yr). Slip rates for this study were obtained from the Global Strain Rate Map Project (GRSM, v. 1.2, Kreemer *et al.*, 2000). Segmentation is most prevalent on the EPR, hosting 29 of the 106 segmented fault strands ($\sim27\%$). These 29 individual fault segments comprise 9 segmented RTF systems and represent all but one of the faults measured on the EPR. The Mid-Atlantic Ridge has 23 segmented fault strands ($\sim22\%$), comprising 9 segmented RTFs out of the 35 fault systems measured on the ridge. It is interesting to note that although segmentation was observed across the range of MOR spreading rates, unsegmented faults were not. With the exception of the Clipperton Transform Fault, which has a slip rate of ~106 mm/yr and is the only fault on the EPR under compression, no other single-segment faults are found at slip rates above ~90 mm/yr. This slip rate also coincides with the transition from intermediate to fast spreading (Dick *et al.*, 2003).

Abyssal hill fabric, bands of topographic highs that trend approximately parallel to the mid-ocean ridge axis, are thought to cover the majority of the seafloor, except where buried by sediment (Dietz *et al.*, 1954; Menard & Atwater, 1968; Searle, 1984; Gallo *et al.*, 1986). The orientation of abyssal hill fabric often changes as it reaches the ridge-transform intersection, and begins to curve into the transform fault (Lonsdale, 1978; Fox & Gallo, 1984; Fornari *et al.*, 1989), reflecting the change in the stress regime from a primarily ridge-normal extensional stress, to a transform parallel shear stress. It is this rotation that gives abyssal hills their characteristic "J-shape" along transform
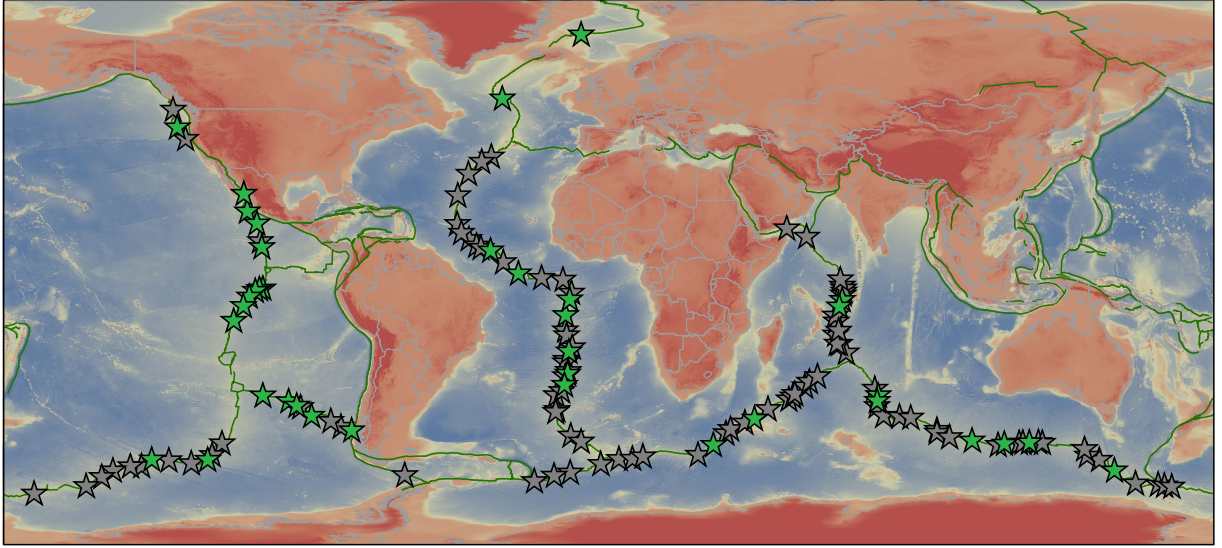
Figure 3.3: Global map showing the location of segmented (green stars) and non-segmented (gray stars) mid-ocean ridge transform faults. There are 132 total fault systems: 37 segmented fault systems comprised of two or more fault segments, and 95 single-segment faults. Map data derived from the global topography dataset (ver. 17.1; Smith & Sandwell, 1997). Plate boundary model (Coffin *et al.*, 1998).

fault and fracture zone boundaries (Searle, 1983; Sonder & Pockalny, 1999; Croon *et al.*, 2010). Sonder & Pockalny (1999) and Croon *et al.* (2010) noted the presence of "anti-J shape" abyssal hills along the Clipperton (EPR), and the Menard and Pitman (both on the Pacific-Antarctic Ridge) Transform Faults, and suggested that these anomalously rotated hills formed during periods of increased compression along the fault, brought about by changes in plate-motion direction. This compression would lead to increased normal stress across the fault, which could, in turn, result in distributed strike-slip deformation away from the fault and the deflection of abyssal-hill fabric. An initial goal of this study was to determine whether or not any of the abyssal hills were anomalously rotated so that the state of stress along the fault could be inferred. Unfortunately, the level of data resolution in the global datasets is not sufficient to determine this and areas along transforms faults that have high-resolution multibeam bathymetry data are few. In total, 91 of the measured faults were flanked by discernible abyssal hills, and only 3 of them (the faults mentioned above) had anomalously rotated fabric that was discernible in the data.

Another feature that was noted along with abyssal-hill fabric was the presence of a median ridge

or valley. Transform faults form along small circles, centered about the plate's Euler pole (Fox & Gallo, 1989). Most transform faults are defined by median valleys, indicating that the RTF is either in equilibrium with the current plate motion direction or is under some component of extension along the fault. Only 17 of the faults in this study showed some measurable component of a median ridge; including Clipperton, Mendocino (on the Gorda Ridge) and the Blanco Ridge segment of the Blanco Transform Fault (on the Juan de Fuca Ridge). Median ridges are thought primarily to form as a response to increased transpression along the transform fault during periods of compression (Pockalny, 1997; Pockalny *et al.*, 1997). Therefore, the presence and location of transverse ridges with the transform domain may indicate periods of transpression over the course of the fault's tectonic history.

The presence of fracture zone traces was also noted during this study. Fracture zones act as great age markers as the age of the crust can quickly be inferred just from a measurement of length and slip rate. The lack of fracture zones is important to note as well, because their absence could indicate a relative young and still evolving fault, as in the case of the Discovery Transform Fault on the EPR (Wolfson-Schwehr *et al.*, 2014), or a fault that is undergoing reorganization. Fracture zones are also makers for past changes in plate motion, as the ever growing seam preserves the change in the rock record. Fracture zones could not be measured for 31 of the faults in this characterization, though as in the case of the abyssal hills, the scale of a fracture zone depression is typically <5 km, and is on the edge of the resolution of this study. Thus, the inability to see a fracture-zone trace in the data does not mean it does not exist.

3.3   Global Scaling Relations

In order to assess whether or not segmentation of RTFs can explain why some faults do not follow the scaling relations of Boettcher & Jordan (2004) and Boettcher & McGuire (2009), the scaling relations were recomputed using the new segmented RTF database. Two adjacent fault segments

were combined and treated as a single-segment fault where the offset between them was less than 5 km. Thermal modeling of the effect of physical RTF segmentation on the underlying thermal structure of the fault indicates that for most moderate- to fast-slipping RTFs, two adjacent fault segments will be significantly thermally decoupled at offsets $\geq$ 5 km. This scale of offset also agrees with the resolution of the most recent global topography dataset (v. 18.1 Sandwell *et al.*, 2014). RTFs were included in the analysis if their fault length, L, and thermal area, A_T, were $\geq$50 km and 200 km^2, respectively. The thermal area, A_T, is defined as the area above the 600°C isotherm. The length requirement eliminates small faults where a large portion of the seismicity may actually be attribute to ridge-crest normal faulting. It also helps avoid associating an earthquake with the wrong RTF, as the uncertainly in earthquake locations from the CMT catalog is also on the order of 50 km for mid-ocean faults (Ekström *et al.*, 2012; Wolfson-Schwehr *et al.*, 2014). A_T is approximated using the half-space cooling model (Eq. 3.1). For each RTF segment that meets the L and A_T requirements, a bounding polygon was used to select which earthquakes to associate with the fault from a 39-year seismic record obtained from the CMT catalog (Ekström *et al.*, 2012), spanning the time period between January 1, 1976 and September 26, 2015. The bounding polygon initially extended out 100 km to the sides parallel to the fault, and 50 km perpendicular to the fault. These bounds are adjusted as necessary to avoid overlap with other bounding polygons. Earthquakes on RTFs have been observed to follow a tapered Gutenberg-Richter distribution (Kagan & Jackson, 2000; Bird *et al.*, 2002; Boettcher & Jordan, 2004):

$$N(M) = N_0 \left(\frac{M_0}{M} \right)^{\beta} \exp \left(\frac{M_0 - M}{M_C} \right), \tag{3.2}$$

where $N(M)$ is the cumulative number of events with a seismic moment greater than, or equal to, M, N_0 is the cumulative number of events above the completeness threshold moment, M_0, and β is the slope of the distribution below the exponential roll off at M_C, the largest expected earthquake on the fault. In order to ensure there were enough earthquakes to robustly compute the scaling

relations, the RTFs were divided into 4 groups on the basis of their A_T. A_T divisions were chosen such that each of the 4 groups had approximately the number of events over the threshold moment. The scaling parameters were then estimated by fitting equation 2 to the groups using using a maximum likelihood approach. Event frequencies for each group were binned by 0.1 increments of $\log(M)$, and $\bar{n}k$, the variable that represents the number of events in each group, was assumed to be Poisson-distributed with an expected value, $\bar{n}k \approx -\Delta M_k dN(M_k)/dM$, where $N(M)$ was specified by equation 3.2. The log likelihood function then computes a best fit β and M_C value for each A_T group:

$$
\begin{aligned}
\text{Lik}(\beta, M_C) = \sum_k \Bigg\{ & \ln\left[n_k N_0 \left(\frac{\beta}{M_k} + \frac{1}{M_C} \right) \left[\frac{M_k}{M_0}\right]^{-\beta} \cdot \exp\left[\frac{M_0 - M_k}{M_C}\right] \right] \\
& - N_0 \left(\frac{\beta}{M_k} + \frac{1}{M_C} \right) \left[\frac{M_k}{M_0}\right]^{-\beta} \cdot \exp\left[\frac{M_0 - M_k}{M_C}\right] - \ln(n_k!) \Bigg\}
\end{aligned} \quad (3.3)
$$

A contour plot for the likelihood functions for β and M_C for the four A_T groups is shown in Figure (3.4) The 95% confidence region for each estimate includes the maximum likelihood estimate obtained with β fixed at two-thirds. These results agree with the maximum likelihood scaling of Bird et al. (2002) and Boettcher & Jordan (2004), who showed that at $\beta = 2/3$, RTFs show self-similar scaling below the upper cutoff moment. The maximum likelihood estimates of M_C consistent with $\beta = 2/3$ can now be used to compute additional scaling parameters for RTF seismicity. The maximum likelihood values for M_C and β were then used to compute scalings for the four A_T groups for A_E, the effective seismogenic area of the fault (the area displaced by the observed moment release rate per unit tectonic slip); A_C, the area of the fault ruptured in the largest expected event; and T_R, the repeat time for the largest event on the fault.

$$A_E = \frac{M_C}{\mu \bar{V} N(M_C) T} \qquad\qquad \propto C_E A_T^\alpha = C_E L^{3/2} V^{-1/2} \qquad (3.4)$$

$$A_C = \left(\frac{M_C}{\Delta \sigma} \right)^{2/3} \qquad\qquad \propto A_T^\gamma = C_{AC} L^{3/4} V^{-1/4} \qquad (3.5)$$

$$T_R = \frac{\Delta \sigma^{2/3} C_{MC}^{1/3} A_T^{1/4}}{\mu V} \qquad\qquad \propto A_T^{1/4} V^{-1} \qquad (3.6)$$
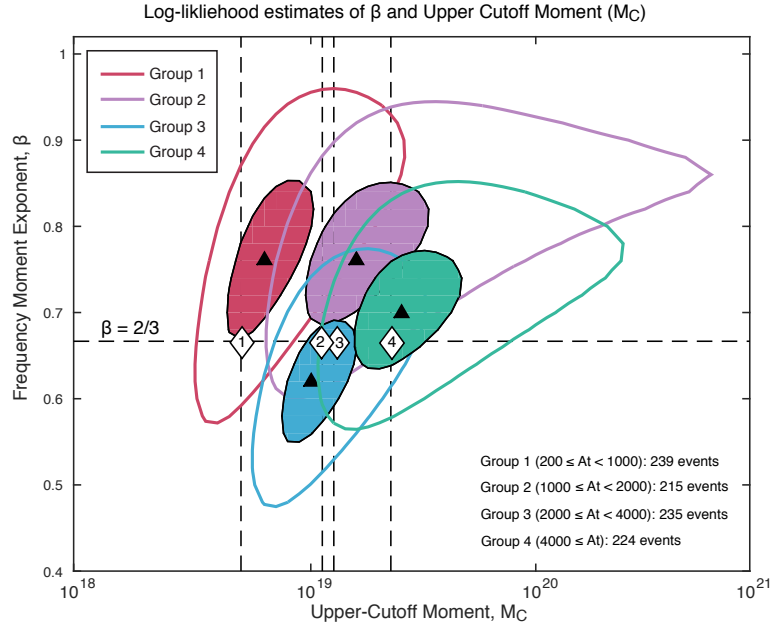
Figure 3.4: Maximum likelihood estimate of the upper cutoff moment, M_C, and the slope of the distribution, β, for each of the A_T groups. White diamonds marks the MLE estimates. Black diamonds mark where $\beta = 2/3$.

Following Boettcher & Jordan (2004), the scaling exponents, α and γ, were derived using maximum likelihood functions. Despite the fact that different best fit values were obtained for α and γ using the segmented fault database, the values were within the 95% confidence bounds of the values used in (Boettcher & Jordan, 2004). A_E is directly proportional A_T, with $\alpha = 1$. The scaling exponent for A_C, is consistent with a value of 0.5. While the scaling exponents for both

43

A_E and A_C did not change, preserving the proportionality of the original scaling relationships, the scaling constants did change (Fig. 3.5). For A_E, the constant C_E represents χ, the seismic coupling coefficient, therefore, the increase from 0.15 to $\sim$0.22 indicates that more of the motion along RTFs is being accommodated seismically when segmentation is taken into account. For A_C, the constant C_{AC} does not have a direct meaning such as in the case of C_E, but the increase from $\sim 4.6 \times 10^3$ to $\sim 5.6 \times 10^3$ indicates that the largest expected earthquakes rupture a larger portion of the available fault area. Both of these results are expected given that we effectively reduced overall fault length by taking into account RTF segmentation. A table of the individual scaling relations computed for each individual fault segment is provided in the supplement to this chapter (3-S2).

3.4 Discussion

Physical segmentation of RTFs was observed on 10 of the 12 mid-ocean ridges involved in this study, with the exceptions being the America Antarctic Ridge (AAR) and the Aden Ridge, in the Gulf of Aden between Somalia and the Arabian Peninsula. The four faults on the AAR and two faults on the Aden Ridge have slow ($\sim$2 to 5.5 mm/yr) to ultraslow ($<$2 mm/yr) slip rates. Other slow to ultraslow slipping faults do show segmentation, including many faults on the Mid-Atlantic Ridge (MAR) and Andrew Bain on the Southwest Indian Ridge (SWIR), indicating that segmentation is not constrained by slip rate alone. It is interesting to note, however, that with the exception of the Clipperton Transform Fault, all RTFs with slip rates greater than 90 mm/yr are segmented. These fast-slipping faults all occur on the EPR, which has undergone multiple small counterclockwise changes in plate-motion direction over the last few millions of years (Macdonald *et al.*, 1984, 1992; Carbotte & Macdonald, 1994). Mid-ocean ridge transform fault segmentation is thought to form as a response to transtensional stresses across the fault domain brought about by changes in plate-motion direction. It is understandable then that the highest prevalence of segmentation is found on the fastest spreading ridge that has undergone recent changes in plate motion. The one fault
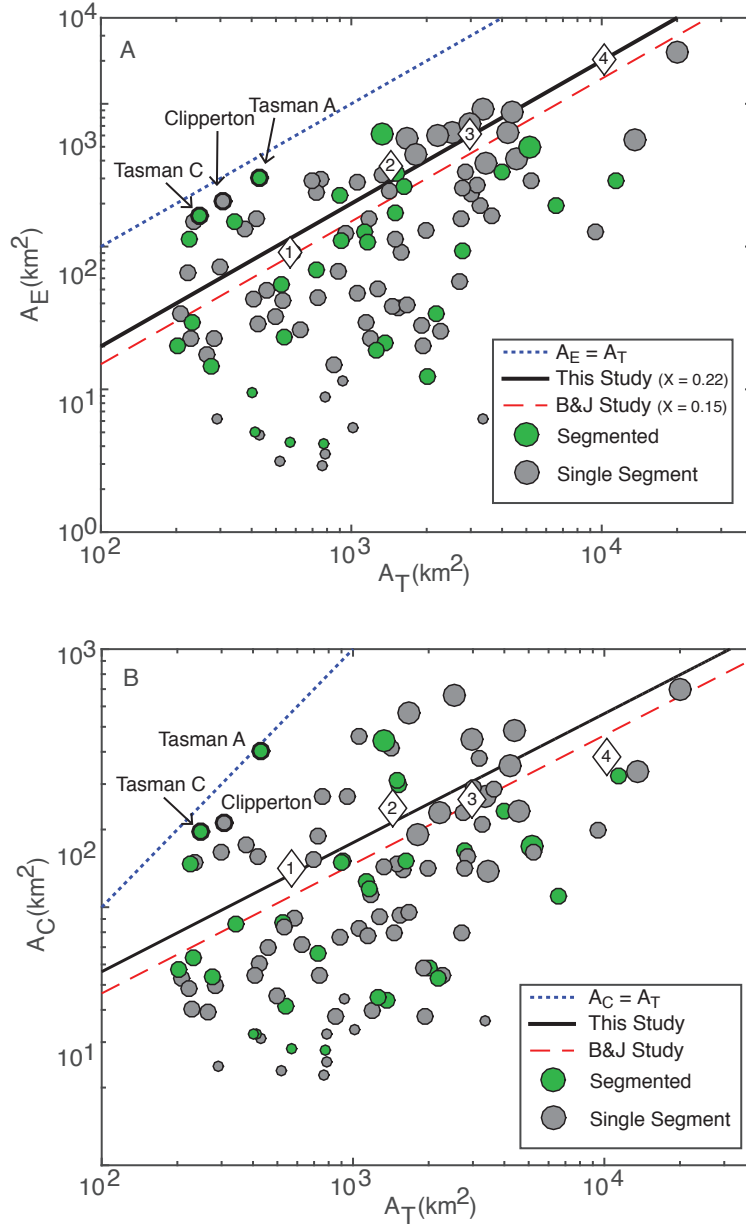
Figure 3.5: A: A_E versus A_T and B: A_C versus A_T for the RTFs used in the scaling relation computation. Circles represent individual RTFs sized by their cumulative moment magnitude. Colors denote segmentation: Gray circles represent single segment RTFs, and green represent fault segments that are part of a larger, segmented RTF system. In both plots, the thick black line indicates the scaling relationship computed in this study. The dashed red line is the scaling relation of Boettcher & Jordan (2004). The dotted blue line shows the 1:1 scaling of A_E:A_T and A_C:A_T, respectively. Faults that fall outside the expected values are highlighted in the plots.

on the EPR that is not segmented, the Clipperton Transform Fault, is a left-lateral transform fault separating the Pacific Plate from the Nazca Plate. Counterclockwise changes in relative plate motion between the Pacific and Nazca Plates, therefore, would put Clipperton under compression. Indeed, the structure of the Clipperton Transform Fault also supports the notion that the fault is under compression, including the presence of a median ridge and anomalously rotated abyssal hill fabric. These observations raise the question of what is the dominant controlling factor in the segmentation of RTFs. Does spreading rate of the ridge play a more important role than recent changes in plate-motion direction, or perhaps are the changes in plate motion the dominant factor? To answer this question, one would need to determine when each offset along segmented RTFs formed and attempt to link their formation to changes in plate-motion direction. The spreading rate histories for each of the RTFs would also need to be determined. This question could also be addressed through the mechanical modeling of RTF formation and breakup, wherein the parameters of relative plate-motion direction and spreading rate could be easily varied. Both of these methods are beyond the scope of this study.

The computation of the new scaling relations led to expected, though still somewhat surprising results. As theorized, breaking up the faults according to their segmentation increased the seismic coupling on the faults and the largest events were observed to rupture a larger portion of the full fault area. The amount of this change, however, is actually smaller than expected. It is not understood why the largest earthquakes on RTFs do not rupture the full fault area. However, one hypothesis is that the current studies did not take into account RTF segmentation, and thus were using estimated fault lengths and areas that were too large. If segmentation were the sole reason for the low seismic coupling and small maximum earthquakes, then the new scaling relations for A_C and A_E should have scaling constants and exponents near unity. In both plots in figure 3.5, one would expect the majority of the faults to line up on the 1:1 lines. The fact that the results do not show this indicates that the currently resolved physical segmentation of RTFs alone, is not

sufficient to explain these discrepancies. There is some scale of segmentation, whether physical or mechanical (e.g., varying frictional properties along the fault), that is still missing.

Some of the discrepancy between what the scaling relations show and what is expected may still be due to incorrect source parameter estimates. Currently a constant stress-drop model in employed for the computation of A_C. Boettcher & McGuire (2009) computed a range of estimated stress drops for RTFs by comparing estimated recurrence times for the largest observed earthquakes to the actual observed recurrence times. The results indicate that stress drops between 3 and 10 MPa may be common along RTFs. In this study, stress drop is assumed to be 3 MPa. For some faults, this value may be too high, in which case the computed A_C would be too low. Conversely, if the stress drop is too low, then the resulting A_C would be too high. Another possible issue is the number of faults that make up each A_T group. Seismic catalogs on RTFs can be fairly sparse, so to make sure the computation of the scaling relations was robust, the faults were grouped on the basis of their fault thermal area. The A_T divisions where chosen such that the number of earthquakes above the threshold moment in each group were as equal as possible; however, this leaves each group with a highly variable number of faults. Group 4, faults with thermal areas above 4,000 km^2, for example, is composed of 10 faults. If one of two of those faults have more or less earthquakes than expected, or if their largest earthquakes haven't occurred during the catalog period, that could significantly affect the scaling relations. Indeed, Figure 3.5B, the plot of A_C versus A_T, shows that the diamond that represents group 4 falls lower than expected and may be pulling A_C down with it.

Another goal of this study was to identify faults that behave as exceptions to the scaling relations and determine whether or not the structure of the fault may provide clues as to why. Figure 3.6 plots the fraction of the fault area ruptured in the largest earthquake (A_C/A_T) versus A_T. Faults that deviate from the scaling relations, in that they have larger than expected maximum earthquakes, are readily highlighted in this plot. An example of one such fault is the Clipperton Transform Fault,

also identified by Boettcher & McGuire (2009) as anomalous, for hosting much larger than expected earthquakes (Mw 6.6 observed versus Mw 6.0 expected) and much longer recurrence times (~20 yrs observed versus 5 yrs expected). As has previously been discussed, however, there are several lines of evidence that suggest the Clipperton Transform Fault has undergone repeated periods of transtension in the last few million years, and may still be adjusting to the most recent change in plate motion. Therefore, the Clipperton Transform Fault is likely anomalous due to the increased normal stresses that would explain the large earthquakes and extended recurrence time. Two other faults that stand out in the scaling relations are Tasman A and Tasman C, two fault strands of the segmented Tasman Transform Fault on the Southeast Indian Ridge. The largest expected earthquake on Tasman A based on its length and slip rate is an Mw 6.1. However, in 2007 an Mw 6.9 event occurred right in the middle of the fault segment. The whole Tasman Transform Fault system is composed of 5 individual fault segments and Tasman A is the only segment defined by a median ridge. It is possible that Tasman A is experiencing localized compression. Tasman C also has a higher than expected maximum-sized earthquake (Mw 6.5 versus the expected 5.9), yet this fault segment is defined by a median valley and appears to be under extension. Perhaps the scale of segmentation used in deciding where to combine adjacent fault segments is not appropriate for the Tasman Transform Fault. In the scaling analysis, adjacent fault segments were combined if the offset between them was shorter than 5 km. The offsets on the Tasman Transform Fault are all on the order of 20 km. Furthermore, Tasman C is a relatively short segment (61 km) compared the lengths of Tasman B (218 km) and Tasman D (173 km). Consequently, the seismicity on Tasman C may be influenced by the proximity of Tasman B and D, and these three segments may need to be treated as one to account for the large thermal influence of one segment on another (see Chapter 2). The middle segment of the segmented Hollister RTF system, Hollister B, has an expected maximum-sized earthquake of Mw 6.0, but an observed maximum of Mw 6.4. The offsets between Hollister B and Hollister A and C are 7 km and 11 km, respectively. This length of offset, combined with

Hollister's slip rate of ∼78 mm/yr, could indicate that the segments of the Hollister Transform Fault are still seismically connected, and should be treated as a single segment fault. The other transform fault that stands out in Figure 3.6 is the Hillegom Transform Fault. Hillegom Transform Fault, on the Southeast Indian Ridge (SEIR), is a single segment fault defined by a 2-km deep, median valley and has no apparent fracture zones. Studies on Hillegom also note the lack of fracture zones and hypothesize that the Hillegom Transform Fault is a relatively young fault that is evolving from the fracture zone of the now defunct St. Paul Transform Fault, not to be confused with the active St. Paul RTF on the MAR (Conder *et al.*, 2000; Scheirer *et al.*, 2007). The Hillegom Transform Fault has formed on top of the Amsterdam-St. Paul Plateau, a large volcanic massif that straddles the SEIR. High seismic reflectance associated with the flat bathymetry in the median valley of the Hillegom Transform Fault suggests that off-axis volcanism may be occurring within the transform fault (Scheirer *et al.*, 2007). Given the fact that Hillegom is forming within an active volcanic massif, it is not surprising that the fault does not follow the predicted scalings. As the massif itself is also continuously forming and Hillegom is still evolving and may have active volcanism within its median valley, it is possible that that fault is undergoing periods of tranpression that could explain the higher than expected maximum earthquake.
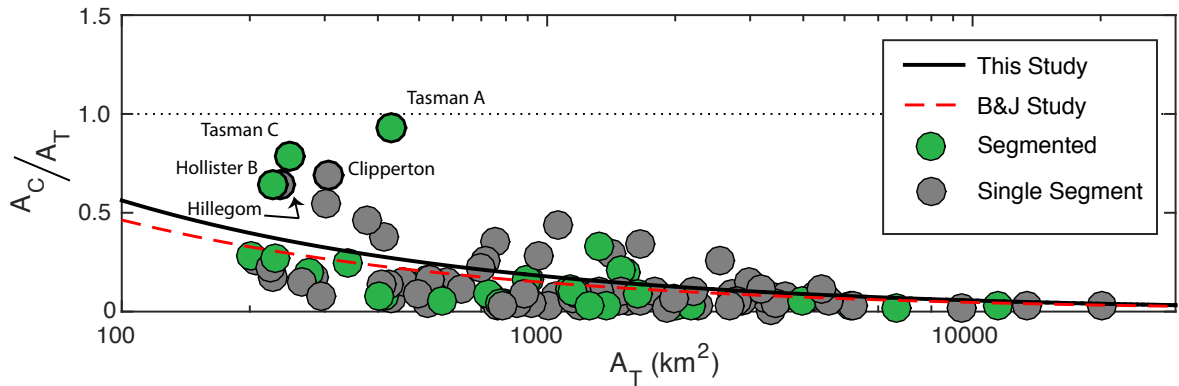
Figure 3.6: The fraction of the fault ruptured in the largest earthquake, A_C/A_T, versus A_T. Scaling from this study is shown in black, scaling from Boettcher & Jordan (2004) is shown in red. The coloring of the circles follows previous figures. Anomalous faults are highlighted by their name and thicker black border.

One the faults that stuck out as anomalous in Boettcher & Jordan (2004) was the Quebrada Transform Fault, a segmented transform fault on the EPR. Quebrada was identified to have a very low seismic coupling coefficient (0.01) and a small maximum-sized earthquake given its size (Mw 5.6 observed, Mw 6.1 expected). In the Boettcher & Jordan (2004) study, the Quebrada Transform Fault was treated as a single fault, although in this study it is broken up into three separate segments: Quebrada A, Quebrada B, and Quebrada CD. The last two segments were combined because the adjoining offset is less than 5 km. The result of breaking up Quebrada is that the observed maximum-sized earthquakes on each segment now match the expected maximum sizes. The seismic coupling has increased slightly, but is still quite low (0.06 for Quebrada A and Quebrada CD, and 0.02 for Quebrada B) because the Quebrada Transform Fault does not host any large, repeating ruptures (McGuire, 2008). The reason for the lack of repeating ruptures on the Quebrada Transform Fault is not understood, especially in light of the fact that the two adjacent transforms, Discovery and Gofar Transform Faults, both have well established repeating rupture patches (McGuire, 2008; McGuire et al., 2012; Wolfson-Schwehr et al., 2014).

3.5 Conclusion

This study presents a global characterization of oceanic transform-fault structure with an emphasis on physical segmentation. Fault segmentation was observed on 37 of the 132 oceanic transform fault systems that represents the full range of slip rates. The highest prevalence of segmentation occurs on the East Pacific Rise, which has the fastest spreading rates in the world as well as some of the most recent changes in plate-motion direction. In order for a fault to become segmented, a change in relative plate motion and a sufficiently high spreading rate to allow for lithospheric thinning are needed. In total, 202 individual fault segments where characterized on the basis of their fault structure and are summed up in Table 3-S1 in the Supplement. An earlier version of this dataset, based on a previous version of the Smith and Sandwell global topography dataset, was

incorporated into the Geophysical Earth Model (GEM) Faulted Earth database, a compilation of neotectonic faults, folds and fault sources used for seismic hazard estimation (Christophersen *et al.*, 2015).

This study also examines the effect of the physical segmentation of RTFs on global scaling relations by recomputing them using an updated seismic catalog (Jan. 1, 1976 to September 26, 2015) and a new fault database in which all adjacent faults separated by offsets greater than 5 km are broken up into their respective segments. If the primary reason for the low seismic coupling and small maximum earthquakes on RTFs is because current scaling relations do not take into account segmentation, then the relations for A_C and A_E computed in this study should have constants and exponents near unity. However, the results show only slight increases in the constants C_E and C_{AC}, and scaling exponents that are statistically unchanged. Although there are some limitations regarding how the scaling relations are computed (e.g., using a constant stress drop model and a constant cutoff criteria for offset length), it is also likely that there is some scale of segmentation, either physical, mechanical, or both, that is still missing. The newest Smith and Sandwell global topography dataset provides a maximum resolution in the oceans of ~ 5 km (Sandwell *et al.*, 2014), meaning that although segmentation above this scale may be adequately quantified, capturing anything below this is really dependent on having high-resolution multibeam sonar data.

Finally, this study also addresses whether or not fault structure can explain why some faults present clear challenges to the scalings relations. Five anomalous faults are discussed, and in each case the structure of the fault was able to provide clues as to why the seismicity was behaving in an unexpected way. The clearest example of this is the Clipperton Transform Fault, which has higher than expected maximum magnitudes, as well as longer than expected recurrence times. The orientation of the Clipperton Transform Fault, combined with the presence of a median ridge and anomalously rotated abyssal hill fabric, clearly indicates that the fault is under compression. The transpressional forces across the fault would increase the normal stresses, which may be related to

both the larger than expected earthquake size and the recurrence interval.

While both the seismic coupling and the fraction of the fault ruptured in the largest event increased slightly for RTFs included in this study, the results were not significantly different from the scaling relations of Boettcher & Jordan (2004) and Boettcher & McGuire (2009). Thus, the current scaling relations still hold, even when taking into account our current resolvable physical segmentation of RTFs. It remains possible, however, that as global bathymetric compilations improve in resolution, or as more multibeam bathymetric data is collected over RTF systems, that we will discover that faults may be segmented on smaller and smaller scales. A combination of this physical segmentation, along with varying mechanical properties along RTFs, remains the most likely reason for the seismic deficit and small earthquakes observed on these faults.

3.6 Supplement

3.6.1 Section A: Oceanic Transform Fault Characterization Table

Table 3-S1: Characterization of Oceanic Transform Faults. West and East RTI measurements are the length from the ridge-transform intersection to the nearest ridge discontinuity

Fault	Name	Long.	Lat.	Length	Slip Rate	Seg	Ridge /Valley	West RTI	East RTI	Fracture Zones	Abyssal Hills	Transverse Ridges
#				(km)	(mm/yr)		(%)					
					Mid-Atlantic Ridge							
1	Ascension A	-13.2457	-7.3740	58	29.54	x	0/100	85	23	x	x	-
2	Ascension B	-12.1360	-6.8837	203	29.51	x	0/100	23	93	x	x	-
3	Atlantis	-42.3457	30.0617	63	22.40	-	0/100	90	143	x	x	-
4	Bode Verde A	-14.5907	-12.2460	56	30.02	x	0/100	101	39	x	-	-
5	Bode Verde B	-13.7002	-11.6760	162	29.98	x	0/100	39	154	x	-	-
6	Chain	-14.5227	-1.2368	313	28.58	-	0/100	210	125		-	-
7	Charlie Gibbs A	-33.2599	52.6168	203	21.73	x	0/100	51	39	x	-	x
8	Charlie Gibbs B	-30.8240	52.1236	110	21.83	x	0/100	39	107	x	-	x
9	Doldrums A	-40.0168	8.8229	109	25.56	-	0/100	60	68	x	-	-
10	Doldrums B	-38.7814	8.2131	162	25.74	-	0/100	68	55	x	-	-
11	Doldrums C	-37.3781	7.7201	149	25.89	x	0/100	55	36	x	-	x
12	Doldrums D	-35.6648	7.4013	230	26.00	x	0/100	36	23	x	-	x
13	Doldrums E	-34.2776	7.1946	77	26.08	x	0/100	23	32	x	-	x
14	Falkland	-12.2514	-47.3090	181	27.44	-	0/100	95	37	x	-	x
15	Gough	-16.2298	-39.7910	57	28.98	-	0/100	50	45	x	-	-
16	Hayes	-38.6474	33.6635	80	21.65	-	0/100	62	21	x	x	-
17	Jan Mayen A	-9.6377	71.3747	127	15.45	x	0/100	43	11	x	-	-
18	Jan Mayen B	-7.3876	71.1387	27	15.45	x	0/100	11	35	x	-	x
19	Kane	-45.6185	23.7372	146	23.43	-	0/100	91	1108	x	x	x
20	MAR 15°20'	-45.7371	15.2761	193	23.57	-	0/100	345	175	x	x	-
21	MAR 18S	-13.3749	-17.7200	91	30.34	-	0/100	171	109	x	-	-
22	MAR 21S	-11.7190	-21.2300	45	30.40	-	0/100	81	108	x	-	-
23	MAR 22S A	-13.2588	-22.8150	85	30.39	x	0/100	116	41	x	-	x
24	MAR 22S B	-12.3655	-22.2760	86	30.40	x	0/100	41	14	x	-	x
25	MAR 22S C	-11.8257	-22.0190	22	30.40	x	0/100	14	81	x	-	x
26	MAR 25°50'S	-13.7426	-25.6580	39	30.32	-	0/100	76	34	x	x	-
27	MAR 25S	-13.5519	-24.8980	37	30.35	-	0/100	91	76	x	-	-
28	MAR 29°45'S	-13.7661	-29.7600	27	30.10	-	0/100	97	57	x	-	-
29	MAR 29S A	-13.4456	-29.1910	74	30.13	x	0/100	57	22	x	x	-
30	MAR 29S B	-12.7702	-28.8650	59	30.15	x	0/100	22	72	x	x	-
31	MAR 32S A	-14.4245	-32.4970	23	29.87	x	0/100	107	18	x	x	-
32	MAR 32S B	-13.9450	-32.2680	57	29.89	x	0/100	18	8	x	x	-
33	MAR 32S C	-13.4782	-32.1120	29	29.90	x	0/100	8	80	x	x	-
34	MAR 34S	-14.8348	-34.1600	69	29.71	-	0/100	31	53	x	x	-

Table 3-S1: Characterization of Oceanic Transform Faults. West and East RTI measurements are the length from the ridge-transform intersection to the nearest ridge discontinuity

Fault	Name	Long.	Lat.	Length	Slip Rate	Seg	Ridge /Valley	West RTI	East RTI	Fracture Zones	Abyssal Hills	Transverse Ridges
#				(km)	(mm/yr)		(%)					
35	MAR 35S	-16.5118	-35.3960	250	29.60	-	0/100	121	41	x	-	x
36	MAR 40S	-16.6391	-40.3500	40	28.90	-	0/100	128	50	x	-	-
37	MAR 5S	-11.9376	-5.0357	78	29.27	-	0/100	60	92	x	-	-
38	MAR 50S	-9.1361	-49.1260	110	26.90	-	0/100	87	79	x	-	x
39	Marathon	-44.4648	12.6387	88	24.41	-	0/100	87	40	x	x	-
40	Oceanographer	-35.6433	35.1829	121	21.27	-	0/100	92	68	x	x	-
41	Rio Grande	-12.9412	-28.2300	57	30.19	-	0/100	195	72	x	-	-
42	Romanche	-20.6093	-0.6719	878	28.27	-	0/100	208	210	x	-	x
43	Saint Paul A	-29.0194	0.9335	297	27.71	x	0/100	202	27	x	-	-
44	Saint Paul B	-27.0355	0.8731	146	27.77	x	0/100	27	24	x	-	-
45	Saint Paul C	-25.9187	0.7399	97	27.83	x	0/100	24	21	x	-	-
46	Saint Paul D	-25.2346	0.6166	50	27.88	x	0/100	21	208	x	-	-
47	Strakhov	-32.0787	3.9423	108	26.96	-	0/100	281	156	x	x	-
48	Tetyaev	-13.7495	-16.2530	123	30.28	-	0/100	171	233	x	-	-
49	Vema	-42.2863	10.7777	307	24.98	-	0/100	133	65	x	x	x
					Juan de Fuca Ridge							
50	Blanco A	-129.9160	44.3327	94	51.06	x	0/100	133	8	x	x	x
51	Blanco B	-129.2260	44.0457	24	51.01	x	0/100	8	6	x	-	x
52	Blanco C	-128.8380	43.8909	41	50.99	x	0/100	6	15	x	-	-
53	Blanco D	-127.8140	43.4512	135	50.94	x	100/0	15	6	x	x	-
54	Blanco E	-126.8260	43.0771	41	50.93	x	0/100	6	69	-	x	-
55	Sovanco	-129.7650	48.9762	135	53.90	-	30/70	80	51	-	n	x
					Gorda Ridge							
56	Mendocino	-126.0390	40.3735	237	49.48	-	100/0	131	N/A	x	-	-
					East Pacific Rise							
57	Clipperton	-103.9470	10.2194	84	106.28	-	100/0	126	175	x	anomalous	x
58	Discovery A	-104.3500	-4.0067	36	123.55	x	0/100	70	8	-	x	-
59	Discovery B	-104.0080	-3.9980	27	123.48	x	0/100	8	34	-	x	-
60	Garrett A	-112.1540	-13.4110	39	133.99	x	0/100	289	7	x	x	-
61	Garrett B	-111.8210	-13.4230	27	133.94	x	0/100	7	5	x	-	-
62	Garrett C	-111.5250	-13.4490	32	133.90	x	0/100	5	5	x	x	-
63	Garrett D	-111.2420	-13.4760	27	133.86	x	0/100	5	20	x	x	-
64	GoC 24N	-108.7720	24.0449	133	50.37	x	40/60	31	30	-	-	-
65	GoC 25N	-109.5170	24.9837	119	49.85	x	50/50	30	37	-	-	-
66	Gofar A	-105.8480	-4.5939	95	124.55	x	0/100	120	15	x	x	-
67	Gofar B	-105.2640	-4.5792	29	124.40	x	0/100	15	11	x	x	-
68	Gofar C	-104.8820	-4.5561	46	124.30	x	0/100	11	70	x	x	-
69	Orozco A	-105.1140	15.4136	46	87.81	-	0/100	106	46	-	x	-
70	Orozco B	-104.5810	15.1572	23	88.85	-	0/100	46	144	-	x	-
71	Quebrada A	-103.6830	-3.7446	27	123.12	x	0/100	34	7	x	x	-
72	Quebrada B	-103.4440	-3.7324	23	123.05	x	0/100	7	9	x	x	-

Table 3-S1: Characterization of Oceanic Transform Faults. West and East RTI measurements are the length from the ridge-transform intersection to the nearest ridge discontinuity

Fault	Name	Long.	Lat.	Length	Slip Rate	Seg	Ridge /Valley	West RTI	East RTI	Fracture Zones	Abyssal Hills	Transverse Ridges
#				(km)	(mm/yr)		(%)					
73	Quebrada C	-103.1890	-3.7005	27	122.97	x	0/100	9	4	x	x	-
74	Quebrada D	-102.8600	-3.7301	42	122.94	x	0/100	4	115	x	x	-
75	Rivera A	-108.6780	19.5692	177	73.00	x	0/100	50	16	-	-	x
76	Rivera B	-107.1760	18.6913	208	73.00	x	0/100	16	30	-	x	x
77	Siqueiros A	-104.0450	8.3991	24	112.24	x	0/100	72	15	x	x	x
78	Siqueiros B	-103.6590	8.3817	34	112.48	x	0/100	15	8	x	x	x
79	Siqueiros C	-103.4150	8.3570	18	112.68	x	75/25	8	7	-	x	x
80	Siqueiros D	-103.2080	8.3641	17	112.89	x	100/0	7	8	-	x	x
81	Siqueiros E	-102.9950	8.3781	17	112.96	x	0/100	8	131	-	x	x
82	Tomayo	-108.3350	23.0780	66	50.95	x	0/100	37	115	x	x	-
83	Wilkes A	-109.2070	-9.0185	35	129.79	x	0/100	10	91	x	x	-
84	Wilkes B	-108.6880	-9.0621	75	129.74	x	0/100	10	66	x	x	-
85	Yaquina A	-107.3140	-6.2481	23	126.66	x	0/100	155	17	x	x	-
86	Yaquina B	-106.9880	-6.1794	21	126.51	x	0/100	17	89	-	x	-
Chile Ridge												
87	Challenger A	-96.6218	-36.9970	79	46.56	x	0/100	80	13	x	x	-
88	Challenger B	-95.7192	-37.1050	67	46.58	x	0/100	13	16	x	x	-
89	Challenger C	-95.1854	-37.2450	21	46.61	x	0/100	16	10	x	x	-
90	Challenger D	-94.5775	-37.3200	82	46.62	x	0/100	10	89	x	x	-
91	Chile 38S A	-93.6255	-38.3330	43	46.85	x	0/100	34	8	x	x	x
92	Chile 38S B	-92.9816	-38.4110	68	46.86	x	0/100	8	62	x	x	-
93	Chile 39S	-92.0683	-38.9640	84	46.98	-	0/100	62	140	x	x	-
94	Chile A	-106.5110	-35.1400	493	46.42	x	0/100	N/A	20	-	-	-
95	Chile B	-102.7910	-35.8980	186	46.43	x	0/100	20	18	x	-	-
96	Chile C	-99.4232	-36.2060	420	46.46	x	0/100	18	80	x	-	-
97	Chiloe	-83.0813	-43.0260	61	47.82	-	0/100	113	27	x	-	-
98	Darwin	-76.3638	-45.8950	53	48.30	x	0/100	42	47	x	-	-
99	Guafo	-80.1486	-44.6950	286	48.10	-	0/100	33	161	x	-	-
100	Guamblin	-77.3700	-45.7050	80	48.27	x	0/100	161	42	x	x	-
101	Valdavia A	-91.5641	-41.0890	50	47.42	x	0/100	92	14	x	-	-
102	Valdavia B	-90.8074	-41.1970	77	47.45	x	0/100	14	17	x	-	-
103	Valdavia C	-89.7437	-41.3040	97	47.47	x	0/100	17	13	x	-	-
104	Valdavia D	-88.4437	-41.3470	119	47.48	x	0/100	13	21	x	-	-
104	Valdavia E	-86.7164	-41.4080	166	47.51	x	0/100	21	25	x	-	-
105	Valdavia F	-85.1445	-41.4850	69	47.54	x	0/100	25	16	x	-	-
106	Valdavia G	-84.5249	-41.5710	23	47.56	x	0/100	16	31	x	-	-
Pacific-Antarctic Ridge												
107	Heezen	-124.5340	-55.4160	382	79.02	-	30/70	64	164	x	x	x
108	Herron	-139.0720	-56.2880	26	75.45	-	100/0	111	29	-	x	-
109	Hollister A	-136.9010	-54.2150	23	77.89	x	0/100	45	7	x	x	-
110	Hollister B	-136.2280	-54.3520	62	77.93	x	0/100	7	11		x	-

Table 3-S1: Characterization of Oceanic Transform Faults. West and East RTI measurements are the length from the ridge-transform intersection to the nearest ridge discontinuity

Fault	Name	Long.	Lat.	Length	Slip Rate	Seg	Ridge /Valley	West RTI	East RTI	Fracture Zones	Abyssal Hills	Transverse Ridges
#				(km)	(mm/yr)		(%)					
111	Hollister C	-135.3930	-54.5330	34	77.95	x	0/100	11	41	x	x	-
112	L'Astronome	-150.8520	-59.6450	56	68.94	-	0/100	94	178	-	x	-
113	Le Geographe	-147.4940	-57.6250	70	71.90	-	0/100	178	269	-	x	-
114	Menard	-115.2410	-49.5630	208	85.47	-	0/100	186	159	x	anomalous	-
115	PAR 161	161.5047	-61.7780	77	45.98	-	0/100	299	54	x	-	-
116	PAR 163	163.3584	-62.0950	85	46.71	-	0/100	54	66	x	-	-
117	PAR 165	165.4610	-62.3830	89	47.58	-	0/100	66	78	x	-	-
118	Pitman	-170.7790	-64.5320	71	56.74	-	0/100	70	181	x	anomalous	x
119	Raitt A	-120.0960	-54.3330	88	80.94	x	0/100	45	9	x	x	-
120	Raitt B	-118.9350	-54.4870	58	80.99	x	0/100	9	170	x	x	-
121	Saint Exupery	-155.4170	-62.2430	42	64.73	-	0/100	65	142	-	-	-
122	Tharp	-131.1220	-54.5940	462	78.82	-	0/100	59	64	x	x	-
123	Udintsev	-142.4330	-56.4110	325	74.49	-	0/100	269	111	x	x	x
124	Vacquier	-118.0900	-53.0360	52	82.29	-	0/100	170	235	x	-	-
					American Antarctic Ridge							
125	Bullard A	-17.1357	-59.1290	94	12.99	-	0/100	35	140	x	-	x
126	Bullard B	-11.4860	-58.1840	526	13.43	-	20/80	140	46	x	-	-
127	Conrad	-3.1638	-55.7100	198	14.51	-	0/100	56	33	x	-	x
128	South Sandwich	-22.8786	-60.8490	383	12.26	-	0/100	N/A	52	x	-	x
					Southwest Indian Ridge							
129	Andrew Bain A	32.2321	-47.4900	86	13.35	x	0/100	24	83	x	x	x
130	Andrew Bain B	31.3117	-48.5570	147	13.34	x	0/100	13	24	x	x	x
131	Andrew Bain C	29.0100	-50.9500	471	13.33	x	0/100	60	13	x	x	x
132	Atlantis II	57.0414	-32.7570	200	12.02	-	0/100	49	129	x	-	x
133	Bouvet	1.9220	-54.2640	200	12.72	-	0/100	37	124	x	-	-
134	Discovery II A	41.6629	-43.2960	124	12.91	x	0/100	84	45	x	-	x
135	Discovery II B	42.5947	-41.8590	216	12.89	x	0/100	45	138	x	-	x
136	Du Toit	25.4810	-53.0070	129	13.29	-	0/100	60	65	x	x	-
137	Eric Simpson	39.2474	-43.7340	89	13.03	-	0/100	66	80	x	-	x
138	Gallieni	52.3209	-36.6360	113	12.34	-	0/100	36	92	x	-	x
139	Gauss	54.1243	-34.9980	58	12.23	-	0/100	59	54	x	-	x
140	Gazelle	53.4257	-35.8020	81	12.27	-	0/100	92	59	x	-	x
141	Indomed	46.1057	-39.4740	141	12.73	-	0/100	69	130	x	-	x
142	Islas Orcadas	6.0992	-54.1820	99	12.85	-	0/100	50	104	x	-	x
143	Marion	33.6623	-46.4680	108	13.22	-	0/100	83	81	x	x	x
144	Melville	60.7767	-29.8410	92	11.74	-	0/100	145	162	x	-	x
145	Novara	58.4108	-31.4250	45	11.93	-	0/100	129	118	x	-	x
146	Prince Edward	35.1282	-45.4450	145	13.19	-	0/100	81	217	x	-	x
147	Shaka	9.0237	-53.5520	198	12.92	-	0/100	104	35	x	-	x
					Southeast Indian Ridge							
148	Amsterdam	78.6870	-36.7010	107	62.02	-	0/100	23	120	x	x	x

Table 3-S1: Characterization of Oceanic Transform Faults. West and East RTI measurements are the length from the ridge-transform intersection to the nearest ridge discontinuity

Fault	Name	Long.	Lat.	Length	Slip Rate	Seg	Ridge /Valley	West RTI	East RTI	Fracture Zones	Abyssal Hills	Transverse Ridges
#				(km)	(mm/yr)		(%)					
149	Balleny	154.8090	-61.4290	349	64.50	-	60/40	154	300	x	-	-
150	Birubi	127.2618	-49.5040	148	69.62	-	50/50	90	45	x	x	-
151	Boomerang	78.2141	-37.3600	35	62.15	-	0/100	27	23	-	x	x
152	Euroka	126.0992	-49.2290	133	69.76	-	0/100	53	90	x	x	-
153	Geelvinck	84.7103	-41.9640	302	65.60	-	0/100	299	68	x	-	x
154	George V A	139.7171	-51.3510	234	67.49	-	0/100	314	93	x	-	x
155	George V B	140.5523	-53.2360	178	67.30	-	0/100	93	235	x	-	-
156	Heemskerck A	115.5802	-50.0050	19	70.34	x	0/100	88	16	x	x	-
157	Heemskerck B	115.9341	-49.8760	24	70.34	x	0/100	16	8	x	x	x
158	Heemskerck C	116.1865	-49.6490	26	70.34	x	0/100	8	9	x	x	x
159	Heemskerck D	116.4698	-49.3960	30	70.33	x	0/100	9	73	x	x	-
160	Hillegom's Hole	78.3063	-38.6620	59	62.70	-	0/100	58	83	-	-	-
161	SEIR 100E	99.8058	-47.6820	128	69.46	-	0/100	308	197	x	x	x
162	SEIR 106E A	106.2620	-49.0850	55	70.11	x	0/100	82	13	x	x	-
163	SEIR 106E B	106.7910	-48.6350	59	70.12	x	0/100	13	124	-	x	-
164	SEIR 120	120.4165	-49.4880	153	70.19	-	0/100	102	73	x	-	-
165	SEIR 121	121.5314	-49.3550	79	70.13	-	0/100	73	93	x	-	-
166	SEIR 122	122.7257	-49.7080	50	70.04	-	0/100	93	32	-	-	-
167	SEIR 88E	88.4153	-41.9210	65	66.47	-	0/100	155	325	-	-	-
168	SEIR 96E A	96.0316	-45.6630	88	68.69	-	100/0	44	54	-	-	x
169	SEIR 96E B	96.1364	-46.4290	40	68.82	-	0/100	54	308	-	-	-
170	St. Vincent	144.1216	-54.4960	57	66.50	-	0/100	235	136	x	-	-
171	Tasman A	146.3334	-55.2310	90	66.05	x	100/0	136	21	x	-	-
172	Tasman B	147.2791	-56.5920	218	65.82	x	0/100	21	37	x	-	-
173	Tasman C	148.4670	-57.7980	61	65.51	x	0/100	37	23	x	-	-
174	Tasman D	149.2502	-58.8660	173	65.29	x	0/100	23	44	x	-	-
175	Tasman E	150.5694	-59.8880	81	65.29	x	0/100	44	154	x	-	-
176	Ter Tholen	77.7178	-33.4440	89	60.26	-	0/100	227	200	x	x	x
177	Vlamingh	80.3625	-41.4710	123	64.35	-	60/40	156	299	x	x	x
178	Warringa A	123.3799	-49.4060	38	70.00	x	0/100	32	21	x	-	-
179	Warringa B	123.8693	-49.0720	48	69.97	x	0/100	21	99	x	-	-
180	Zeehaen	114.1238	-50.1210	70	70.35	-	0/100	82	88	x	x	x
181	Zeewolf A	78.4580	-35.4430	31	61.41	x	0/100	120	8	x	x	x
182	Zeewolf B	78.6366	-35.1800	28	61.36	x	0/100	8	200	x	x	x
						Aden Ridge						
183	Alula Fartak	51.7064	13.9416	203	18.90	-	0/100	58	29	x	-	x
184	Owen	57.5424	11.4232	335	22.84	-	0/100	65	60	x	-	x
						South Scotia Ridge						
185	Shackleton	-59.1128	-59.7490	332	6.83	-	100/0	-	-	-	-	-
						Central Indian Ridge						
186	Argo	66.3508	-13.5850	101	33.33	-	0/100	32	44	x	-	-

Table 3-S1: Characterization of Oceanic Transform Faults. West and East RTI measurements are the length from the ridge-transform intersection to the nearest ridge discontinuity

Fault	Name	Long.	Lat.	Length	Slip Rate	Seg	Ridge /Valley	West RTI	East RTI	Fracture Zones	Abyssal Hills	Transverse Ridges
#				(km)	(mm/yr)		(%)					
187	CIR 10S	66.5586	-10.0860	75	30.95	x	0/100	70	34	x	-	-
188	CIR 12°12'	65.9933	-11.8540	106	31.90	-	0/100	65	30	x	-	-
189	CIR 16S	66.9738	-16.2920	110	35.58	-	0/100	60	55	x	-	-
190	CIR 1S	67.5232	-1.1860	49	29.87	-	0/100	34	90	x	-	-
191	CIR 5S	68.5886	-4.7309	49	31.00	-	0/100	73	30	x	-	-
192	CIR 6S	68.2378	-6.8331	89	31.35	x	0/100	79	49	x	-	x
193	CIR 7S	68.0794	-7.6133	61	30.17	x	0/100	49	63	x	-	x
194	Egeria	66.5795	-20.1340	45	38.13	-	0/100	150	50	x	x	-
195	Flinders	67.2598	-20.2440	65	38.48	-	0/100	50	42	x	-	-
196	Gemino	69.2856	-22.7800	37	40.99	-	100/0	28	58	x	-	-
197	Mabahiss	68.1212	-3.0415	42	30.48	-	0/100	37	89	x	-	-
198	Marie Celeste	66.0021	-17.5090	219	35.99	-	0/100	30	60	x	x	x
199	Sealark	68.4741	-3.8789	62	30.78	-	0/100	89	73	x	-	-
200	Vema II	67.4427	-8.9231	237	30.63	x	0/100	34	63	x	x	x
201	Vityaz	68.3684	-5.6876	105	31.14	-	0/100	21	79	x	-	x

3.6.2 Section B: Ridge-Transform Fault Scaling Relations

Table 3-S2: Global Compilation of Oceanic Transform Faults.

Fault	Name	Lat.	Long.	Length	Slip Rate	ms	mb	Mw	ΣM $*10^{18}$	χ	W_T	D600	A_T	A_E	A_C	Seg
#				(km)	(mm/yr)				(Nm)		(km)	(km)	(km^2)	(km^2)	(km^2)	
1	Alula Fartak	13.94	51.71	203	18.9	5.9	6.6	6.6	18.0	0.20	13.4	16	2724	548	232	0
2	Amsterdam	-36.70	78.69	108	62.02	5.7	6.1	6.2	12.0	0.19	5.4	6.5	584	112	91	0
3	Andrew Bain A	-47.49	32.23	87	13.35	5.8	6.2	6.4	12.0	0.57	10.5	12.5	909	522	150	1
4	Andrew Bain B	-48.55	31.30	148	13.34	5.7	5.8	6	1.7	0.04	13.7	16.3	2018	72	58	1
5	Andrew Bain C	-51.00	29.07	471	13.33	6.2	6.7	6.8	32.0	0.12	24.3	29	11464	1384	323	1
6	Argo	-13.59	66.35	102	33.33	5.5	6	6	6.2	0.15	7.2	8.6	731	106	54	0
7	Ascension A	-7.37	-13.25	58	29.54	5.1	5.1	5.4	0.3	0.02	5.8	6.9	333	6	14	1
8	Ascension B	-6.88	-12.14	203	29.51	5.5	6	6	5.8	0.05	10.7	12.8	2180	111	53	1
9	Atlantis	30.06	-42.35	63	22.4	5.5	5.7	5.7	1.1	0.07	6.9	8.2	432	29	31	0
10	Atlantis II	-32.76	57.04	201	12.02	5.4	5.8	5.8	1.2	0.02	16.7	20	3365	58	36	0
11	Balleny	-61.43	154.81	350	64.5	5.8	6.7	6.7	110.0	0.28	9.6	11.4	3340	936	270	0
12	Birubi	-49.50	127.26	148	69.62	5.3	4.7	5.4	0.5	0.00	6	7.1	884	4	14	0
13	Blanco A	44.33	-129.92	94	51.06	5.8	6	6.2	8.1	0.17	5.5	6.6	523	91	88	1
14	Blanco B	44.05	-129.23	24	51.01	5.4	6	6.2	3.3	0.55	2.8	3.4	67	37	91	1
15	Blanco C	43.89	-128.84	41	50.99	5.2	5.2	5.4	0.2	0.02	3.7	4.4	150	3	15	1
16	Blanco D	43.45	-127.81	135	50.94	6.1	6.3	6.4	28.0	0.35	6.7	8	900	311	149	1
17	Blanco E	43.08	-126.83	41	50.93	5.2	5.2	5.5	0.6	0.05	3.7	4.4	151	7	19	1
18	Bode Verde A	-12.25	-14.59	56	30.02	4.9	4.6	5.1	0.1	0.01	5.6	6.7	313	2	8	0
19	Bode Verde B	-11.68	-13.70	162	29.98	5.4	6.1	6.2	5.4	0.07	9.5	11.4	1542	102	93	0
20	Boomerang	-37.36	78.21	35	62.15	5.3	5.8	5.8	2.0	0.17	3.1	3.7	108	19	33	0
21	Bouvet	-54.26	1.92	201	12.72	5.6	6.5	6.6	22.0	0.30	16.3	19.4	3271	982	210	0
22	Bullard A	-59.13	-17.14	95	12.99	6.1	6.2	6.2	5.7	0.24	11.1	13.2	1051	249	82	0
23	Bullard B	-58.18	-11.49	526	13.43	6.7	6.7	6.8	63.0	0.20	25.6	30.6	13479	2664	334	0
24	Chain	-1.24	-14.52	313	28.58	6.4	7	6.8	71.0	0.33	13.6	16.2	4242	1410	354	0
25	Challenger A	-37.00	-96.62	78	46.56	5.2	5.4	5.8	1.3	0.04	5.3	6.3	414	15	32	1
26	Challenger B	-37.11	-95.72	67	46.58	0	0	0	0.0	0.00	4.9	5.9	329	0	0	1
27	Challenger C	-37.25	-95.19	20	46.61	0	0	0	0.0	0.00	2.7	3.2	53	0	0	1
28	Challenger D	-37.32	-94.58	82	46.62	4.9	5	5.4	0.5	0.01	5.4	6.5	446	6	14	1
29	Charlie Gibbs A	52.62	-33.26	203	21.73	6.1	7.1	7.1	69.0	0.71	12.5	14.9	2541	1799	665	0
30	Charlie Gibbs B	52.12	-30.82	110	21.83	5.6	5.4	5.8	1.2	0.03	9.2	11	1011	31	33	0
31	Chile 38S A	-38.33	-93.63	43	46.85	5.2	5	5.3	0.3	0.02	3.9	4.7	169	4	12	1
32	Chile 38S B	-38.41	-92.98	68	46.86	0	0	0	0.0	0.00	4.9	5.9	336	0	0	1
33	Chile 39S	-38.96	-92.07	84	46.98	5.5	6	6.1	6.2	0.16	5.5	6.5	460	75	70	0
34	Chile A	-35.14	-106.51	493	46.42	5.7	6.1	6.3	28.0	0.05	13.3	15.9	6580	345	110	1
35	Chile B	-35.90	-102.79	186	46.46	6.1	6.5	6.7	39.0	0.31	8.2	9.8	1525	479	296	1
36	Chile C	-36.21	-99.42	420	46.43	5.7	6.3	6.5	59.0	0.14	12.3	14.7	5174	731	173	1
37	Chiloe	-43.03	-83.08	61	47.82	5.2	5.4	5.5	1.6	0.07	4.6	5.5	282	19	20	0
38	CIR 10S	-10.09	66.56	76	30.95	4.8	5	5	0.1	0.00	6.4	7.7	488	2	5	0
39	CIR 12 12	-11.85	65.99	106	31.9	5.8	5.6	5.8	2.1	0.05	7.4	8.9	791	38	32	0

Table 3-S2: Global Compilation of Oceanic Transform Faults.

Fault	Name	Lat.	Long.	Length	Slip Rate	ms	mb	Mw	ΣM $*10^{18}$	χ	W_T	D600	A_T	A_E	A_C	Seg
#				(km)	(mm/yr)				(Nm)		(km)	(km)	(km^2)	(km^2)	(km^2)	
40	CIR 16S	-16.29	66.97	110	35.58	5.2	5.5	5.6	1.6	0.03	7.2	8.6	792	26	20	0
41	CIR 1S	-1.19	67.52	50	29.87	0	0	0	0.0	0.00	5.3	6.3	265	0	0	0
42	CIR 5S	-4.73	68.59	49	31	4.9	5.3	5.3	0.4	0.03	5.1	6.1	252	8	12	0
43	CIR 6S	-6.83	68.24	89	31.35	4.9	0	5.1	0.1	0.00	6.9	8.2	614	1	7	0
44	CIR 7S	-7.61	68.08	62	30.17	5.3	5.4	5.4	0.5	0.02	5.9	7	364	9	15	0
45	Clipperton	10.22	-103.95	84	106.28	5.8	6.5	6.6	24.0	0.41	3.6	4.4	307	127	213	0
46	Conrad	-55.71	-3.16	198	14.51	5.7	6.6	6.7	25.0	0.33	15.1	18.1	2995	989	290	0
47	Darwin	-45.90	-76.36	53	48.3	5.5	5.9	5.9	3.4	0.18	4.3	5.1	227	41	40	0
48	Discovery A	-4.01	-104.35	36	123.55	5.1	5.9	6	6.6	0.38	2.2	2.7	80	30	56	1
49	Discovery B	-4.00	-104.01	27	123.48	5.3	5.6	5.8	2.9	0.26	1.9	2.3	52	13	32	1
50	Discovery II A	-43.30	41.66	124	12.91	5.4	6.1	6.4	10.0	0.29	12.6	15.1	1573	460	139	0
51	Discovery II B	-41.86	42.59	216	12.89	5.7	6.3	6.7	19.0	0.23	16.7	20	3620	819	288	0
52	Doldrums A	8.82	-40.02	109	25.56	5.9	5.8	5.9	1.6	0.04	8.5	10.1	922	35	44	0
53	Doldrums B	8.21	-38.78	162	25.74	6.5	7.1	7	63.0	0.84	10.3	12.3	1664	1390	565	0
54	Doldrums C	7.72	-37.38	149	25.89	5.9	6	6.2	4.9	0.07	9.8	11.7	1464	107	79	0
55	Doldrums D	7.40	-35.66	229	26	6	6.5	6.5	11.0	0.09	12.1	14.5	2783	252	166	1
56	Doldrums E	7.19	-34.28	77	26.08	5.5	5.8	5.9	3.6	0.14	7	8.4	542	78	41	1
57	Du Toit	-53.01	25.48	130	13.29	5.4	5.9	6.2	5.3	0.14	12.8	15.3	1664	228	95	0
58	Egeria	-20.13	66.58	46	38.13	5.8	5.6	5.5	1.2	0.09	4.5	5.4	207	18	17	0
59	Eric Simpson	-43.73	39.25	89	13.03	5.6	6.6	6.7	14.0	0.64	10.7	12.8	952	614	270	0
60	Euroka	-49.23	126.10	134	69.76	5.3	5.6	5.6	2.0	0.02	5.7	6.8	761	16	22	0
61	Falkland	-47.31	-12.25	181	27.44	5.4	5.7	6	3.9	0.04	10.5	12.6	1904	80	58	0
62	Flinders	-20.24	67.26	65	38.48	5.8	5.6	5.2	0.6	0.03	5.3	6.4	346	9	9	0
63	Gallieni	-36.64	52.32	114	12.34	5.7	6.1	6.9	26.0	0.86	12.4	14.9	1418	1213	415	0
64	Garrett A	-13.41	-112.15	39	133.99	5.1	5.6	5.9	2.8	0.14	2.2	2.7	87	12	43	1
65	Garrett BCD	-13.45	-111.53	26	133.94	5.3	5.8	5.8	4.1	0.37	1.8	2.2	47	17	32	C
66	Gauss	-35.00	54.12	59	12.23	6.1	6.1	6.2	4.9	0.43	9	10.7	530	227	84	0
67	Gazelle	-35.80	53.43	81	12.27	5.4	5.4	5.8	2.2	0.12	10.5	12.6	852	102	38	0
68	Geelvinck	-41.96	84.71	303	65.6	5.6	5.5	5.5	2.9	0.01	8.8	10.5	2668	25	18	0
69	Gemino	-22.78	69.29	38	40.99	5.3	4.9	5.4	0.6	0.06	4	4.7	150	8	14	0
70	George V A	-51.35	139.72	235	67.49	5.9	6.6	6.5	50.0	0.23	7.6	9.1	1797	422	191	0
71	George V B	-53.24	140.55	179	67.3	5.4	5.8	5.8	4.6	0.03	6.7	8	1196	39	40	0
72	GoC 24N	24.05	-108.77	133	50.37	5.7	6.1	6.1	9.9	0.13	6.7	7.9	885	112	76	0
73	GoC 25N	24.98	-109.52	119	49.85	6.2	6.8	6.7	35.0	0.52	6.3	7.6	753	395	269	0
74	Gofar A	-4.59	-105.85	95	124.55	5.5	6	6.2	18.0	0.24	3.6	4.3	341	83	86	1
75	Gofar B	-4.58	-105.26	29	124.4	5.2	5.9	6	3.7	0.29	2	2.4	58	17	62	1
76	Gofar C	-4.56	-104.88	46	124.3	5.6	6.1	6.1	9.4	0.38	2.5	3	115	43	64	1
77	Gough	-39.79	-16.23	56	28.98	0	5.1	5.2	0.1	0.01	5.7	6.8	319	2	10	0
78	Guafo	-44.70	-80.15	286	48.1	5.5	6.4	6.4	38.0	0.16	10	11.9	2857	448	157	0
79	Guamblin	-45.71	-77.37	80	48.27	5.7	6.1	6	4.9	0.14	5.3	6.3	422	57	60	0
80	Hayes	33.66	-38.65	80	21.65	5.8	5.8	6.1	3.9	0.16	7.8	9.4	629	102	71	0
81	Heemskerck A	-50.01	115.58	19	70.34	0	0	0	0.0	0.00	2.1	2.6	40	0	0	1

Table 3-S2: Global Compilation of Oceanic Transform Faults.

Fault	Name	Lat.	Long.	Length	Slip Rate	ms	mb	Mw	ΣM $*10^{18}$	χ	W_T	D600	A_T	A_E	A_C	Seg
#				(km)	(mm/yr)				(Nm)		(km)	(km)	(km^2)	(km^2)	(km^2)	
82	Heemskerck B	-49.88	115.93	24	70.34	0	0	0	0.0	0.00	2.4	2.9	57	0	0	1
83	Heemskerck C	-49.65	116.19	27	70.34	0	0	0	0.0	0.00	2.6	3	68	0	0	1
84	Heemskerck D	-49.40	116.47	31	70.33	0	0	0	0.0	0.00	2.8	3.3	84	0	0	1
85	Heezen	-55.42	-124.53	382	79.02	6	6.3	6.4	47.0	0.10	9	10.7	3441	337	139	0
86	Herron	-56.29	-139.07	26	75.45	5.8	5.8	5.9	2.1	0.25	2.4	2.9	63	16	42	0
87	Hillegom's Hole	-38.66	78.31	59	62.7	5.7	6.4	6.4	16.0	0.64	3.9	4.7	235	149	150	0
88	Hollister A	-54.22	-136.90	23	77.89	5.2	5.4	5.7	0.6	0.09	2.2	2.7	51	5	26	1
89	Hollister B	-54.35	-136.23	62	77.93	5.6	6.2	6.4	13.0	0.42	3.7	4.4	227	95	146	1
90	Hollister C	-54.53	-135.39	34	77.95	5.4	6	6.1	7.2	0.57	2.7	3.2	92	53	76	1
91	Indomed	-39.47	46.11	141	12.73	5.5	5.9	5.8	2.4	0.06	13.6	16.3	1921	108	38	0
92	Islas Orcadas	-54.18	6.10	100	12.85	5.8	6.1	6.1	3.7	0.14	11.5	13.6	1142	166	77	0
93	Jan Mayen A	71.37	-9.64	127	15.45	5.9	6.8	6.7	19.0	0.47	11.7	14	1491	708	309	1
94	Jan Mayen B	71.14	-7.39	27	15.45	6.1	6.2	6.2	6.1	1.56	5.3	6.5	145	227	96	1
95	Kane	23.74	-45.62	146	23.43	6.2	6.4	6.4	13.0	0.22	10.2	12.2	1492	322	147	0
96	L'Astronome	-59.65	-150.85	56	68.94	5.6	5.8	6	4.6	0.18	3.7	4.4	207	38	53	0
97	Le Geographe	-57.63	-147.50	70	71.9	5.7	5.9	5.9	3.0	0.08	4	4.8	283	24	50	0
98	Mabahiss	-3.04	68.12	42	30.48	0	0	0	0.0	0.00	4.8	5.7	202	0	0	0
99	MAR 15 20	15.28	-45.74	193	23.57	5.3	6	6	3.4	0.04	11.7	14	2262	83	55	0
100	MAR 18S	-17.72	-13.37	91	30.34	5.3	5.6	5.5	1.6	0.05	7.1	8.5	645	30	17	0
101	MAR 21S	-21.23	-11.72	45	30.4	4.8	0	4.9	0.0	0.00	4.9	5.9	224	1	5	0
102	MAR 22S A	-22.82	-13.26	85	30.39	5.3	5.1	5.4	0.4	0.01	6.8	8.2	582	8	13	1
103	MAR 22S B	-22.28	-12.37	86	30.4	4.9	5.3	5.2	0.2	0.01	6.9	8.2	592	4	9	1
104	MAR 22S C	-22.02	-11.83	22	30.4	4.9	4.6	5.2	0.1	0.02	3.5	4.2	76	2	9	1
105	MAR 25 50S	-25.66	-13.74	39	30.32	5.4	5.2	5.5	0.8	0.08	4.6	5.5	181	15	17	0
106	MAR 25S	-24.90	-13.55	37	30.35	5	5	5.4	0.3	0.04	4.5	5.4	167	6	14	0
107	MAR 29 45S	-29.76	-13.77	27	30.1	0	0	0	0.0	0.00	3.9	4.6	104	0	0	0
108	MAR 29S A	-29.19	-13.45	74	30.13	4.6	4.9	5	0.1	0.00	6.5	7.7	475	1	5	1
109	MAR 29S B	-28.87	-12.77	59	30.15	5.3	4.8	5.5	0.4	0.02	5.7	6.8	338	7	16	1
110	MAR 32S A	-32.50	-14.42	23	29.87	0	0	0	0.0	0.00	3.6	4.3	82	0	0	1
111	MAR 32S B	-32.27	-13.95	57	29.89	5.1	4.8	5.3	0.2	0.01	5.6	6.8	322	4	11	1
112	MAR 32S C	-32.11	-13.48	29	29.9	5.6	5.7	5.9	1.2	0.20	4.1	4.8	117	23	40	1
113	MAR 34S	-34.16	-14.83	69	29.71	5.2	5	5.3	0.5	0.02	6.3	7.5	431	9	10	0
114	MAR 35S	-35.40	-16.51	250	29.6	6	7	6.9	79.0	0.51	11.9	14.2	2975	1520	445	0
115	MAR 40S	-40.35	-16.64	40	28.9	0	0	0	0.0	0.00	4.9	5.8	192	0	0	0
116	MAR 50S	-49.13	-9.14	110	26.9	5.4	5.3	5.4	0.3	0.01	8.2	9.9	911	6	14	0
117	MAR 5S	-5.04	-11.94	78	29.27	5.5	5.1	5.6	0.5	0.02	6.7	8	521	9	23	0
118	Marathon	12.64	-44.46	88	24.41	5	5.1	5.5	0.6	0.02	7.8	9.3	684	15	19	0
119	Marie Celeste	-17.51	66.00	219	35.99	6	6.7	6.6	67.0	0.48	10.1	12.1	2213	1057	232	0
120	Marion	-46.47	33.66	109	13.22	5.7	6.1	6.2	6.1	0.21	11.8	14	1281	264	92	0
121	Melville	-29.84	60.78	92	11.74	6.1	6.8	6.9	31.0	1.43	11.5	13.7	1054	1508	462	0
122	Menard	-49.56	-115.24	208	85.47	5.7	6.5	6.4	37.0	0.19	6.4	7.6	1330	247	143	0
123	Novara	-31.43	58.41	45	11.93	0	0	0	0.0	0.00	8	9.5	362	0	0	0

61

Table 3-S2: Global Compilation of Oceanic Transform Faults.

Fault	Name	Lat.	Long.	Length	Slip Rate	ms	mb	Mw	ΣM $*10^{18}$	χ	W_T	D600	A_T	A_E	A_C	Seg
#				(km)	(mm/yr)				(Nm)		(km)	(km)	(km^2)	(km^2)	(km^2)	
124	Oceanographer	35.18	-35.64	121	21.27	5.8	6.3	6.3	19.0	0.43	9.8	11.7	1182	503	111	0
125	Orozco A	15.41	-105.11	46	87.81	4.3	4.5	5.1	0.1	0.00	2.9	3.6	137	1	6	0
126	Orozco B	15.16	-104.58	23	88.85	5.2	5.5	5.6	0.6	0.08	2.1	2.5	48	4	24	0
127	Owen	11.42	57.54	335	22.84	5.9	6.2	6.5	32.0	0.15	15.7	18.7	5254	802	162	0
128	PAR 161	-61.78	161.50	77	45.98	5.5	6.1	6	6.4	0.19	5.3	6.3	408	79	55	0
129	PAR 163	-62.10	163.36	85	46.71	5	5.2	5.3	0.2	0.01	5.5	6.6	470	3	11	0
130	PAR 165	-62.38	165.46	89	47.58	5.6	5.9	5.9	5.2	0.12	5.6	6.7	499	62	46	0
131	Pitman	-64.53	-170.78	71	56.74	0	0	0	0.0	0.00	4.6	5.5	325	0	0	0
132	Prince Edward	-45.45	35.13	146	13.19	5.8	6.3	6.4	15.0	0.32	13.6	16.3	1989	634	142	0
133	Quebrada A	-3.74	-103.68	27	123.12	5.1	4.9	5.6	0.8	0.07	1.9	2.3	52	4	23	1
134	Quebrada B	-3.73	-103.44	22	123.05	5	4.8	5.3	0.2	0.02	1.7	2.1	38	1	11	1
135	Quebrada CD	-3.75	-102.87	27	122.97	5.2	5.2	5.6	0.7	0.06	1.9	2.3	52	3	20	C
136	Raitt A	-54.33	-120.10	88	80.94	4.9	4.9	5.4	0.4	0.01	4.3	5.1	376	3	13	1
137	Raitt B	-54.49	-118.94	58	80.99	5.6	5.9	6	3.2	0.11	3.5	4.1	201	23	58	1
138	Rio Grande	-28.23	-12.94	57	30.19	4.9	5	5.2	0.3	0.02	5.6	6.7	321	6	10	0
139	Rivera A	19.57	-108.68	177	73	5.6	6.3	6.3	18.0	0.12	6.4	7.6	1130	138	125	1
140	Rivera B	18.76	-107.16	197	73	6.1	6.8	6.9	69.0	0.41	6.7	8	1326	540	440	1
141	Romanche	-0.53	-20.63	878	28.27	6.3	6.5	7.1	260.0	0.26	22.8	27.2	20036	5161	700	0
142	Saint Exupery	-62.24	-155.42	42	64.73	4.9	5.7	5.7	0.5	0.03	3.3	3.9	139	5	26	0
143	Saint Paul A	0.93	-29.02	297	27.71	6.3	6.5	6.6	40.0	0.21	13.4	16	3982	825	236	1
144	Saint Paul B	0.87	-27.04	146	27.77	5.4	5.6	5.9	4.5	0.07	9.4	11.2	1371	93	43	1
145	Saint Paul C	0.74	-25.92	96	27.83	5.6	6.1	6.1	8.4	0.24	7.6	9.1	730	172	66	1
146	Saint Paul D	0.62	-25.23	50	27.88	5.5	5.3	6	1.7	0.12	5.5	6.6	274	34	54	1
147	Sealark	-3.88	68.47	63	30.78	4.8	0	5.1	0.1	0.00	5.9	7	369	1	7	0
148	SEIR 100E	-47.68	99.81	129	69.46	6.1	6.6	6.5	27.0	0.31	5.6	6.7	721	223	189	0
149	SEIR 106E A	-49.09	106.26	56	70.11	0	4.4	5	0.0	0.00	3.7	4.4	205	0	6	1
150	SEIR 106E B	-48.64	106.79	59	70.12	5.2	5.3	5.5	0.7	0.03	3.8	4.5	222	6	16	1
151	SEIR 120	-49.49	120.42	154	70.19	5.1	4.8	5.3	0.2	0.00	6.1	7.2	935	1	11	0
152	SEIR 121	-49.36	121.53	80	70.13	5	5.3	5.3	0.6	0.01	4.4	5.2	350	5	10	0
153	SEIR 122	-49.71	122.73	50	70.04	5.4	5	5.3	0.1	0.01	3.5	4.1	173	1	11	0
154	SEIR 88E	-41.92	88.42	65	66.47	5.5	5.7	5.8	3.5	0.11	4	4.8	264	30	39	0
155	SEIR 96E A	-45.66	96.03	89	68.69	6	6.5	6.4	18.0	0.36	4.7	5.6	415	151	157	0
156	SEIR 96E B	-46.43	96.14	40	68.82	5.3	5.6	5.7	3.0	0.20	3.1	3.7	125	25	27	0
157	Shackelton	-59.77	-59.12	332	6.83	6.5	6.6	6.6	14.0	0.13	28.6	34.1	9477	1208	199	0
158	Shaka	-53.55	9.02	199	12.92	5.9	6.8	6.8	30.0	0.41	16.1	19.2	3198	1318	375	0
159	Siqueiros A	8.40	-104.05	24	112.24	5	5.4	5.5	0.8	0.08	1.9	2.3	46	4	18	1
160	Siqueiros B	8.38	-103.66	34	112.48	5	5	5.5	0.3	0.02	2.3	2.7	77	2	20	1
161	Siqueiros C	8.36	-103.42	18	112.68	5.2	5.8	5.8	3.3	0.56	1.7	2	30	17	32	1
162	Siqueiros D	8.36	-103.21	17	112.89	5.2	5.5	5.8	2.4	0.44	1.6	1.9	27	12	35	1
163	Siqueiros E	8.38	-103.00	17	112.96	5.4	5.8	5.9	2.5	0.47	1.6	1.9	27	13	43	1
164	Sovanco	48.98	-129.77	135	53.9	0	0	0	0.0	0.00	6.5	7.7	875	0	0	0
165	St Vincent	-54.50	144.12	58	66.5	5.6	5.9	5.9	7.9	0.30	3.9	4.6	222	67	48	0

Table 3-S2: Global Compilation of Oceanic Transform Faults.

Fault	Name	Lat.	Long.	Length	Slip Rate	ms	mb	Mw	ΣM $*10^{18}$	χ	W_T	D600	A_T	A_E	A_C	Seg
#				(km)	(mm/yr)				(Nm)		(km)	(km)	(km^2)	(km^2)	(km^2)	
166	Strakhov	3.94	-32.08	108	26.96	5.1	5.3	5.5	0.7	0.02	8.2	9.8	885	15	17	0
167	Tasman A	-55.23	146.33	90	66.05	6.2	6.9	6.9	34.0	0.68	4.8	5.7	431	291	401	1
168	Tasman B	-56.59	147.28	218	65.82	5.9	6.4	6.4	31.0	0.17	7.5	8.9	1626	268	151	1
169	Tasman C	-57.80	148.47	62	65.51	5.7	6.5	6.5	18.0	0.62	4	4.8	247	153	195	1
170	Tasman D	-58.87	149.25	173	65.29	6.1	6.2	6.3	14.0	0.10	6.7	8	1154	120	118	1
171	Tasman E	-59.89	150.57	82	65.29	5.8	6.5	6.5	14.0	0.33	4.6	5.5	377	125	174	0
172	Ter Tholen	-33.44	77.72	89	60.26	5	4.8	5.3	0.5	0.01	5	5.9	443	4	10	0
173	Tetyaev	-16.25	-13.75	123	30.28	5.6	5.2	5.5	0.5	0.01	8.2	9.9	1015	8	19	0
174	Tharp	-54.59	-131.12	462	78.82	5.9	6.7	6.6	53.0	0.08	9.9	11.8	4582	385	235	0
175	Tomayo	23.08	-108.34	65	50.95	5.4	6.2	6.5	8.6	0.32	4.6	5.5	301	96	163	0
176	Udintsev	-56.41	-142.43	325	74.49	5.8	6.4	6.4	38.0	0.10	8.6	10.2	2781	291	141	0
177	Vacquier	-53.04	-118.09	52	82.29	5.3	5.7	5.8	3.1	0.13	3.3	3.9	170	22	34	0
178	Valdavia A	-41.09	-91.56	49	47.42	5.1	5.1	5.4	0.8	0.05	4.2	5	204	9	15	1
179	Valdavia B	-41.20	-90.81	77	47.45	5.3	5.8	5.8	2.2	0.07	5.2	6.2	402	27	32	1
180	Valdavia C	-41.30	-89.74	97	47.47	5.1	5.4	5.7	1.5	0.03	5.9	7	568	18	28	1
181	Valdavia D	-41.35	-88.44	119	47.48	5.3	5.3	5.7	2.0	0.03	6.5	7.7	772	25	28	1
182	Valdavia E	-41.41	-86.72	165	47.51	5.4	5.6	5.9	4.3	0.04	7.6	9.1	1260	51	44	1
183	Valdavia F	-41.49	-85.14	69	47.54	5.1	5	5.3	0.3	0.01	4.9	5.9	340	3	11	1
184	Valdavia G	-41.57	-84.52	23	47.56	5.7	5.7	5.6	0.3	0.06	2.8	3.4	65	4	23	1
185	Vema	10.78	-42.29	307	24.98	6.4	6.9	6.9	95.0	0.49	14.4	17.1	4407	2175	485	0
186	Vema II	-8.92	67.44	237	30.63	5.2	5.8	6.2	8.1	0.06	11.4	13.6	2700	151	79	0
187	Vityaz	-5.69	68.37	105	31.14	5.2	5.6	5.7	0.7	0.02	7.5	9	790	13	25	0
188	Vlamingh	-41.47	80.36	123	64.35	6	6.4	6.4	32.0	0.41	5.7	6.8	697	287	154	0
189	Warringa A	-49.41	123.38	38	70	5.4	5	5.3	0.1	0.01	3	3.6	115	1	11	1
190	Warringa B	-49.07	123.87	49	69.97	0	0	0	0.0	0.00	3.4	4.1	168	0	0	1
191	Wilkes A	-9.02	-109.21	35	129.79	5.4	5.8	5.9	4.7	0.28	2.1	2.6	75	21	42	1
192	Wilkes B	-9.06	-108.69	74	129.74	5.5	6	6.1	4.9	0.09	3.1	3.7	230	22	63	1
193	Yaquina A	-6.25	-107.31	23	126.66	5.2	5.5	5.5	1.3	0.15	1.7	2.1	40	6	18	1
194	Yaquina B	-6.18	-106.99	21	126.51	4.8	4.9	5.2	0.3	0.03	1.6	2	35	1	9	1
195	Zeehaen	-50.12	114.12	71	70.35	5.4	5.6	5.6	2.3	0.06	4.1	4.9	292	18	24	0
196	Zeewolf A	-35.44	78.46	32	61.41	5.1	0	5	0.0	0.00	3	3.5	95	0	6	1
197	Zeewolf B	-35.18	78.64	29	61.36	5.1	4.9	5.3	0.5	0.06	2.8	3.4	82	5	11	1

4 | THE RELATIONSHIP BETWEEN SEISMICITY AND FAULT STRUCTURE ON THE DISCOVERY TRANSFORM FAULT, EAST PACIFIC RISE

4.1 Introduction

The work presented in this chapter was published online in the journal Geochemistry, Geophysics, Geosystems on September 29, 2014. The original research presented in this paper was conducted by me, with some of the data and methodology being provided by my coauthors. Unprocessed multibeam bathymetry data for the 2006 SeaBeam 2112 survey was obtained via the National Geophysical Data Center (NGDC). The unprocessed data for the 2008 Kongsberg Maritime EM302 survey was provided by Dr. Jeff McGuire from the Woods Hole Oceanographic Institute. All multibeam data used in this paper were cleaned and processed by me. The 24-year Mw $\geq$ Mw 5.4 earthquake catalog was obtained from the Global Centroid Moment Tensor Project. The seismic catalog derived from the ocean bottom seismometers was provided by Jeff McGuire. All earthquake relocations were run by me. Analysis and interpretation of the results was primarily conducted by me, with input and advice from my coauthors. The paper was also written by me, with edits by my coauthors.

4.2 Reprint of Article and Supporting Information

The relationship between seismicity and fault structure on the Discovery transform fault, East Pacific Rise

Monica Wolfson-Schwehr[1], Margaret S. Boettcher[1], Jeffrey J. McGuire[2], and John A. Collins[2]

[1]Department of Earth Sciences, University of New Hampshire, Durham, New Hampshire, USA, [2]Department of Geology and Geophysics, Woods Hole Oceanographic Institution, Woods Hole, Massachusetts, USA

Abstract There is a global seismic moment deficit on mid-ocean ridge transform faults, and the largest earthquakes on these faults do not rupture the full fault area. We explore the influence of physical fault structure, including step-overs in the fault trace, on the seismic behavior of the Discovery transform fault, 4S on the East Pacific Rise. One year of microseismicity recorded during a 2008 ocean bottom seismograph deployment (24,377 $0 \leq M_L \leq 4.6$ earthquakes) and 24 years of $Mw \geq 5.4$ earthquakes obtained from the Global Centroid Moment Tensor catalog, are correlated with surface fault structure delineated from high-resolution multibeam bathymetry. Each of the 15 $5.4 \leq Mw \leq 6.0$ earthquakes that occurred on Discovery between 1 January 1990 and 1 April 2014 was relocated into one of five distinct rupture patches using a teleseismic surface wave cross-correlation technique. Microseismicity was relocated using the HypoDD relocation algorithm. The western fault segment of Discovery (DW) is composed of three zones of varying structure and seismic behavior: a zone with no large events and abundant microseismicity, a fully coupled zone with large earthquakes, and a complex zone with multiple fault strands and abundant seismicity. In general, microseismicity is reduced within the patches defined by the large, repeating earthquakes. While the extent of the large rupture patches on DW correlates with physical features in the bathymetry, step-overs in the primary fault trace are not observed at patch boundaries, suggesting along-strike heterogeneity in fault zone properties controls the size and location of the large events.

1. Introduction

The Discovery transform fault, located at 4S on the East Pacific Rise (EPR, Figure 1), is ideal for investigating the relationship between seismic processes and fault structure. Discovery is a segmented transform fault, comprising two fault strands separated by an intratransform spreading center. Both fault strands contain multiple repeating-rupture patches that host Mw 5.4–6.0 earthquakes [*McGuire*, 2008]. Discovery was the site of a 2008 ocean bottom seismometer (OBS) deployment, as well as two high-resolution multibeam bathymetry surveys in 2006 and 2008. The bathymetry data enable the surface structure of the fault trace of Discovery to be delineated on a subkilometer scale, while the OBS data provide a high-resolution seismic database. These two data sets, combined with a 24 year record of seismicity obtained from the global Centroid Moment Tensor (CMT) catalog [*Dziewoński et al.*, 1981; *Ekström et al.*, 2012], are used to investigate whether fault structure influences seismic behavior along the segmented Discovery transform fault.

Discovery is representative of a typical mid-ocean ridge transform fault (RTF) in that the size and repeat time of the largest observed earthquakes scale with the seismogenic area of the fault [*Boettcher and Jordan*, 2004; *Boettcher and McGuire*, 2009]. The largest observed earthquakes on Discovery (Mw 6.0) are small compared to the full fault area and repeatedly rupture the same patch of the fault (Figure 2) [*McGuire*, 2008; *Boettcher and McGuire*, 2009]. Multiple large rupture patches occur on each fault segment and these patches fail when an accumulation of ∼50–100 cm of tectonic slip has been reached since the last large event, corresponding to a mean repeat time of 5.8 years [*McGuire*, 2008]. While the majority of plate motion on RTFs is accommodated aseismically [*Bird et al.*, 2002; *Boettcher and Jordan*, 2004], the largest events on many intermediate and fast-slipping RTFs occur on fully coupled fault patches [*Braunmiller and Nábělek*, 2008; *McGuire*, 2008; *Boettcher and McGuire*, 2009; *Sykes and Ekström*, 2012] separated by rupture barriers with low seismic coupling [*McGuire*, 2008; *McGuire et al.*, 2012].
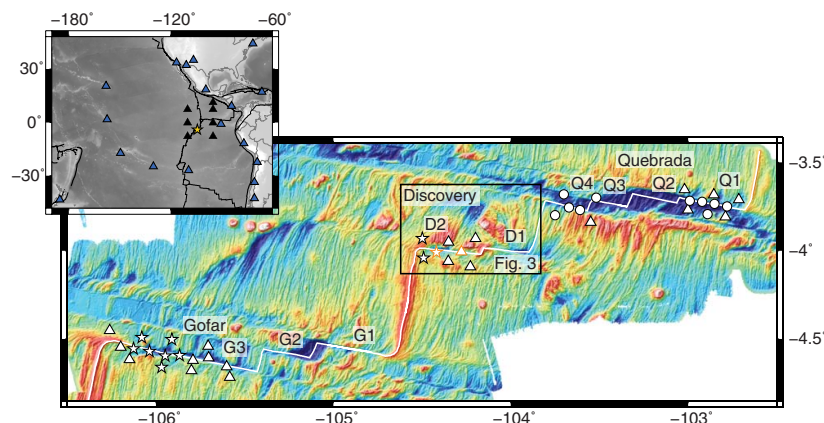
Figure 1. Base map: 2006 SeaBeam 2112 bathymetry data of the Quebrada, Discovery, and Gofar transform faults. Fault segments are numbered following *Searle* [1983]. In the text, D1 and D2 are referred to as DE and DW for clarity. Data are gridded at a 200 m resolution. White circles, triangles, and stars, respectively, indicate the locations of the short period, broadband, and broadband plus strong motion seismometers deployed during the 2008 OBS experiment. The star and triangle bordered in orange on Discovery represent stations D01 and D07, respectively. These two stations are referenced in section 4. The rectangle surrounding the Discovery transform fault delineates the area shown in Figure 3. Inset: Smith and Sandwell global topography data (v 15.1, 2013) for the equatorial Pacific. Blue triangles indicate the location of GSN stations used in the relocation analysis. Black triangles indicate the positions of the NOAA PMEL hydroacoustic array during the 1996–2001 deployment. Discovery is indicated by the gold star.

In 2008, *McGuire et al.* [2012] positioned an OBS array consisting of 30 broadband seismometers (10 collocated with strong-motion accelerometers) and 10 short-period seismometers on the Quebrada, Discovery, and Gofar transform fault system (QDG) on the EPR for a period of approximately 1 year (Figure 1), and successfully captured an Mw 6.0 earthquake on the westernmost segment (G3) of Gofar on 18 September 2008. In the 2 weeks prior to this event, more than 20,000 foreshocks were recorded on the OBS array [*McGuire et al.*, 2012]. These foreshocks clustered in a 10 km long zone located just east of the mainshock rupture patch. To the east of the foreshock zone is another rupture patch, which last failed in 2007 (Mw 6.2). Neither the 2008 nor the 2007 earthquakes appear to have ruptured across the foreshock region and into the adjacent patch. These observations indicate that there are regions of the fault that act both as barriers to large rupture propagation as well as loci for abundant microseismic activity, suggesting that the mechanical properties of the fault zone (the fault core and/or damage zone) vary along strike [*McGuire et al.*, 2012].

On continental strike-slip faults, *Wesnousky* [2006] found that fault step-overs on the order of 5 km in width act as physical barriers to rupture propagation. Along RTFs, compressional or dilational step-overs, intratransform spreading centers, and pull-apart basins can divide the fault into a series of parallel or subparallel fault segments [*Searle*, 1983] that may create barriers to rupture propagation. On Gofar, there appears to be a small jog in the fault trace at the western terminus of the foreshock zone, corresponding to a compressional bend at depth as evidenced by the microseismicity [*McGuire et al.*, 2012; *Froment et al.*, 2014]. The coincidence of this feature with the location of the barrier zone suggests that it may influence rupture propagation.

In this study, we examine the relationship between surface fault structure and the location and size of repeating-rupture patches, as well as the spatial relationship between rupture patches and microseismicity on the Discovery transform fault. We use two multibeam bathymetry data sets, SeaBeam 2012 data collected in 2006 (grid resolution: 200 m) and EM300 data collected in 2008 (grid resolution: 75 m), to delineate the fault trace on a subkilometer scale and relate the bathymetry to the locations of large (Mw $\geq$ 5.4) earthquakes that have occurred from 1992 to 2013 and microseismicity ($0 \leq M_L \leq 4.6$) recorded on Discovery during the 2008 OBS deployment. The goal of this study is to improve our understanding of how plate motion is accommodated along oceanic transform boundaries by investigating the influence of fault structure on the seismic behavior of the Discovery transform fault.
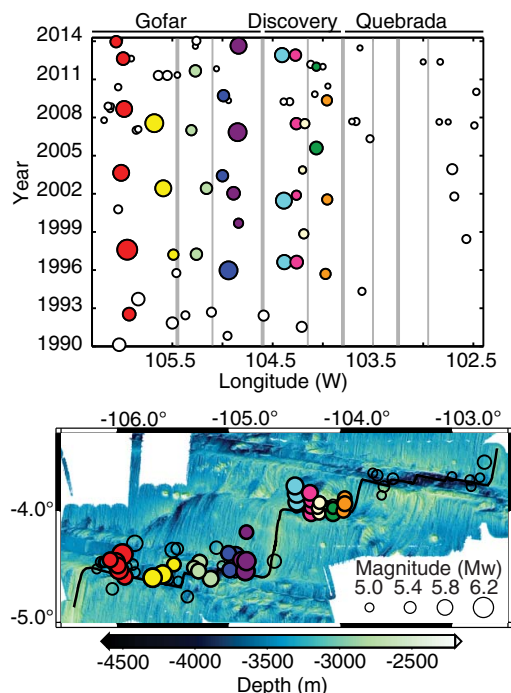
Figure 2. Map and space-time evolution of Mw ≥ 5.0 earthquakes on Quebrada, Discovery, and Gofar transform faults between 1 January 1990 and 1 March 2014, modified from *McGuire* [2008] and *McGuire et al.* [2012]. All earthquakes (circles) are sized by magnitude. Events on Quebrada and Gofar are shown at their CMT catalog locations. Events on Discovery are shown at their relocated longitude, and are offset in latitude so that all events are visible on the map. Earthquakes with overlapping ruptures (defined as relative centroid locations <5 km) [see *McGuire* 2008] are represented by circles of the same color. The vertical gray lines denote the location of mid-ocean ridge segments (thick lines) and intratransform spreading centers (thin lines).

2. Structure of the Discovery Transform Fault

The Discovery transform fault is a fast-slipping, left-lateral fault system composed of two subparallel fault strands separated by an intratransform spreading center [*Searle*, 1983] (ITSC; Figures 1 and 3). The slip-rate on Discovery is ∼12.6 cm/yr according to the Global Strain Rate Model (GSRM v1.2) [*Kreemer et al.*, 2003]. In contrast to Gofar and Quebrada, on Discovery there is a distinct lack of fracture zones beyond the ridge-transform intersections, and Discovery's strike (∼95 degrees) forms an obtuse angle with the EPR. These observations are consistent with findings from earlier studies suggesting that the plate geometry of the QDG fault system is still evolving [*Fox and Gallo*, 1989; *Forsyth et al.*, 2007; *Pickle et al.*, 2009]. The segments of Discovery are both defined by median valleys, and include dilational features (nodal basins and the ITSC) consistent with a component of extension across Discovery caused by the obtuse angle between Discovery and the EPR.

The western fault segment of Discovery (DW) is 36 km long and is defined by three distinct structural zones (Figures 3b and 3c). Zone A, the westernmost zone, is composed of a narrow and well-defined (300–500 m wide) fault valley extending from the ridge-transform intersection to 7 km along strike. Heading east, the fault valley broadens into two consecutive lozenge-shaped basins that comprise zone B. The first basin is 4 km long, 2 km wide, and ∼600 m deep relative to the surrounding seafloor. A small, 0.75 km wide ridge separates this basin from the larger, 7.5 km long, 2.5 km wide basin to the east (Figure 3b, purple arrow). Here the strike of the fault trace changes from approximately east-west to more west-northwest to east-southeast. This larger basin is the deepest part of DW, ∼900 m below the surrounding seafloor, and is terminated at its eastern extent by a 3.5 km wide ridge that crosscuts the transform valley (Figures 3b and 3c, yellow arrow). Zone C, the third structural zone, begins east of this ridge, where there is a series of 3–5 km long en echelon ridges (Figure 3b, pink arrow), which may be small fault strands making up a splay zone. This series of ridges is bounded to the south by the primary fault trace, and to the north by a 17 km long secondary fault trace.

The eastern fault segment of Discovery (DE) is composed of a single 27 km long fault zone that progressively widens from a narrow, well-defined fault trace at the ITSC into a broad, 4.5 km wide nodal basin along the inside corner of the eastern ridge-transform intersection (Figures 3b and 3c). The deepest part of DE occurs within the nodal basin and is ∼1150 m below the surrounding seafloor (Figure 3c). Small changes in strike (< 15°) occur along DE; the most notable of which are found where the fault zone begins to widen ∼8 km east of the ITSC and where it enters the nodal basin ∼15 km east of the ITSC.

The bathymetric expression of the ITSC separating the two segments of Discovery is broad and flat, with an average base width of 6 km and an average crest width of 1.4 km (Figure 3). The offset distance between

Figure 3. (a) Bathymetry of the Discovery transform fault and possible nanoplate. Foreground data: 75 m resolution EM300 multibeam bathymetry data collected in 2008. Background data: 200 m resolution SeaBeam 2112 multibeam bathymetry data collected in 2006. Both data sets use the same color scale. (b) Interpreted geology of the Discovery transform fault and possible nanoplate. A: axis-centered ridge-transform intersection high; B1 & B2: rotated crustal blocks; C: rift; D: north-south ridges; E: NE-SW trending abyssal hills; and F: abandoned rift. The thick white line outlines the region of rotated terrain that comprises the possible nanoplate. Solid white lines denote apparent compressional ridges. Long-dashed white lines indicate extensional zones and arrows indicate direction of extension. Short-dashed white lines indicate possible faults that offset features. White dashed-dotted lines highlight abyssal hill fabric. Circles outline some of the seamounts in the area. Black solid lines show the location of the EPR on either end of Discovery and outline the intratransform spreading center. Black long-dashed lines show the primary fault traces; short-dashed black line indicates the secondary trace on the western segment. Black-dotted lines outline the two consecutive lozenge-shaped valleys on the western fault segment, and delineate the width of the fault valley. Orange arrow denotes direction of rotation of the nanoplate. (c) Cross section with depth from DW to DW[1] of the western fault segment. (d) Cross section with depth from DE to DE[1] of the eastern fault segment.

the primary fault traces of DW and DE is ∼8 km; however, the total length of the ITSC is 14 km. The excess length results from sigmoidal shape of the ITSC, which may be due to fissure eruptions creating volcanic ridges extending at acute angles to the spreading direction, similar to the Joseph Mayes seamount on the Southwest Indian Ridge [*Dick et al.*, 2003]. Discovery's ITSC comprises a region of thickened crust [*Pickle et al.*, 2009], reaching a height of 700 m above the surrounding seafloor. It is anomalous compared to the ITSCs of Quebrada and Gofar, which are defined by axial valleys, such as those generally associated with slow-spreading ridges. *Pickle et al.* [2009] used gravity data along with the Seabeam 2112 bathymetry data set to infer crustal thickness throughout the QDG region. They found that the ITSCs on Quebrada and Gofar are well-established spreading centers, defined by a thin crust, variable melt supply, and depressed thermal structure. Conversely, the ITSC on Discovery recently developed as the fault changed configuration, and may represent a region of constructive volcanism over a preexisting plate.

The 70 km long ridge segment of the EPR linking Discovery with Gofar to the south is relatively narrow (1.5–5 km) and has a shallow axial high consistent with observations from many fast-spreading ridges, e.g., *Small* [1998] and *Shah and Buck* [2001] (Figure 3). The intersection between this ridge segment and DW (feature A, Figure 3b) is characterized by an "axis-centered" intersection high [*Barth et al.*, 1994]. Similar morphology has been observed at the RTIs of other transform faults on the EPR, including Clipperton [*Gallo et al.*, 1986; *Barth et al.*, 1994], Quebrada [*Lonsdale*, 1978], and Raitt [*Lonsdale*, 1994], and is thought to result from some combination of lateral heat transport across the fracture zone leading to thermal expansion [*Gallo et al.*, 1986; *Phipps Morgan and Forsyth*, 1988], and constructive/intrusive volcanism due to excess ridge volcanism [*Gallo et al.*, 1986; *Kastens et al.*, 1986].

The 35 km long EPR segment connecting Discovery with Quebrada to the north is characterized by a 5 km wide spreading center and a 200–300 m deep axial valley (Figure 3). Given the fast spreading rates associated with the EPR, the presence of a median valley along this ridge segment is unexpected. *Pickle et al.* [2009] attributes this to the possibility that a portion of the extension between the Pacific and Nazca plates along this ridge segment may be accommodated by the formation of grabens and dike injections to the west, effectively reducing the spreading rate along the ridge [*Forsyth et al.*, 2007].

Directly north of the ITSC on Discovery, there is an ∼850 km^2 region of complex, discordant terrain (Figure 3). Rotated crustal blocks containing oblique abyssal hill fabric (features B1 and B2, Figure 3b) are present within this region, and suggest a counterclockwise rotation of ∼45 degrees [*Forsyth et al.*, 2007]. This region is bounded to the west (104.3W) by a 7 km wide rift, or pull-apart basin (feature C, Figure 3b), that extends 35 km northeast of Discovery. A set of ridges (feature D, Figure 3b) that trend roughly north-south and bound the rift to the west is truncated to the northwest by abyssal hill fabric (feature E, Figure 3b) that cuts across the ridges at an angle of ∼45 degrees. The rift progressively deepens and curves slightly inward toward the northeast at its northern extent. Stair-stepped morphology along the flanks of seamounts (white circles in Figure 3b) within the rift indicates normal faulting. The morphology of the rift, specifically the deepening and inward curvature of the tip, is strikingly similar to the secondary rifts bounding the Wilkes nanoplate [*Goff et al.*, 1993] located at 9S on the EPR, the Easter Island microplate [*Naar and Hey*, 1991] located at 25S on the EPR, and the Juan Fernandez micro plate [*Bird et al.*, 1998] located at 33S on the EPR. An apparent abandoned rift segment (feature F, Figure 3b) located northwest of the rift, overprints the oblique abyssal hill fabric west of this region, suggesting that the abyssal hills predate the rotation and formation of this complex region. Small ridges and troughs bound this region to the north and east. Similar ridges and troughs are observed at the Wilkes nanoplate, where the free-air gravity anomaly suggests these features are formed, in part, by compressional upwarping and downwarping of the crust [*Goff et al.*, 1993]. The similarity between the morphology of the deformed region just north of Discovery and that at the Wilkes nanoplate suggests a similar mechanism of formation.

3. Repeating-Rupture Patches

To determine the role fault structure plays in controlling the location and size of rupture patches on Discovery, it was first necessary to determine absolute locations for the large repeating earthquakes because location errors of up to ∼50 km are common for mid-ocean earthquakes in global seismic catalogs [*Sverdrup*, 1987; *Cronin and Sverdrup*, 2003]. Following the relative surface-wave relocation technique described in *McGuire* [2008], earthquakes detected by the National Oceanic and Atmospheric Administration (NOAA)

hydroacoustic catalog were used as empirical Greens Functions (EGFs) to determine the absolute location for an Mw 5.5 earthquake in 1998. This event was subsequently used to estimate the absolute centroid locations of all other Mw $\geq$ 5.4 events that occurred between 1992 and 2013 using relative surface-wave arrival times.

The hydroacoustic earthquake catalog is compiled by NOAA's Pacific Marine Environmental Laboratory (PMEL) using data from a suite of hydrophone arrays, which were deployed in the eastern equatorial Pacific between 19 May 1996 and 19 October 2002 (Figure 1). The hydrophones record the tertiary waves (T-wave or T-phase) of earthquakes, i.e., the seismic energy of an earthquake that leaves the seafloor and travels through the water column as an acoustic wave. While uncertainties associated with T-phase source locations are small inside the hydroacoustic array ($<$ 2 km) [*Fox et al.*, 2001], this location does not necessarily represent the true epicenter or centroid of the earthquake, but rather the point at which most of the seismic energy leaves the oceanic crust and is converted into acoustic energy. To avoid location bias that may be introduced by topographic steering [*Fox et al.*, 2001; *Smith*, 2003], only events located on or near the fault trace, away from topographic highs were used in this analysis.

Thirteen events located by the hydroacoustic catalog were used to relocate the 1998 Mw 5.5 earthquake that ruptured a fault patch centrally located on Discovery, just west of the ITSC. Events from the hydroacoustic catalog were chosen on the basis of their magnitude (Mw $\geq$ 4.4) and location (events $>$ 5 km off the fault trace or located on a topographic high were excluded). Each of these earthquakes was used as an EGF to compute a relative location for the 1998 Mw 5.5 event using a cross correlation of the first orbital Rayleigh (R1) waves. The nucleation depth for earthquakes on RTFs is thought to be constrained by the 600°C isotherm [*Abercrombie and Ekström*, 2001; *Boettcher et al.*, 2007], which is relatively shallow for fast-slipping transforms on the EPR ($\leq$ 6 km). The relative depth and distance between each EGF and the 1998 Mw 5.5 event ($<$ 25 km) is small compared to the teleseismic distance between the events and the Global Seismic Network (GSN) stations ($>$ 1000s km); therefore, path effects between the EGF and the master event are assumed negligible. Seismicity in the NOAA hydroacoustic catalog is predominantly associated with transform faults, indicating that the focal mechanisms for these events should correspond to strike-slip motion on near-vertical faults [*Fox et al.*, 2001]. Given the similarity in location and focal mechanism, the R1 arrivals from the EGF and the target event are expected to have similar waveforms at the GSN stations. The primary differences between the two waveforms at a specific station are phase and amplitude, corresponding to differential arrival time and relative seismic moment, respectively [*McGuire*, 2008].

For each event, seismograms were obtained from a set of GSN stations that are azimuthally distributed around Discovery (Figure 1). The data were bandpass filtered between 0.02 and 0.04 Hz to isolate the R1 arrivals, as this bandwidth has a high signal-to-noise ratio and constant group velocity (3.7 km/s) for R1 waves in young oceanic lithosphere [*Nishimura and Forsyth*, 1988]. Waveform pairs with a cross-correlation coefficient $\geq$ 0.7 were used to compute the relative distance between events. The differential times were measured from the peak of the cross-correlation function and obvious outliers ($>$3 standard deviations from the mean) were removed. The remaining differential times were then fit to a cosine function using the L1 norm to minimize the effect of any outliers that fell below the 3 standard deviation cutoff. The scale and phase parameters of the cosine fit were used to obtain a relative distance and azimuth between the EGF and the master event (Figure 4). As in *McGuire* [2008], standard errors were computed for the parameters of the cosine fit using a bootstrap algorithm and assuming a Gaussian distribution with a 1 s standard deviation for the differential travel-time measurement errors. The errors were calculated as the standard deviation in location estimates after 100 iterations. Each event pair resulted in a single estimated location for the 1998 Mw 5.5 earthquake; these estimations were averaged to obtain the best estimate of the absolute centroid position (Table 1 and Figure 5a). Three of the 13 event pairs resulted in either a poor cosine fit, or a location estimate that was more than 5 km off the fault, and their estimated locations were not included in the average.

Three of the 10 events from the hydroacoustic catalog that were used in the relocation of the 1998 Mw 5.5 earthquake were also recorded in the CMT catalog. To ensure no circularity was introduced into our location procedure, we compared the location of the 1998 event obtained from averaging all 10 estimated locations with that obtained from averaging only estimated locations based on the seven events unique to the hydroacoustic catalog. The location estimate based on the seven events is ~0.5 km east of the location estimate based on all 10 earthquakes. The estimated absolute location of an event becomes more precise as

70

7/23/01 Mw 5.3 and 11/15/98 Mw 5.5

distance: 15+/–2 km azimuth: 269
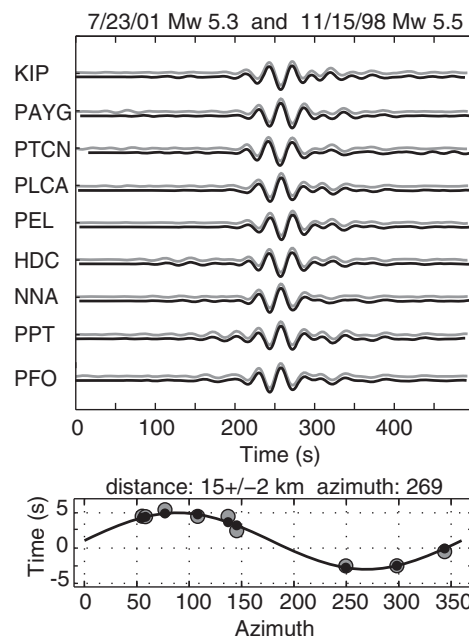
Figure 4. Relative relocation of the 1998 Mw 5.5 master event using a 2001 Mw 5.3 event located by the NOAA/PMEL hydroacoustic catalog as an EGF. (a) Aligned Rayleigh waves of the EGF (gray) and master event (black) filtered between 0.02 and 0.04 Hz at GSN stations. (b) Differential arrival times (gray) and best fit estimates from the cosine function (black). The master event is located 15 km from the NOAA/PMEL event, at an azimuth of 269 degrees.

the number of relative position estimates averaged together increases (uncertainty reduces by a factor of $1/\sqrt{N}$). A discrepancy of 0.5 km is within the reduced uncertainty of our averaged location ($\sim$0.6 km), and is therefore not significant.

The 1998 Mw 5.5 event was then used as an EGF to estimate the absolute positions for the remaining 14 Mw $\geq$ 5.4 earthquakes on Discovery recorded in the CMT catalog between 1992 and 2013 (Table 2 and Figure 5b). Each relocated event fell into one of five distinct patches; three on the DW (patches DW1, DW2, DW3) and two on DE (patches DE1, DE2) (Figure 6). These rupture patches, defined as areas on the fault where overlapping ruptures (centroids $\leq$ 5 km apart) repeatedly occur, include the four patches initially identified by *McGuire* [2008] and one additional patch with earthquakes in 2005 and 2012 (dark green circles in Figure 2). There was an Mw 5.6 earthquake in 1991 that may have ruptured either DW2 or DW3, but there were too few reliable stations to compute a robust location.

Mean rupture lengths were estimated for each rupture patch using:

$$R_L = \left(\frac{M_{0avg}}{\Delta\sigma}\right)^{2/3} Z^{-1} \quad (1)$$

where M_{0avg} is the averaged seismic moment release of all earthquakes belonging to that patch, $\Delta\sigma$ is the static stress drop that is assumed to be constant at 3 MPa [*Allmann and Shearer*, 2009; *Boettcher and McGuire*, 2009], and Z is the maximum depth of rupture that is assumed to be 5 km, consistent with the mean depth of the microseismicity on Discovery and Gofar [*McGuire et al.*, 2012]. To obtain equation (1), we follow *Boettcher and Jordan* [2004] and assume average earthquake slip, D, scales as the square root of the rupture area, A, as $D = \Delta\sigma\mu^{-1}A^{1/2}$. Combining the equation for D with the equation for seismic moment $M_0 = \mu A D$, where μ, the shear modulus, is 44.1 GPa, the value obtained for the lower crust from the Preliminary Earth Reference Model (PREM) [*Dziewonski and Anderson*, 1981] gives us equation (1).

Table 1. Hydroacoustic (t-Phase) Events Used in the Relocation of the 1998 Mw 5.5 Event[a]

Event #	Latitude	Longitude	Date	Time	Mw	Estimated 1998 Event Latitude	Estimated 1998 Event Longitude
1	−3.9970	−104.3990	23 Aug 1996	21:56:16	5.9	−4.0269	−104.2096
2	−4.0070	−104.2530	23 Aug 1996	22:19:06	5.9	−4.0353	−104.1658
3	−4.0120	−104.0020	8 Jun 1997	21:02:43	5.1	−4.0253	−104.1933
4	−4.0180	−103.9090	12 Aug 1997	3:49:49	4.4	−4.0090	−104.1674
5	−4.0360	−103.9580	7 May 2000	6:18:45	4.4	−4.0281	−104.1830
6	−4.0170	−104.2200	26 Jun 2001	15:22:32	4.7	−4.0331	−104.1908
7	−4.0150	−103.9870	23 Jul 2001	10:34:34	5.1	−4.0050	−104.1785
8	−3.9810	−104.0680	23 Jul 2001	9:43:08	5.3	−3.9833	−104.2014
9	−3.9930	−104.0400	23 Jul 2001	10:06:57	4.4	−3.9875	−104.1983
10	−4.0290	−103.9760	23 Jul 2001	4:34:49	5.6	−4.0168	−104.2092
Averaged centroid location for the 1998 Mw 5.5 event:						−4.0150	−104.1897

[a]Dates and times are UTC.
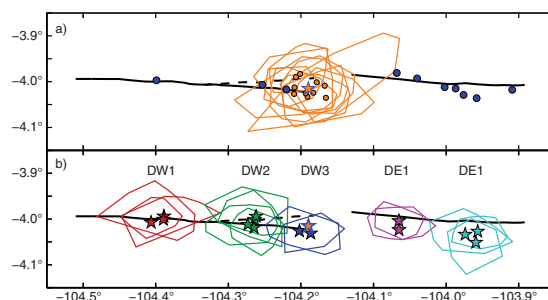
Figure 5. (a) Relocation of the 1998 Mw 5.5 earthquake. Blue circles show the location of events from the NOAA/PMEL hydroacoustic catalog used to calculate relative positions for the 1998 event. Orange circles denote relative position estimates of the 1998 event. The orange polygons outline the uncertainty in each relative position estimated from the bootstrap algorithm described in the text. The orange star with the blue border represents the absolute centroid of the 1998 event obtained by averaging the relative relocations. (b) Relocation of the repeating Mw $\geq$ 5.4 earthquakes in the CMT catalog. Stars represent the estimated centroid positions relative to the 1998 Mw 5.5 event. Polygons outline the estimated uncertainty in position. In both plots, the black lines denote the western and eastern fault traces of the Discovery transform (solid: primary, dashed: secondary).

Rupture patch DW1 has an estimated length of 10 km and is the largest patch on Discovery, hosting Mw 5.9–6.0 earthquakes (Figure 6). Rupture patch DW2 is located ~5 km east of patch DW1 and hosts Mw 5.5–5.8 earthquakes with an estimated rupture length of ~6 km. The smallest rupture patch on Discovery is DW3, located just west of the ITSC. DW3 has a length of ~3 km and fails in Mw 5.4–5.5 events.

The calculated locations for the two 5 km long rupture patches on DE (patches DE1 and DE2) are just south of the fault trace (Figure 6). Patch DE1 is located 9 km east of the ITSC and is ~2 km south of the transform valley. Patch DE2, the easternmost rupture patch, is located ~3 km south of the fault valley. This is likely due to event mislocation. Figure 5b shows the location uncertainty associated with each earthquake relocated in this study, calculated using the bootstrap method. For both patches, the fault trace is within the computed location uncertainty. There is additional uncertainty associated with the velocity structure underlying Discovery. The relocation scheme assumes an R1 wave velocity value that is representative of young oceanic lithosphere and does not take into account localized variations. While the path effects between the EGF and the event being relocated is typically considered negligible compared to the path effects between the events and the GSN stations, it is possible that there is some unknown local variation, particularly underlying the ITSC, that is significant enough to affect the relocation scheme. These uncertainties, combined with the lack of fault structure south of the eastern segment in the bathymetry data suggest that patch DE1 and DE2 actually lie on the eastern fault trace.

4. Microseismicity

The 2008 OBS deployment on the QDG fault system recorded 24,377 earthquakes (0.16 $\leq M_L \leq$ 4.58, magnitude of completeness for DW: 0.9 and DE: 2.0) on Discovery between 1 January and 31 December. There were no large repeating earthquakes on Discovery during the deployment period. The Antelope software package was used to generate an earthquake catalog from the OBS data using standard short-term average to long-term average (STA/LTA)-based detection algorithms [*Houliston et al.*, 1984] for P-waves and wavelet-based detections [*Simons et al.*, 2006] for S-wave arrivals (see supporting information for detailed methodology). On DW, the majority of earthquakes in the catalog cluster within 5 km of the primary fault trace (gray circles, Figure 7). Earthquakes extend outside both the western RTI (Figure 7; Area I) and eastern ITSC-intersection (Figure 7; Area II). There is a 2 km long zone located at

Table 2. Estimated Centroid Locations of the 15 Mw $\geq$ 5.4 Repeating Earthquakes[a]

Rupture Patch	Date	Time	Latitude	Longitude	Mw
DW1	23 Aug 1996	21:56:13	−4.0010	−104.3893	5.9
	26 Jun 2001	12:34:00	−3.9941	−104.3887	6.0
	17 Dec 2012	17:41:37	−4.0740	−104.4068	5.9
DW2	23 Aug 1996	22:19:04	−3.9944	−104.2616	5.8
	29 Nov 2001	17:07:06	−4.0020	−104.2634	5.5
	23 Jul 2007	6:03:55	−4.0189	−104.2644	5.6
	17 Dec 2012	17:46:50	−4.0121	−104.2726	5.8
DW3	15 Nov 1998	4:51:49	−4.0150	−104.1897	5.5
	26 Nov 2003	17:32:55	−4.0267	−104.2022	5.4
	23 Jul 2007	6:00:38	−4.0318	−104.1867	5.5
DE1	21 Aug 2005	9:49:54	−4.0237	−104.0647	5.8
	17 Jan 2012	15:27:52	−4.0041	−104.0649	5.4
DE2	16 Sep 1995	22:49:22	−4.0339	−103.9733	5.6
	30 Jul 2001	4:34:50	−4.0272	−103.9565	5.6
	24 May 2009	9:57:16	−4.0514	−103.9591	5.7

[a]Dates and times are UTC.
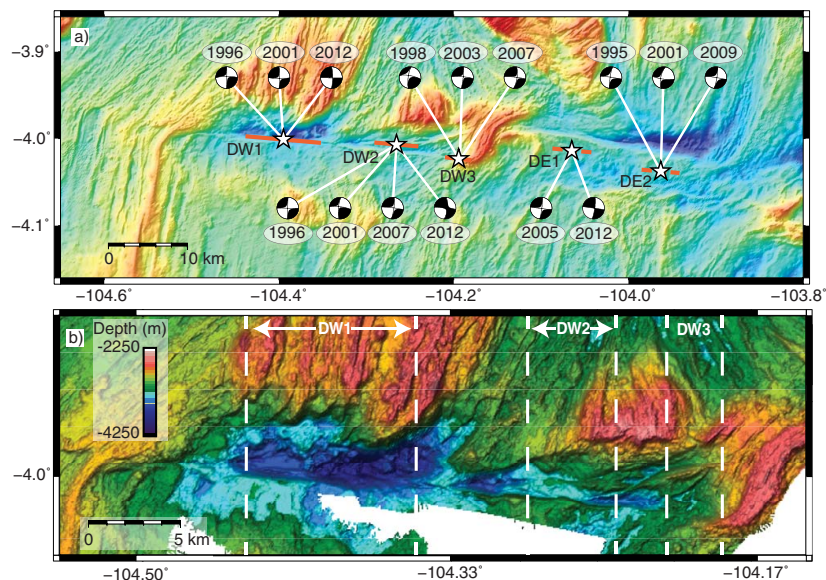
Figure 6. (a) Repeating-rupture patch locations on the Discovery transform fault. White stars denote the averaged location of earthquake centroids for each patch. Red lines represent the estimated rupture length centered on each centroid. The repeating earthquakes in each rupture patch are shown by their focal mechanism and year. (b) A zoomed in view of the fault structure and extent of the rupture patches on DW.

~104.5W on the western fault segment in which very few earthquakes occurred (Figure 7; Area III). A small cluster of earthquakes is located on the crustal block just north of the possible splay zone (~104.22W). On DE, which is outside the OBS array, the majority of recorded earthquakes cluster north of the transform valley within 16 km of the ITSC.

Earthquakes in the Antelope-generated catalog were relocated using the HypoDD double-difference algorithm [*Waldhauser and Ellsworth*, 2000] to estimate more robust positions. The microseismicity was divided into seven overlapping groups, subset by longitude (Figure 7). Groups 1–4 cover DW, group 5 is centered on the ITSC, and groups 6 and 7 cover DE. The earthquakes within group 7 were located > 20 km outside of the OBS array and were not relocatable. Only earthquakes that had detections on five or more stations (minimum of 10 associated P and S arrivals) were used in the relocation analysis (17,017 events). Differential
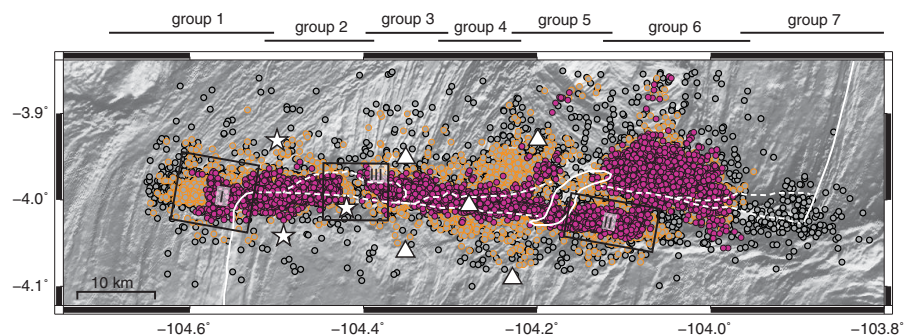
Figure 7. Microseismicity on the Discovery transform fault. Gray circles: STA/LTA catalog locations. Gray circles with orange border: events from the STA/LTA catalog that were successfully relocated by HypoDD. Pink circles: relocated positions. White solid lines denote the location of the EPR and outline the ITSC. White-dashed lines indicate the width of the fault valley on both the western and eastern fault segments. Areas I, II, and III are described in the text.
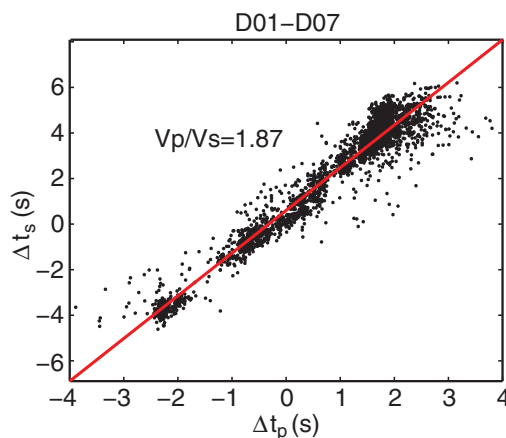
Figure 8. The difference in S-wave first arrival times (*y* axis) versus P-wave (*x* axis) first arrival times for microearthquakes on DW recorded at stations D01 and D07 (see Figure 1 for station locations). The red line represents a linear least squares regression to the data and is indicative of the Vp/Vs ratio in the lower crust between the two stations.

arrival times were calculated via waveform cross correlation for P and S waves. A window of 2.56 s centered on the arrival was extracted from each waveform, and subsequently tapered and bandpass filtered between 5–12 Hz for S waves and 5–15 Hz for P waves. Event pairs required a minimum of six differential time observations per pair with a cross-correlation coefficient ≥ 0.75. Catalog arrival times were not used due to the higher uncertainty associated with the increased percentage of misidentified phases. The relocation of events within groups 1–4 were based on a minimum of nine observations per event pair, as these groups fall within, or directly adjacent to, the OBS array. Relocations for events within groups 5 and 6 were based on a minimum of eight and six observations per pair, respectively, as these groups are located increasingly farther outside the OBS array. A one-dimensional version of

the P-wave velocity model developed by *Roland et al.* [2012] for the Gofar transform fault was used. The Vp/Vs ratio of 1.87 was obtained by fitting a linear least squares regression to differential S-wave versus P-wave arrival times for the two stations located on the fault trace (D01 and D07; Figures 1 and 8). This Vp/Vs ratio is on the upper end of the expected range from studies of oceanic crustal rocks [*Christensen*, 1972; *Anderson*, 1989; *Barclay et al.*, 2001] and may reflect localized high porosity, as was interpreted by *Roland et al.* [2012] and *McGuire et al.* [2012] for Gofar.

A total of 12,635 earthquakes out of the original 17,017 (~74%) were successfully relocated using the HypoDD algorithm (pink circles in Figure 7). For events located inside the overlapping region of two groups, final location estimates were obtained by averaging the relocated positions (median difference in position estimates from all overlapping groups is ~1.8 km). The large cluster of events on DE tightens up slightly, but remains predominantly located north of the fault trace. These events fall outside the OBS array, thus their locations are less certain than those on DW. Along DW, the location of the microseismicity tightened up along the fault trace so that 95% of events were within 3 km of the fault trace. The latitudinal spread of the microseismicity is likely due to a combination of unaccounted for location uncertainty and the occurrence of events in the damage zone surrounding the fault core [e.g., *Valoroso et al.*, 2014]. Microseismic activity extends ~4.5 km outside the western RTI and ~9 km beyond the ITSC intersection. The region of reduced seismicity in Area III is more distinct in the relocated catalog. Earthquakes on either side of this region have moved outward relative to their initial locations, forming a gap within which there is no microseismicity at all.

Perhaps the most striking observation is the extension of microseismic activity beyond the western RTI and ITSC intersection (Areas I and II; Figure 7); such activity is not observed on the neighboring Gofar transform fault. Although seismic activity has been observed along the fracture zones of other RTFs, these events are primarily associated with shorter-lived aftershock sequences related to mainshocks that occurred on the active transform [*Bohnenstiehl et al.*, 2004] or complex stress regimes related to the Mendocino Triple Junction [*Sverdrup*, 1987]. On Discovery, the extension of microseismicity beyond the active fault boundaries occurs throughout the entire deployment period. Comparison of waveform arrivals between a few of the events located west of the RTI and events located on the active western fault segment suggest that these events do occur outside the RTI and are not mislocated (see supporting information). The extension of events beyond the endpoints of DW is in line with the general trend of seismicity on the active fault trace and with the strike of the fault itself, suggesting that events in Areas I and II (Figure 7) may be related to the propagation of fracture zones. The change in the strike of the microseismicity from approximately east-west to more northwest-southeast coincides with the change in strike of the active fault trace, and indicates that
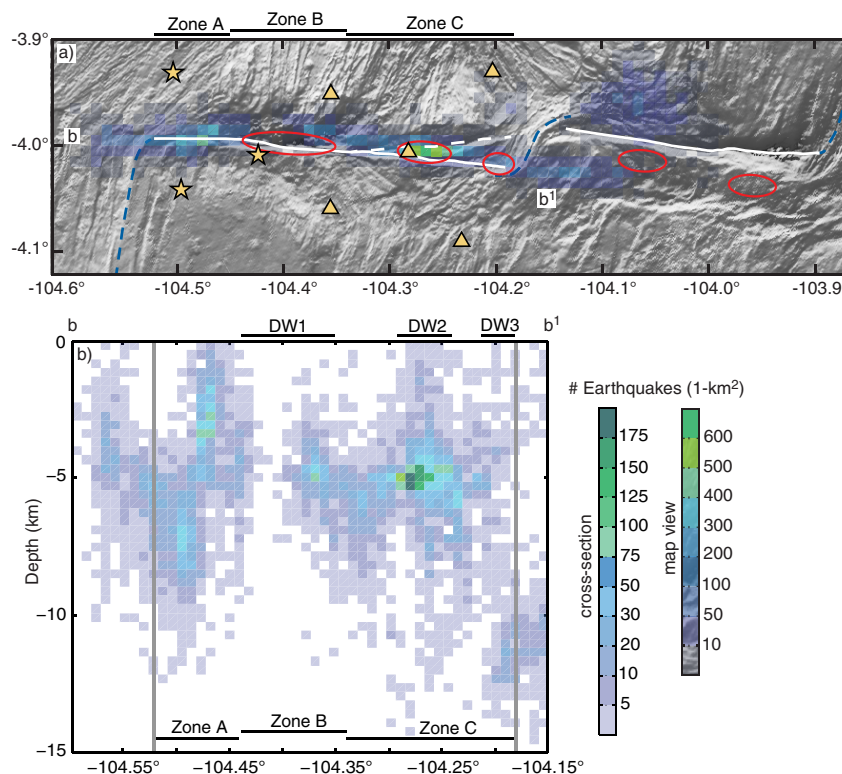
Figure 9. (a) Map view of the seismicity on the Discovery transform fault. Red ellipses are centered on the rupture patch centroid locations and indicate rupture length. Microseismicity is represented as a density plot (boxes are 1 km-by-1 km). White lines denote the primary (solid) and secondary (dashed) fault trace. Blue-dashed lines denote the ridge segments and the ITSC. Gold stars represent the broadband seismometers and gold triangles indicate broadband seismometers with strong motion sensors. The density plot shows that the majority of recorded microseismicity occurs along the western fault segment. The highest density coincides with rupture patch 2, located in the splay zone. The seismic gap coincides with DW1, the largest rupture patch. (b) Cross section along the western segment of Discovery showing a density plot of the microseismicity with depth for b–b^1. All microseismicity is projected into a single vertical plane. Boxes are 1 km-by-1 km. Vertical gray lines indicate the location of the EPR and ITSC.

the surface fault trace reflects aspects of the fault structure at depth. The inflection point in the strike of the microseismicity appears to lie within the 3 km long microseismic gap (Area III; Figure 7). This gap appears to be real (see supporting information), reflecting an area of the fault that was completely locked during the OBS deployment. *McGuire and Collins* [2013] used seafloor geodesy to show that within millimeter-level precision, this part of the fault was indeed locked during 2008.

5. Discussion

The relationship between seismicity and fault structure in zones A and B on DW (Figure 9) is strikingly similar to what is observed on the western end of the G3 segment of the Gofar transform fault, also studied during this experiment (Figures 1 and 2) [*McGuire et al.*, 2012; *Froment, et al.*, 2014] where strongly coupled fault patches are separated by zones of abundant microseismicity that do not appear to rupture in the large earthquakes. Zone A on Discovery comprises the narrow, well-defined fault trace that extends from the RTI eastward ~7 km along the fault. This zone appears to be a barrier to large ruptures as there are no Mw > 5 earthquakes recorded in this region over the 45 year span of the CMT catalog (see Figure 2 for the past 24 years), although the CMT catalog is only complete down to Mw 5.4 for QDG. Zone A is structurally and mechanically comparable to western end of G3 [*McGuire et al.*, 2012; *Froment et al.*, 2014], which is also relatively narrow, well-defined, devoid of large events, and contains abundant microseismicity. On both faults,

the western RTI is defined by an intersection high that spills over onto the older plate with prominent abyssal hill fabric. Microseismicity on westernmost G3 appears to split into two branches, suggesting that the fault zone in this region may be composed of two subparallel fault strands [*Froment, et al.,* 2014].

Zone B encompasses the largest repeating-rupture patch on Discovery, DW1, which is located in the deepest portion of the fault within the two adjacent lozenge-shaped valleys. The gap in the microseismicity is located within zone B, coinciding with the centroid location of patch DW1 (Figure 9). The lack of microseismicity in the large rupture patch is consistent with the accumulation of a slip deficit between earthquakes and supports the interpretations that the patch is fully coupled. The extent of rupture patch DW1 corresponds to the narrowing and shallowing of the transform valley as it exits the two consecutive valleys at either end of zone B. The eastern extent of DW1 also coincides with the 3.5 km wide cross-transform ridge (Figure 3b, yellow arrow). Mechanically, zone B on DW is comparable to segment 2 on G3, which includes the rupture patch that hosted the 2008 Mw 6.0 earthquake [*Froment, et al.,* 2014]. Microseismicity within the Mw 6.0 rupture patches on G3 during the interseismic period is minimal [*McGuire et al.,* 2012], similar to DW1.

The clear pattern observed on both western G3 and western DW, where a large rupture patch is confined by small-scale bathymetric features and surrounded by zones of low seismic coupling and high rates of microseismicity, is not observed in zone C on DW. Zone C is the most complex region of Discovery. The highest density of microseismicity, two repeating-rupture patches, DW2 and DW3, and a zone of small en echelon ridges that extend from the cross-transform ridge to the ITSC are all located within zone C (Figure 9). The high concentration of microseismicity within zone C coincides with the location of DW2, suggesting very different behavior to that observed for DW1 and the G3 rupture patches. It is possible that the secondary fault trace and some of the small en echelon fault strands are active in addition to the primary fault trace, and may accommodate some of the microseismicity in this zone. There is a small cluster of earthquakes between patches DW2 and DW3. Patch DW3 contains some microseismicity, though some of this seismicity may be associated with activity on the ITSC.

The majority of the microseismicity on DW locates in the crust shallower than 6 km (Figure 9b), as expected from the short transform fault length and fast slip rate on Discovery, consistent with observations on Gofar [*McGuire et al.,* 2012]. While some microseismicity in Figure 9b appears to extend well into the upper mantle, these depths are not well constrained due to insufficient station spacing. The depth resolution is poorest outside of the array, where the deepest seismicity is shown.

On both G3 and DW, small structural features on the order of 0.5-km or greater coincide with some of the rupture patch boundaries. On G3, there appears to be an ~600 m wide step-over in the fault trace at the western end of the foreshock zone that separates the two large repeating-rupture patches. This step-over coincides with a 600 m long bend in the trend of the microseismicity as it exits the foreshock zone [*Froment et al.,* 2014]. On DW, the structural features that correlate with the extents of the rupture patches do not appear to offset the primary fault trace in the cross-transform direction, though the ability to detect such offsets is limited by the resolution of the bathymetry data (75–200 m).

Observations from both Discovery and Gofar suggest that step-overs in the fault trace are not required for a structural feature to act as a barrier to rupture propagation. Small structural features, including step-overs in the fault trace, may be associated with an increased damage zone width or intensity. Enhanced fracturing in the damage zone may allow for increased porosity and subsequent dilatant strengthening during large events, providing a mechanism for halting rupture propagation. Increased porosity has been invoked to explain the observed decrease in P-wave velocities in the foreshock zone on G3 in the weeks leading up to the Mw 6.0 mainshock [*McGuire et al.,* 2012; *Roland et al.,* 2012]. Dilatant step-overs in the fault trace have been observed to stop rupture on continental strike-slip faults [*Sibson,* 1987; *Harris and Day,* 1993; *Wesnousky,* 2006], through a process thought to involve extensional fracturing at the rupture tip, leading to reduction in fluid pressure and subsequent dilatant strengthening [*Sibson,* 1987]. Compressional step-overs may also stop rupture due to an increase in the mean and normal stresses acting on the fault [*Harris and Day,* 1993; *Wesnousky,* 2006]. In both cases, field observations on continental strike-slip faults [*Knuepfer,* 1989; *Wesnousky,* 2006] agree with dynamic rupture models [*Harris and Day,* 1993] and indicate a step-over of ~5 km will stop rupture propagation. Furthermore, *Harris and Day* [1993] found that in dynamic rupture models, the dimension of fault step required to stop rupture was dependent on rupture velocity and stress

drop. For subshear rupture-velocities and stress drops of 3 MPa, compressional and dilational step-overs were found to stop rupture at dimensions less than 1 km.

Even with the complexity in zone C, all but one of the structural features in the fault trace that we are able to resolve (Figure 3) correlate with either the boundary of a large earthquake rupture patch or are the foci of abundant microseismicity (Figure 9). Rupture patch DW2 is bounded to the west by the narrowing of the possible splay zone as it approaches the cross-transform ridge. The eastern terminus of DW2 may be associated with one of the en echelon faults that make up the possible splay zone. Patch DW3 is the smallest rupture patch on Discovery and is located just west of the ITSC. The eastern end of DW3 extends to the ITSC-intersection. The length scale of segmentation derived from the structural complexity in zone C matches the length of rupture patches DW2 and DW3. The only feature that is not observed to correlate with either the end of a repeating-rupture patch or abundant microseismicity is the small, 0.75 km wide ridge that separates the two lozenge-shaped valleys located near the center of the DW1 rupture patch in zone B.

The relationship between fault structure and seismicity on the eastern segment of Discovery is not well constrained. DE is composed of a single fault valley that progressively widens from a narrow, well-defined fault trace near the ITSC to a broad, deep nodal basin approaching the eastern RTI. DE hosts two repeating-rupture patches, DE1 and DE2, as well as a cluster of microseismicity located just north of the fault trace (Figure 9). The OBS network did not cover DE, which significantly increased the magnitude of completeness and reduced the location accuracy of the recorded microseismicity. In addition, the 1998 Mw 5.5 event used to relocate the large, repeating earthquakes was located on DW. It is possible that the velocity structure under the ITSC may have influenced the relocation procedure, and thus reduced the accuracy of the large events locations on DE compared with DW. Acknowledging the uncertainty in the large event locations, it appears that DE1 occurs along the part of the fault that is still relatively narrow and well defined, while DE2 is located within the nodal basin.

Evidence of stress-transfer can be seen in three sets of Mw $\geq$ 5.4 earthquakes that occur minutes apart in adjacent patches. On 23 August 1996, DW2 hosted a Mw 5.8 earthquake ~23 min after a Mw 5.9 earthquake ruptured DW1. The same pattern repeated on 17 December 2012, with only ~6 min between events. On 23 July 2007, DW3 ruptured in a Mw 5.5 earthquake ~3 min prior to a Mw 5.6 rupture on patch DW2. In all three cases, the second earthquake was located about 1–2 rupture lengths from the first, and patch DW2 was the last to rupture. These observations suggest that either static or dynamic stress transfer may be an important triggering mechanism on DW.

Liu et al. [2012] modeled seismic cycles on RTFs using rate and state-dependent friction to explore the relationship between earthquake behavior and global RTF scaling relations. This model does not require along-fault heterogeneity in material properties in order to satisfy the observed scaling relations of *Boettcher and Jordan* [2004] and *Boettcher and McGuire* [2009], but it does require large nucleation zone sizes and an increase in the characteristic slip distance with fault width. The results of *Liu et al.* [2012] correspond to a multimode hypothesis of earthquake rupture [*Boettcher and Jordan*, 2004] in which a fault patch transitions between seismic and aseismic slip over many earthquake cycles. In these models, the large earthquakes jump around between cycles nucleating in different patches of the fault until eventually the entire fault has ruptured. The Mw $\geq$ 5.4 earthquakes observed on Discovery and Gofar, however, repeatedly rupture the same fault patches over the 24 years of the CMT catalog used in this study (Figure 2), following the single-mode hypothesis of *Boettcher and Jordan* [2004] and suggesting that rupture patches and barriers remain stable over multiple seismic cycles. Therefore, along-strike heterogeneity in fault properties is likely the cause of the slip deficit.

6. Conclusions

This study examined the correlation between fault structure and seismic behavior on the Discovery transform fault, located at 4S on the East Pacific Rise. The western fault segment of Discovery is composed of three distinct mechanical zones, including a zone that acts as a barrier to large rupture propagation, with no large earthquakes and abundant microseismicity, a fully coupled zone with large earthquakes, and a complex zone with multiple fault strands and abundant seismicity. While fracture zone traces are not evident in the bathymetry, microseismicity extends beyond the western RTI and the ITSC intersection, suggesting nascent fracture zone formation. The rotated block of complex terrain centered immediately north of

the ITSC may be an active nanoplate similar to that just north of the Wilkes transform fault, and suggests a complex regional stress regime surrounding Discovery. The obtuse angle of Discovery to the EPR combined with the lack of fracture zones and extension of microseismicity beyond the active fault trace suggest that Discovery is a relatively young and still evolving transform fault.

The primary focus of this study is whether or not structural features evident in the bathymetry data, including small step-overs in the surface fault trace, are a controlling factor in the size and location of the large, repeating-rupture patches. There are no step-overs in the fault trace ≥ 1 km that coincide with the endpoints of the large rupture patches on Discovery. Rupture patch boundaries do correlate with other structural features that do not offset the fault trace, such as the 3.5 km wide cross-transform ridge and the small en echelon faults, suggesting that step-overs greater than 1 km are not required to terminate ruptures on RTFs. The large repeating-rupture patches are separated by 5–10 km long regions that do not rupture in Mw ≥ 5.4 earthquakes. The rate of microseismicity varies strongly between the largest rupture patch (DW1) and the neighboring regions of the fault zone, similar to what is observed on Gofar. These observations suggest that along-strike heterogeneity in fault and damage zone properties partitions RTFs into regions that either fail in large, repeating earthquakes or regions that act as barriers to large rupture propagation and generate abundant microseismicity. It is these heterogeneities, rather than any large (≥ 1 km wide) step over in the fault trace, that appear to limit the size of the largest repeating earthquakes on RTFs and prevent them from rupturing the whole fault.

References

Abercrombie, R. E., and G. Ekström (2001), Earthquake slip on oceanic transform faults, *Nature*, *410*(6824), 74–77.

Allmann, B. P., and P. M. Shearer (2009), Global variations of stress drop for moderate to large earthquakes, *J. Geophys. Res.*, *114*, B01310, doi:10.1029/2008JB005821.

Anderson, D. L. (1989), The crust and upper mantle, in *Theory of the Earth*, pp. 45–62, Blackwell Sci., Boston, Mass.

Barclay, A. H., D. R. Toomey, and S. C. Solomon (2001), Microearthquake characteristics and crustal V_P/V_S structure at the mid-Atlantic ridge, 35°N, *J. Geophys. Res.*, *106*(B2), 2017–2034, doi:10.1029/2000JB900371.

Barth, G. A., K. A. Kastens, and E. M. Klein (1994), The origin of bathymetric highs at ridge-transform intersections: A multi-disciplinary case study at the Clipperton Fracture Zone, *Mar. Geophys. Res.*, *16*(1), 1–50.

Bird, P., Y. Y. Kagan, and D. D. Jackson (2002), Plate tectonics and earthquake potential of spreading ridges and oceanic transform faults, in *Plate Boundary Zones, Geophys. Monogr. Ser.*, vol. 30, edited by S. Stein and J. T. Freymueller, pp. 203–218, AGU, Washington, D. C.

Bird, R. T., D. F. Naar, R. L. Larson, R. C. Searle, and C. R. Scotese (1998), Plate tectonic reconstructions of the Juan Fernandez microplate: Transformation from internal shear to rigid rotation, *J. Geophys. Res.*, *103*(B4), 7049–7067, doi:10.1029/97JB02133.

Boettcher, M. S., and T. H. Jordan (2004), Earthquake scaling relations for mid-ocean ridge transform faults, *J. Geophys. Res.*, *109*, B12302, doi:10.1029/2004JB003110.

Boettcher, M. S., and J. J. McGuire (2009), Scaling relations for seismic cycles on mid-ocean ridge transform faults, *Geophys. Res. Lett.*, *36*, L21301, doi:10.1029/2009GL040115.

Boettcher, M. S., G. Hirth, and B. Evans (2007), Olivine friction at the base of oceanic seismogenic zones, *J. Geophys. Res.*, *112*, B01205, doi: 10.1029/2006JB004301.

Bohnenstiehl, D. R., M. Tolstoy, and E. Chapp (2004), Breaking into the plate: A 7.6 Mw fracture-zone earthquake adjacent to the Central Indian Ridge, *Geophys. Res. Lett.*, *31*, L02615, doi:10.1029/2003GL018981.

Braunmiller, J., and J. Nábělek (2008), Segmentation of the Blanco Transform Fault Zone from earthquake analysis: Complex tectonics of an oceanic transform fault, *J. Geophys. Res.*, *113*, B07108, doi:10.1029/2007JB005213.

Christensen, N. I. (1972), The abundance of serpentinites in the oceanic crust, *J. Geol.*, *80*(6), 709–719.

Cronin, V. S., and K. A. Sverdrup (2003), Multiple-event relocation of historic earthquakes along Blanco Transform Fault Zone, NE Pacific, *Geophys. Res. Lett.*, *30*(19), 2001, doi:10.1029/2003GL018086.

Dick, H. J. B., J. Lin, and H. Schouten (2003), An ultraslow-spreading class of ocean ridge, *Nature*, *426*, 405–412.

Dziewonski, A. M., and D. L. Anderson (1981), Preliminary reference Earth model, *Phys. Earth Planet. Inter.*, *25*(4), 297–356, doi:10.1016/0031–9201(81)90046-7.

Dziewoński, A. M., T. A. Chou, and J. H. Woodhouse (1981), Determination of earthquake source parameters from waveform data for studies of global and regional seismicity, *J. Geophys. Res.*, *86*(B4), 2825–2852, doi:10.1029/JB086iB04p02825.

Ekström, G., M. Nettles, and A. M. Dziewoński (2012), The global CMT project 2004–2010: Centroid-moment tensors for 13,017 earthquakes, *Phys. Earth Planet. Inter.*, *200*, 1–9, doi:10.1016/j.pepi.2012.04.002.

Forsyth, D. W., L. Kerber, and R. Pickle (2007), Co-existing overlapping-spreading-center and ridge-transform geometry, *Eos Trans. AGU*, *88*(52), Fall Meet. Suppl., Abstract T32B–05.

Fox, C. G., H. Matsumoto, and T.-K. A. Lau (2001), Monitoring Pacific Ocean seismicity from an autonomous hydrophone array, *J. Geophys. Res.*, *106*(B3), 4183–4206, doi:10.1029/2000JB900404.

Fox, P. J., and D. G. Gallo (1989), Transforms of the Eastern Pacific, in *The Eastern Pacific Ocean and Hawaii*, edited by E. L. Winterer, D. M. Hussong, and R. W. Decker, pp. 111–124, Geol. Soc. of Am., Boulder, Colo.

Froment, B., J. J. McGuire, R. D. van der Hilst, P. Gouédard, E. C. Roland, H. Zhang, and J. A. Collins (2014), Imaging along-strike variations in mechanical properties of the Gofar transform fault, East Pacific Rise, *J. Geophys. Res.*, doi:10.1002/2014JB011270, in press.

Gallo, D. G., P. J. Fox, and K. C. Macdonald (1986), A Sea Beam investigation of the Clipperton transform fault: The morphotectonic expression of a fast slipping transform boundary, *J. Geophys. Res.*, *91*(B3), 3455–3467, doi:10.1029/JB091iB03p03455.

Goff, J. A., D. J. Fornari, J. R. Cochran, C. Keeley, and A. Malinverno (1993), Wilkes transform system and "nanoplate," *Geology*, *21*(7), 623–626.

Harris, R. A., and S. M. Day (1993), Dynamics of fault interaction: Parallel strike-slip faults, *J. Geophys. Res.*, *98*(B3), 4461–4472, doi:10.1029/92JB02272.

Houliston, D. J., G. Waugh, and J. Laughlin (1984), Automatic real-time event detection for seismic networks, *Comput. Geosci.*, *10*(4), 431–436, doi:10.1016/0098-3004(84)90043-8.

Kastens, K. A., W. B. F. Ryan, and P. J. Fox (1986), Structural and volcanic expression of a fast slipping ridge-transform-ridge-plate boundary: Sea MARC I and photographic surveys at the Clipperton transform fault, *J. Geophys. Res.*, *91*(B3), 3469–3488, doi:10.1029/JB091iB03p03469.

Knuepfer, P. L. K. (1989), Implications of the characteristics of end-points of historical surface fault ruptures for the nature of fault segmentation, *U.S. Geol. Surv. Open-File Rep.*, *89–315*, 193–228.

Kreemer, C., W. E. E. Holt, and A. J. Haines (2003), An integrated global model of present-day plate motions and plate boundary deformation, *Geophys. J. Int.*, *154*(1), 8–34, doi:10.1046/j.1365-246X.2003.01917.x.

Liu, Y., J. J. McGuire, and M. D. Behn (2012), Frictional behavior of oceanic transform faults and its influence on earthquake characteristics, *J. Geophys. Res.*, *117*, B04315, doi:10.1029/2011JB009025.

Lonsdale, P. (1978), Near-bottom reconnaissance of a fast-slipping transform fault zone at the Pacific-Nazca plate boundary, *J. Geol.*, *86*, 451–472.

Lonsdale, P. (1994), Structural geomorphology of the Eltanin fault system and adjacent transform faults of the Pacific-Antarctic plate boundary, *Mar. Geophys. Res.*, *16*(2), 105–143.

McGuire, J. J. (2008), Seismic cycles and earthquake predictability on East Pacific Rise transform faults, *Bull. Seismol. Soc. Am.*, *98*(3), 1067–1084.

McGuire, J. J., and J. A. Collins (2013), Millimeter-level precision in a seafloor geodesy experiment at the Discovery transform fault, East Pacific Rise, *Geochem. Geophys. Geosyst.*, *14*, 4392–4402, doi:10.1002/ggge.20225.

McGuire, J. J., J. A. Collins, P. Gouédard, E. C. Roland, D. Lizarralde, M. S. Boettcher, M. D. Behn, and R. D. van der Hilst (2012), Variations in earthquake rupture properties along the Gofar transform fault, East Pacific Rise, *Nat. Geosci.*, *5*(5), 336–341, doi:10.1038/ngeo1454.

Naar, D. F., and R. N. Hey (1991), Tectonic evolution of the Easter microplate, *J. Geophys. Res.*, *96*(B5), 7961–7993, doi:10.1029/90JB02398.

Nishimura, C. E., and D. W. Forsyth (1988), Rayleigh wave phase velocities in the Pacific with implications for azimuthal anisotropy and lateral heterogeneities, *Geophys. J. Int.*, *94*, 479–501, doi:10.1111/j.1365-246X.1988.tb02270.x.

Phipps Morgan, J., and D. W. Forsyth (1988), Three-dimensional flow and temperature perturbations due to a transform offset: Effects on oceanic crustal and upper mantle structure, *J. Geophys. Res.*, *93*(B4), 2955–2966, doi:10.1029/JB093iB04p02955.

Pickle, R. C., D. W. Forsyth, N. Harmon, A. N. Nagle, and A. Saal (2009), Thermo-mechanical control of axial topography of intra-transform spreading centers, *Earth Planet. Sci. Lett.*, *284*(3-4), 343–351.

Roland, E. C., D. Lizarralde, J. J. McGuire, and J. A. Collins (2012), Seismic velocity constraints on the material properties that control earthquake behavior at the Quebrada-Discovery-Gofar transform faults, East Pacific Rise, *J. Geophys. Res.*, *117*, B11102, doi:10.1029/2012JB009422.

Searle, R. C. (1983), Multiple, closely spaced transform faults in fast-slipping fracture zones, *Geology*, *11*(10), 607–610.

Shah, A. K., and W. R. Buck (2001), Causes for axial high topography at mid-ocean ridges and the role of crustal thermal structure, *J. Geophys. Res.*, *106*(12), 30,865–30,879, doi:10.1029/2000JB000079.

Sibson, R. H. (1987), Earthquake rupturing as a mineralizing agent in hydrothermal systems, *Geology*, *15*(8), 701–704.

Simons, F. J., B. D. E. Dando, and R. M. Allen (2006), Automatic detection and rapid determination of earthquake magnitude by wavelet multiscale analysis of the primary arrival, *Earth Planet. Sci. Lett.*, *250*(1-2), 214–223, doi:10.1016/j.epsl.2006.07.039.

Small, C. (1998), Global systematics of mid-ocean ridge morphology, in *Faulting and Magmatism at Mid-Ocean Ridges*, edited by W. Roger Buck et al., AGU, Washington, D. C., doi:10.1029/GM106p0001.

Smith, D. K. (2003), Spatial and temporal distribution of seismicity along the northern Mid-Atlantic Ridge (15°−35°N), *J. Geophys. Res.*, *108*(B3), 2167, doi:10.1029/2002JB001964.

Sverdrup, K. A. (1987), Multiple-event relocation of earthquakes near the Gorda Rise: Mendocino fracture zone intersection, *Geophys. Res. Lett.*, *14*(4), 347–350, doi:10.1029/GL014i004p00347.

Sykes, L. R., and G. Ekström (2012), Earthquakes along Eltanin transform system, SE Pacific Ocean: Fault segments characterized by strong and poor seismic coupling and implications for long-term earthquake prediction, *Geophys. J. Int.*, *188*(2), 421–434, doi:10.1111/j.1365-246X.2011.05284.x.

Valoroso, L., L. Chiaraluce, and C. Collettini (2014), Earthquakes and fault zone structure, *Geology*, *42*(4), 343–346, doi:10.1130/G35071.1.

Waldhauser, F., and W. L. Ellsworth (2000), A double-difference earthquake location algorithm: Method and application to the northern Hayward fault, California, *Bull. Seismol. Soc. Am.*, *90*(6), 1353–1368.

Wesnousky, S. G. (2006), Predicting the endpoints of earthquake ruptures, *Nature*, *444*(7117), 358–360.

The Relationship between Seismicity and Fault Structure on the Discovery Transform Fault, East Pacific Rise

Monica Wolfson-Schwehr,[1] Margaret S. Boettcher,[1] Jeffrey J. McGuire,[2] and

John A. Collins[2]

1. Generation of the Microseismic Earthquake Catalog

The catalog of microseismicity was generated using STA/LTA-based detection algorithms [*Houliston et al.*, 1984] for P-waves and wavelet-based detections [*Simons et al.*, 2006] for S-wave arrivals. Associations were based on both P- and S-wave arrivals, and required a minimum of 5 phases. P-wave arrivals were picked from waveforms that were bandpass filtered between 8 - 18 Hz, with time windows of 0.5 s for short-term average and 2.0 s for the long-term average, and a signal-to-noise ratio of 2.5. S-wave arrivals were picked from waveforms bandpass filtered between 1 - 10 Hz and windowed into a 5.12 s long time-series starting at the time of the P-wave pick. These waveforms were then decomposed into their wavelet coefficients using the Cohen-Daubechies-Feauveau wavelet basis. Picks were calculated as the first coefficient of the second scale to exceed a threshold as discussed in *Simons et al.* [2006]. Maximum travel time residuals were set to 1.0 s and 1.5 s for P-waves and S-waves, respectively. Over 24,000 microseismic events were

---

Corresponding author: M. Wolfson-Schwehr, Department of Earth Sciences, University of New Hampshire, Durham, NH 03824, USA. (monica.schwehr@gmail.com)

detected on Discovery during the deployment period, consequently an analyst did not go through and review all the picks.

2. Extension of Microseismicity beyond the Active Fault Trace

The extension of microseismicity beyond the active fault trace is observed at both the western RTI and the transform-ITSC intersection. Similar behavior is not observed along the neighboring Gofar transform fault. These regions of extension are located outside the OBS array, suggesting that the event locations may be the result of poor location estimates in both the STA/LTA and HypoDD-relocated catalogs. In order to investigate this we compare the S-wave and P-wave arrivals for two earthquakes, one located outside the western RTI and one located on the western fault segment, at three OBS stations along Discovery.

All three stations used in this comparison are broadband accelerometers with strong motion detectors. Stations D02 and D03 are located ∼6 km from the RTI and are situated on either side of the fault. Station D01 is located ∼11 km from the RTI, directly on the fault. Event 1, mL 3.2, is located ∼4 km west of the RTI and event 2, mL 3.1, is located ∼3 km east of the RTI, directly on the fault. For both events, the P-waves and S-waves arrive at stations D03 and D02 first, and then station D01, as expected. The arrival times for event 1 are longer relative to event 2 at all three stations, suggesting that it is, indeed, located west of event 1 and the RTI (Fig. S1).

3. Possible Explanations for the Existence of the Microseismic Gap

Three possible explanations for the existence of the gap in microseismicity seen in the relocated event positions have been considered. The preferred explanation is that the

Page 2

gap is real, and reflects an area of the fault that was completely locked during 2008. *McGuire and Collins* [2013] used seafloor geodesy to show that this part of the fault was locked during 2008, and this is the explanation discussed in the main text. The other two explanations involve measurement errors. The exact velocity structure underlying the seismic gap on Discovery is not known; however, it is possible that an extreme low velocity anomaly exists in this region. However, by analogy to Gofar [*Roland et al.*, 2012; *Froment et al.*, 2014], this area is expected to have a relatively fast velocity structure as it coincides with the location of the largest repeating-rupture patch. Furthermore, the 1D velocity model used in HypoDD to relocate the microseismic events on Discovery already accounts for significantly reduced velocities in the crust (reductions up to 0.5 - 1.0 km/s, $\sim$10 - 20%) based on the results of a tomographic inversion of the P-wave velocity structure on Gofar [*Roland et al.*, 2012]. It seems unlikely, therefore, that there is a localized zone around station D01 in which seismic velocities are reduced even further. A third possibility is that a clock bias at station D01 is responsible for creating the gap. If arrivals at station D01 were recorded at a later time than they actually arrived, the event locations would be pushed away from the station. However, a clock bias would be accommodated to some degree by the HypoDD relocation process, and would be evident as relatively high time residuals for events pairs involving events recorded at station D01. The fact that relatively high time residuals are not seen in the data, combined with the seemingly low likelihood of a significant low velocity zone underlying station D01 and no movement in the geodetic data, suggests that the gap in microseismicity is a real feature.

References

Froment, B., P. Gouédard, E. C. Roland, H. Zhang, J. A. Collins, R. D. van der Hilst, and
J. J. McGuire (2014), Imaging along-strike variations in mechanical properties of the
Gofar transform fault, East Pacific Rise, *J. Geophys. Res.*, doi:10.1002/2014JB011270,
in press.

Houliston, D. J., G. Waugh, and J. Laughlin (1984), Automatic real-time event de-
tection for seismic networks, *Comput. Geosci.*, *10*(4), 431–436, doi:10.1016/0098-
3004(84)90043-8.

McGuire, J. J., and J. A. Collins (2013), Millimeter-level precision in a seafloor geodesy
experiment at the Discovery transform fault, East Pacific Rise, *Geochem. Geophys.
Geosys.*, *14*(1), 4392–4402, doi:10.1002/ggge.20225.

Roland, E. C., D. Lizarralde, J. J. McGuire, and J. A. Collins (2012), Seismic velocity con-
straints on the material properties that control earthquake behavior at the Quebrada-
Discovery-Gofar transform faults, East Pacific Rise, *J. Geophys. Res.*, *117*(B11102),
doi:10.1029/2012JB009422.

Simons, F. J., B. D. E. Dando, and R. M. Allen (2006), Automatic detection and rapid
determination of earthquake magnitude by wavelet multiscale analysis of the primary
arrival, *Earth Planet. Sci. Lett.*, *250*(1-2), 214–223, doi:10.1016/j.epsl.2006.07.039.
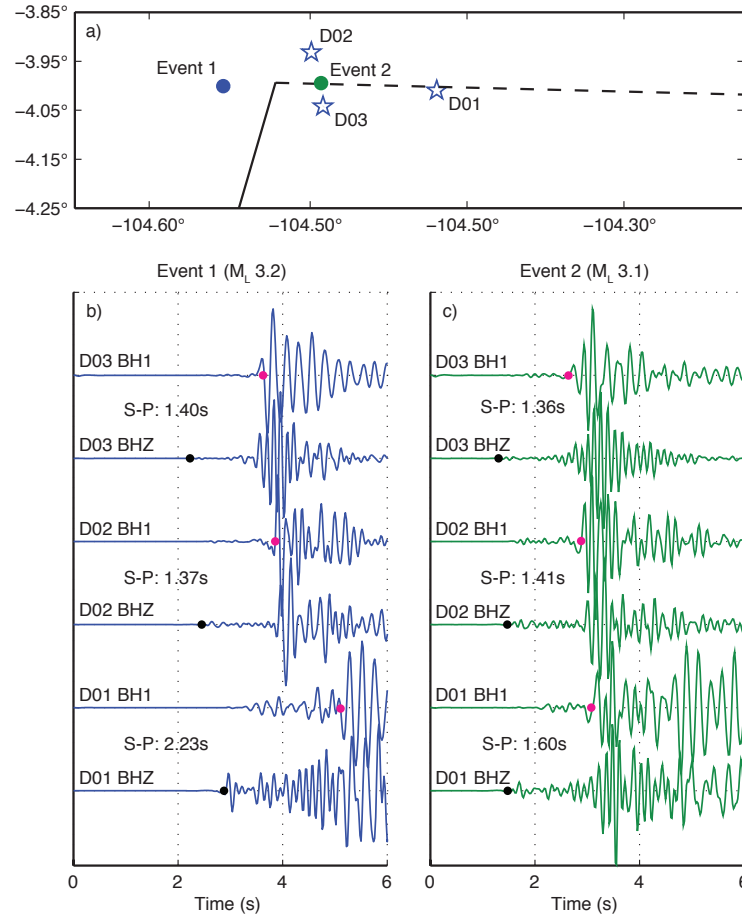
Figure S1.   (a) Simplified map-view of DW. The dashed-line represents the active transform fault and the solid line denotes the EPR. Blue stars denote the location of stations D01 - D03. Event 1 (blue circle) is located ∼4 km west of the RTI. Event 2 (green circle) is located ∼3 east of the RTI. Both events are shown at their relocated positions. (b) and (c) show the waveform arrivals at stations D01, D02, and D03 for event 1 and event 2, respectively. BH1 is one of the horizontal components of the seismometer and BHZ is the vertical. Waveforms are bandpass filtered between 2 and 10 Hz. The black dots on the BHZ waveforms mark the P-wave arrival, while the pink dots on the BH1 waveforms mark the S-wave arrival.

5 | CONCLUSION

The research presented in this dissertation focused on understanding the relationship between segmentation of mid-ocean ridge transform faults (RTFs) and the underlying thermal structure and seismic behavior of the fault. Specifically, this dissertation sought to determine whether segmentation could explain the low seismic coupling and small earthquake size observed on RTFs. To this end, three specific questions were addressed:

1. How is segmentation related to the underlying thermal structure of the fault?

2. How prevalent is RTF segmentation and how does it affect global scaling relations?

3. What is the relationship between fault structure and seismicity on the Discovery Transform Fault?

Segmentation was found to occur on many of the word's mid-ocean ridge transform faults, from those offsetting the ultraslow-spreading Southeast Indian Ridge to faults on the fastest spreading segments of the East Pacific Rise. The results from both the thermal modeling and the case study on Discovery suggest that offsets on the order of 5 km or greater may have a significant effect on the underlying thermal structure of an RTF and act as barriers to rupture prorogation. However, the scaling analysis showed that segmentation alone cannot account for the low seismic coupling and small earthquake size observed globally on RTFs. These observations suggest that other factors, such as dynamic rupture processes, the state of stress on the faults, and heterogeneity in along-strike fault and damage zone properties (e.g. porosity) limit the size and location of the largest repeating

ruptures on RTFs.

Future work addressing the relationship between fault structure and seismicity on oceanic transform faults would benefit from more OBS deployments on oceanic transform faults, accompanied by more high-resolution multibeam bathymetry surveys. This would allow for more detailed case studies, such as the one on the Discovery Transform Fault presented in Chapter 4. The need for more high-resolution multibeam bathymetry is really ubiquitous for all RTFs. The thermal modeling work presented in Chapter 1 suggests that offsets on the order of 5 km are sufficient to thermally decouple two adjacent fault segment on some moderate to fast-slipping fault. The majority of RTFs have not been surveyed by multibeam sonar, and thus the only bathymetry we have for these faults is the predicted bathymetry from satellite altimetry data, which has trouble resolving features smaller than $\sim$12 km. This indicates that the global bathymetric grids that are currently available are not able to capture the level of detail necessary to determine whether or not two adjacent fault segment are decoupled. This research would also benefit from dynamic rupture modeling, to understand how earthquakes nucleating on one fault segment may respond upon encountering a fault offset. That does not necessarily mean, however, that a rupture could not jump a 5-km long offset and continue on along the adjacent fault segment. More finite element analysis in which non-orthogonal offsets were modeled in order to determine the effect of constraining versus releasing bends on the underlying thermal structure of the faults would also be a great compliment to the work presented in this dissertation. While many offsets appear to be orthogonal to the adjacent fault segments on mid-ocean ridge transform faults, it is an overgeneralization to treat all offsets as such.

While the questions of low seismic coupling and small earthquake size on RTFs remain, the work presented in this dissertation improved our knowledge on the interplay between fault structure and seismicity on these faults, and laid the foundation for future work.

REFERENCES

Abercrombie, Rachel E, & Ekström, Göran. 2001. Earthquake slip on oceanic transform faults. *Nature*, **410**(6824), 74–77. 34

Behn, Mark D, Boettcher, Margaret S, & Hirth, Greg. 2007. Thermal structure of oceanic transform faults. *Geology*, **35**(4), 307–310. 4, 13, 33

Bird, Peter, Kagan, Yan Y, & Jackson, David D. 2002. Plate Tectonics and Earthquake Potential of Spreading Ridges and Oceanic Transform Faults. *Pages 203–218 of:* Stein, S, & Freymueller, Jeff (eds), *Plate Boundary Zones*. Washington, D. C.: American Geophysical Union. 7, 34, 41, 42

Bird, Robert T, Naar, David F, Larson, Roger L, Searle, Roger C, & Scotese, Christopher R. 1998. Plate tectonic reconstructions of the Juan Fernandez microplate: Transformation from internal shear to rigid rotation. *J. Geophys. Res.*, **103**(B4), 7049–7067. 30

Boettcher, Margaret S, & Jordan, Thomas H. 2004. Earthquake scaling relations for mid-ocean ridge transform faults. *J. Geophys. Res.*, **109**(B12302). 1, 2, 4, 7, 13, 30, 34, 35, 36, 40, 41, 42, 43, 45, 49, 50, 52

Boettcher, Margaret S, & McGuire, Jeffery J. 2009. Scaling relations for seismic cycles on mid-ocean ridge transform faults. *Geophys. Res. Lett.*, **36**(L21301). 1, 4, 7, 18, 35, 40, 47, 48, 52

Boettcher, Margaret S, Hirth, Greg, & Evans, Brian. 2007. Olivine friction at the base of oceanic seismogenic zones. *J. Geophys. Res.*, **112**(B01205), –. 35

Boettcher, Margaret S, McGarr, Art, & Johnston, Malcolm. 2009. Extension of Gutenberg-Richter distribution to MW -1.3, no lower limit in sight. *Geophys. Res. Lett.*, **36**(L10307). 35

Braunmiller, Jochen, & Nábělek, John. 2008. Segmentation of the Blanco Transform Fault Zone from earthquake analysis: Complex tectonics of an oceanic transform fault. *J. Geophys. Res.*, **113**(B07108). 34

Brune, J N. 1968. Seismic moment, seismicity, and rate of slip along major fault zones. *J. Geophys. Res.*, **73**(2), 777–784. 34

Carbotte, Suzanne M, & Macdonald, KC. 1994. Comparison of seafloor tectonic fabric at intermediate, fast, and super fast spreading ridges: Influence of spreading rate, plate motions, and ridge segmentation on fault patterns. *J. Geophys. Res.*, **99**(B7). 33, 44

Chen, Yongshun, & Morgan, W Jason. 1990. A Nonlinear Rheology Model for Mid-Ocean Ridge Axis Topography. *J. Geophys. Res.*, **95**(B11), 17583–17604. 11

Christophersen, Annemarie, Litchfield, Nicola, Berryman, Kelvin, Thomas, Richard, Basili, Roberto, Wallace, Laura, Ries, William, Hayes, Gavin P, Haller, Kathleen M, Yoshioka, Toshikazu, Koehler, Richard D, Clark, Dan, Wolfson-Schwehr, Monica, Boettcher, Margaret S, Villamor, Pilar, Horspool, Nick, Ornthammarath, Teraphan, Zuñiga, Ramon, Langridge, Robert M, Stirling, Mark W, Goded, Tatiana, Costa, Carlos, & Yeats, Robert. 2015. Development of the Global Earthquake Model's neotectonic fault database. *Natural Hazards*, **79**(1), 111–135. 51

Coffin, M F, Gahagan, L M, & Lawver, L A. 1998. *Present-day plate boundary digital data compilation.* Tech. rept. 174. University of Texas Institute for Geophysics. 37, 39

Conder, James A, Scheirer, Daniel S, & Forsyth, Donald W. 2000. Seafloor spreading on the Amsterdam-St. Paul hotspot plateau. *J. Geophys. Res.*, **105**(B4), 8263. 49

Croon, Marcel B, Cande, Steven C, & Stock, Joann M. 2010. Abyssal hill deflections at Pacific-Antarctic ridge-transform intersections. *Geochem. Geophys. Geosyst.*, **11**, 25 PP.–25 PP. 36, 39

Dick, Henry J B, Lin, Jian, & Schouten, Hans. 2003. An ultraslow-spreading class of ocean ridge. *Nature*, **426**, 405–412. 38

Dietz, Robert S, Menard, Henry W, & Hamilton, Edwin L. 1954. Echograms of the Mid-Pacific expedition. *Deep Sea Research (1953)*, **1**(4), 258IN3267–266IN4272. 38

Dziak, Robert P, Fox, Christopher G, Embley, Robert W, L, Nabelek John, Braunmiller, Jochen, & Koski, Randolph A. 2000. Recent tectonics of the Blanco Ridge, eastern blanco transform fault zone. *Mar. Geophys. Res.*, **21**(5), 423–450. 31

Ekström, G, Nettles, M, & Dziewoński, A M. 2012. The global CMT project 2004-2010: Centroid-moment tensors for 13,017 earthquakes. *Phys. Earth Planet. Inter.*, **200**(June), 1–9. 38, 41

Embley, Robert W, & Wilson, D S. 1992. Morphology of the Blanco Transform Fault Zone-NE Pacific: implications for its tectonic evolution. *Mar. Geophys. Res.*, **14**(1), 25–45. 2, 7, 17, 31, 33

Fornari, Daniel J, Gallo, David G, Edwards, Margo H, Madsen, John A, Perfit, Michael R, & Shor, Alexander N. 1989. Structure and topography of the Siqueiros transform fault system: Evidence for the development of intra-transform spreading centers. *Mar. Geophys. Res.*, **11**(4), 263–299. 2, 7, 31, 38

Forsyth, Donald W, Kerber, L, & Pickle, R. 2007. Co-existing Overlapping-Spreading-Center and Ridge-Transform Geometry. *AGU Fall Meeting Abstracts*, **-1**(Dec.), 05. 31

Fox, Paul J, & Gallo, David G. 1984. A tectonic model for ridge-transform-ridge plate boundaries: implications for the structure of oceanic lithosphere. *Tectonophysics*, **104**(3-4), 205–242. 30, 38

Fox, Paul J, & Gallo, David G. 1989. Transforms of the Eastern Pacific. *Pages 111–124 of:* Winterer, Edward L., Hussong, Donald M., & Decker, Robert W. (eds), *The Eastern Pacific Ocean and Hawaii.* Boulder, CO: Geological Society of America. 1, 4, 30, 33, 40

Frohlich, Cliff, & Wetzel, Laura Reiser. 2007. Comparison of seismic moment release rates along different types of plate boundaries. *Geophys. J. Int.*, **171**(2), 909–920. 34

Froment, B, McGuire, Jeffery J, Hilst, R D, Gouédard, P, Roland, E C, Zhang, H, & Collins, J A. 2014. Imaging along-strike variations in mechanical properties of the Gofar transform fault, East Pacific Rise. *J. Geophys. Res. Solid Earth*, **119**(9), 7175–7194. 18, 20

Gallo, David G, Fox, Paul J, & Macdonald, Ken C. 1986. A Sea Beam Investigation of the Clipperton Transform Fault: The Morphotectonic Expression of a Fast Slipping Transform Boundary. *J. Geophys. Res.*, **91**(B3), 3455–3467. 38

Goff, John A, Fornari, Daniel J, Cochran, James R, Keeley, Christopher, & Malinverno, Alberto. 1993. Wilkes transform system and "nannoplate". *Geology*, **21**(7), 623–626. 31

Gregg, Patricia M, Lin, J, & Smith, Deborah K. 2006. Segmentation of transform systems on the East Pacific Rise: Implications for earthquake processes at fast-slipping oceanic transform faults. *Geology*, **34**(4), 289. 4, 30, 33

Gregg, Patricia M, Behn, Mark D, Lin, J, & Grove, T L. 2009. Melt generation, crystallization, and extraction beneath segmented oceanic transform faults. *J. Geophys. Res.*, **114**. 33

Harris, Ruth A, & Day, Steven M. 1993. Dynamics of fault interaction: Parallel strike-slip faults. *J. Geophys. Res.*, **98**(B3), 4461–4472. 17

Hékinian, Roger, Juteau, T, Gràcia, E, Sichler, B, Sichel, S, Udintsev, G, Apprioual, R, & Ligi, M. 2000. Submersible observations of Equatorial Atlantic mantle: The St. Paul Fracture Zone region. *Mar. Geophys. Res.*, **21**(6), 529–560. 2

Hey, Richard. 1977. A new class of "pseudofaults" and their bearing on plate tectonics: A propagating rift model. *Earth Planet. Sci. Lett.*, **37**(2), 321–325. 30

Hirth, G, & Kohlstedt, D L. 1995. Experimental constraints on the dynamics of the partially molten upper mantle: 2. Deformation in the dislocation creep regime. *J. Geophys. Res.*, **100**(B8), 15441. 10

Hirth, Greg, & Kohlstedt, David L. 2003. Rheology of the upper mantle and the mantle wedge: a view from the experimentalists. *Inside the Subduction Factory, Geophysical Monograph*, **138**, 83–105. 8

Jordan, Thomas H, & Grotzinger, John. 2008. *The Essential Earth.* 1 edn. W. H. Freeman & Company. 1

Kagan, Yan Y, & Jackson, D D. 2000. Probabilistic forecasting of earthquakes. *Geophys. J. Int.*, **143**, 438–453. 41

Kastens, Kim A, Macdonald, K C, Becker, K, & Crane, K. 1979. The Tamayo transform fault in the mouth of the Gulf of California. *Mar. Geophys. Res.*, **4**(2), 129–151. 33

Kreemer, Corné, Haines, John, Holt, William E E, Blewitt, Geoffrey, & Lavallee, David. 2000. On the determination of a global strain rate model. *Earth Planets and Space*, **52**, 765–770. 20, 38

Lonsdale, Peter. 1978. Near-Bottom Reconnaissance of a Fast-Slipping Transform Fault Zone at the Pacific-Nazca Plate Boundary. *JG*, **86**, 451–472. 31, 38

Lonsdale, Peter. 1994. Structural geomorphology of the Eltanin fault system and adjacent transform faults of the Pacific-Antarctic plate boundary. *Mar. Geophys. Res.*, **16**(2), 105–143. 4, 31, 33

Macdonald, KC, Castillo, DA, Miller, SP, Fox, Paul J, Kastens, Kim A, & Bonatti, Enrico. 1986. Deep-tow studies of the Vema Fracture Zone: 1. Tectonics of a major slow slipping transform fault and its intersection with the Mid-Atlantic Ridge. *J. Geophys. Res.*, **91**, 3334–3354. 30

Macdonald, Ken, Sempéré, Jean-Christophe, & Fox, Paul J. 1984. East Pacific Rise From Siqueiros to Orozco Fracture Zones: Along-Strike Continuity of Axial Neovolcanic Zone and Structure and Evolution of Overlapping Spreading Centers. *J. Geophys. Res.*, **89**(B7), PP. 6049–6069–PP. 6049–6069. 44

Macdonald, Ken C, Kastens, Kim A, Spiess, F N, & Miller, S P. 1979. Deep tow studies of the Tamayo transform fault. *Mar. Geophys. Res.*, **4**(1), 37–70. 30

Macdonald, Ken C, Fox, Paul J, Miller, Steve, Carbotte, Suzanne M, Edwards, Margo H, Eisen, Mark F, Fornari, Daniel J, Perram, Laura, Pockalny, Robert A, Scheirer, Daniel S, Tighe, Stacey, Weiland, Charles, & Wilson, Doug. 1992. The East Pacific Rise and its Flanks 8-18° N: History of Segmentation, Propagation and Spreading Direction Based on SeaMARC II and Sea Beam Studies. *Mar. Geophys. Res.*, **14**, 299–344–299 – 344. 33, 44

McGuire, Jeffery J. 2008. Seismic cycles and earthquake predictability on East Pacific Rise transform faults. *Bull. Seismol. Soc. Am.*, **98**(3), 1067–1084. 1, 7, 18, 50

McGuire, Jeffery J, Boettcher, Margaret S, & Jordan, Thomas H. 2005. Foreshock sequences and short-term earthquake predictability on East Pacific Rise transform faults. *Nature*, **434**(7032), 457–461. 1

McGuire, Jeffery J, Collins, John A., Gouédard, Pierre, Roland, Emily C, Lizarralde, Dan, Boettcher, Margaret S, Behn, Mark D, & van der Hilst, Robert D. 2012. Variations in earthquake rupture properties along the Gofar transform fault, East Pacific Rise. *Nat. Geosci.*, **5**(5), 336–341. 7, 18, 30, 50

Menard, H W, & Atwater, Tanya. 1968. Changes in Direction of Sea Floor Spreading. *Nature*, **219**(5153), 463–467. 1, 4, 30, 33, 38

Murton, B J. 1986. Anomalous oceanic lithosphere formed in a leaky transform fault: evidence from the Western Limassol Forest Complex, Cyprus. *J. Geol. Soc.*, **143**(5), 845–854. 33

Oglesby, D. 2008. Rupture Termination and Jump on Parallel Offset Faults. *Bull. Seismol. Soc. Am.*, **98**(1), 440–447. 17

Parson, L M, & Searle, R C. 1986. Strike-slip fault styles in slow-slipping oceanic transform faults—evidence from GLORIA surveys of Atlantis and Romanche Fracture Zones. *J. Geol. Soc.*, **143**(5), 757–761. 30

Pickle, R C, Forsyth, Donald W, Harmon, Nicholas, Nagle, A N, & Saal, A. 2009. Thermomechanical control of axial topography of intra-transform spreading centers. *Earth Planet. Sci. Lett.*, **284**(3-4), 343–351. 18, 32

Pockalny, Robert A. 1997. Evidence of transpression along the Clipperton Transform: Implications for processes of plate boundary reorganization. *Earth Planet. Sci. Lett.*, **146**(3-4), 449–464. 33, 36, 40

Pockalny, Robert A, Fox, Paul J, Fornari, Daniel J, Macdonald, K C, & Perfit, M R. 1997. Tectonic reconstruction of the Clipperton and Siqueiros Fracture Zones: Evidence and consequences of plate motion change for the last 3 Myr. *J. Geophys. Res.*, **102**(B2), 3167–3181. 2, 4, 33, 34, 40

Roland, Emily C, & McGuire, Jeffery J. 2009. Earthquake swarms on transform faults. *Geophys. J. Int.*, **178**(3), 1677–1690. 30

Roland, Emily C, Behn, Mark D, & Hirth, Greg. 2010. Thermal-mechanical behavior of oceanic transform faults: Implications for the spatial distribution of seismicity. *Geochem. Geophys. Geosyst.*, **11**(7), n/a–n/a. 8, 11, 12, 35

Roland, Emily C, Lizarralde, Dan, McGuire, Jeffery J, & Collins, John A. 2012. Seismic velocity constraints on the material properties that control earthquake behavior at the Quebrada-Discovery-Gofar transform faults, East Pacific Rise. *J. Geophys. Res.*, **117**(B11102), B11102. 21

Ryan, William B F, Carbotte, Suzanne M, Coplan, JO, O'Hara, S, Melkonian, A, Arko, R, Weissel, RA, Ferrini, V, Goodwillie, A, Nitsche, F, *et al.*. 2009. Global Multi-Resolution Topography synthesis. *Geochem. Geophys. Geosyst.*, **10**(3), Q03014. 30, 36

Sandwell, David T. 1986. Thermal stress and the spacings of transform faults. *J. Geophys. Res.*, **91**, 6405–6418. 30

Sandwell, David T, Müller, R Dietmar, Smith, Walter H F, Garcia, Emmanuel, & Francis, Richard. 2014. Marine geophysics. New global marine gravity model from CryoSat-2 and Jason-1 reveals buried tectonic structure. *Science*, **346**(6205), 65–67. 30, 31, 41, 51

Scheirer, Daniel S, Forsyth, Donald W, Conder, James A, & Hung, Shu-Huei. 2007. Anomalous seafloor spreading of the Southeast Indian Ridge near the Amsterdam-St. Paul Plateau. *J. Geophys. Res.*, **105**(May), 8243–8262. 49

Sclater, John G, Grindlay, Nancy R, Madsen, John A, & Rommevaux-Jestin, Celine. 2005. Tectonic interpretation of the Andrew Bain transform fault: Southwest Indian Ocean. *Geochem. Geophys. Geosyst.*, **6**, 21 PP.–21 PP. 2

Searle, R C. 1983. Multiple, closely spaced transform faults in fast-slipping fracture zones. *Geology*, **11**(10), 607–610. 1, 20, 30, 33, 39

Searle, R C. 1986. GLORIA investigations of oceanic fracture zones: comparative study of the transform fault zone. *J. Geol. Soc.*, **143**(5), 743–756. 30, 33

Searle, Roger. 1984. Gloria survey of the east pacific rise near 3.5°S: Tectonic and volcanic characteristics of a fast spreading mid-ocean rise. *Tectonophysics*, **101**(3-4), 319–344. 38

Smith, Walter H F. 1998. Seafloor Tectonic Fabric from Satellite Altimetry. *Annu. Rev. Earth Planet. Sci.*, **26**(1), 697–747. 30

Smith, Walter H F, & Sandwell, David T. 1997. Global Sea Floor Topography from Satellite Altimetry and Ship Depth Soundings. *Science*, **277**(5334), 1956–1962. 21, 30, 31, 32, 36, 39

Sonder, Leslie J, & Pockalny, Robert A. 1999. Anomalously rotated abyssal hills along active transforms: Distributed deformation of oceanic lithosphere. *Geology*, **27**(11), 1003–1006. 36, 39

Sykes, Lynn R, & Ekström, Göran. 2012. Earthquakes along Eltanin transform system, SE Pacific Ocean: fault segments characterized by strong and poor seismic coupling and implications for long-term earthquake prediction. *Geophys. J. Int.*, **188**(2), 421–434. 1, 7, 30

Taylor, Brian, Crook, Keith, & Sinton, John. 1994. Extensional transform zones and oblique spreading centers. *J. Geophys. Res.*, **99**(B10), 19707–19718. 30

Wesnousky, Steven G. 1988. Seismological and structural evolution of strike-slip faults. *Nature*, **335**(6188), 340–343. 16

Wesnousky, Steven G. 2008. Displacement and Geometrical Characteristics of Earthquake Surface Ruptures: Issues and Implications for Seismic-Hazard Analysis and the Process of Earthquake Rupture. *Bull. Seismol. Soc. Am.*, **98**(4), 1609–1632. 17

Wesnousky, Steven G, & Biasi, G P. 2011. The Length to Which an Earthquake Will Go to Rupture. *Bull. Seismol. Soc. Am.*, **101**(4), 1948–1950. 17

Willoughby, E C, & Hyndman, R D. 2005. Earthquake rate, slip rate, and the effective seismic thickness for oceanic transform faults of the Juan de Fuca plate system. *Geophys. J. Int.*, **160**, 855–868. 1, 30

Wilson, J Tuzo. 1965a. A New Class of Faults and their Bearing on Continental Drift. *Nature*, **207**(4995), 343–347. 1, 30

Wilson, J Tuzo. 1965b. Transform Faults, Oceanic Ridges, and Magnetic Anomalies Southwest of Vancouver Island. *Science*, **150**(3695), 482–485. 30

Wolfson-Schwehr, Monica, Boettcher, Margaret S, McGuire, Jeffery J, & Collins, John A. 2014. The relationship between seismicity and fault structure on the Discovery transform fault, East Pacific Rise. *Geochem. Geophys. Geosyst.*, **15**(9), 3698–3712. 7, 18, 20, 31, 33, 38, 40, 41, 50